/N-71
42157
89P

The Use of Cowl Camber and Taper to Reduce Rotor/Stator Interaction Noise

R. Martinez
Cambridge Acoustical Associates, Inc.
Medford, Massachusetts

February 1995

National Aeronautics and
Space Administration
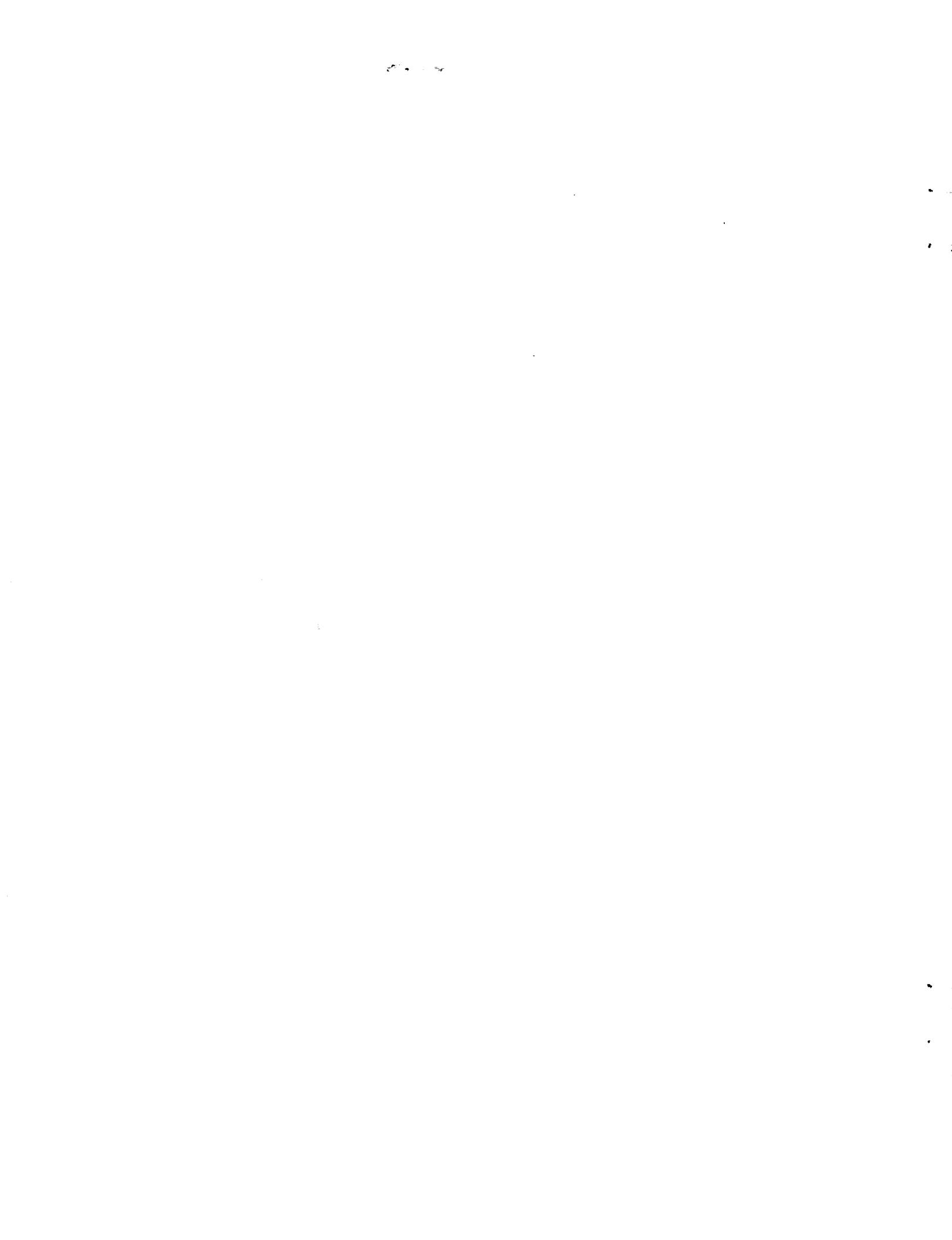
THE USE OF COWL CAMBER AND TAPER TO REDUCE ROTOR/STATOR INTERACTION NOISE

by R. Martinez

TABLE OF CONTENTS

Page

NOMENCLATURE

Roman

a	cowl radius normalized by the duct's halflength L/2
A	parameter used to characterize the width of the impinging wakes
B_R	number of rotor blades
B_S	number of stator blades
c	speed of sound of the medium
$\bar{c}(r^{\cdot})$	nondimensional chord for the radiating blades
D/Dt	substantial derivative, $\partial/\partial t + U_{ax}\,\partial/\partial z$
H_v	Hankel function of the first kind of order v
J_v	Bessel function of order v
k	cowl's reduced frequency, $\omega L/2U_{ax}$
$\bar{k}$	transform wavenumber; nondimensional in Appendix A and dimensional in Appendix B
L/2	cowl's halflength or halfchord, the normalizing constant for all distances and wavenumbers
L_{liner}	length of lined segment (Appendix A)
m	temporal harmonic counter; m=1 corresponds to the blade-passage frequency; also serves in the same context as the rotor wake's Fourier counter
M_{ax}	flight Mach number; the "ax" subscript denotes "axial"

$M_r(r^*)$ Mach number relative to the blade section at radial station r*

n Stator Fourier counter

p time-dependent pressure; dimensional; as on the left-hand side of Eq. 5a

$\bar{p}, \bar{p}_\nu$ frequency-domain pressure, and its circumferential ν mode; both dimensional

p_ν^{inc} incident field pressure of circumferential mode ν, corresponding to $\exp(-i\omega t)$.

$p_\nu{}', p_\nu{}^{th}$ lifting and thickness contributions to the scattered pressure; dimensional

P_o pressure source strength in the traditional treatment of the trailing-edge diffraction problem

$\ddot{Q}_o$ volume source strength in the canonical model

r field value of the radial coordinate; r=a corresponds to the cowl's wall; nondimensional

r^* running radial variable distinguishing among blade stations; nondimensional

R_o nondimensional range to the farfield observer, with origin at the cowl's geometric center r=0, z=0. $\hat{R}_o$ is its dimensional version, $R_o L/2$, used in the retarded time on Eq. 16's left-hand side.

R^* distance from vertex to source point in the canonical model; dimensional

S Sears function

t time; dimensional

T_{nB_s} aerodynamic transfer function. The nB_S subscript becomes mB_R for the rotor-first case

u_{nB_s} $(nB_S)^{th}$ circumferential Fourier mode of the impinging wake

u parameter used to describe the maximum deficit in the impinging wakes

U_{ax} freestream or flight speed

$U_{s>}$	swirl "freestream" between the stator and the rotor in a stator-first configuration
$U_{B>}$	swirl "freestream" between the rotor and the stator in a rotor-first configuration
$U_r(r^*)$	relative freestream for the radiating blade section at $r=r^*$
$\tilde{w}_v^{inc}$	incident field's radial particle velocity over $r=a^+$; dimensional (Appendix A)
z	axial coordinate for a cowl control point; nondimensional
z^*	axial station of a typical radiating point for the incident field
z_{mid}	midpoint axial position for a liner ring patch (Appendix A)
Z_{liner}	liner impedance (Appendix A)

Greek

α_{liner}	axially variable admittance of the liner, normalized by the fluid's characteristic admittance $1/\rho c$
β_{ax}^2	$1-M_{ax}^2$
γ_m	transform wavenumber for the radial direction, Eq. 5c.
$\Delta p, \Delta w$	unknown diffraction loading $\tilde{p}^+ - \tilde{p}^-$ in the lifting problem, and unknown monopole strength $\tilde{w}^+ - \tilde{w}^-$ for the nonlifting problem; each of these two quantities takes on a v subscript when it becomes the circumferential mode of the parent variable; "+" and "−" denote $r=a^+$ and $r=a^-$
η	liner loss factor (Appendix A)
θ_o	off-axis directivity angle measured downward from the forward flight direction
K_v^{u}	lifting kernel, or influence function linking the induced radial velocity to the virtual lift (Appendices A and B)

$K_v^{\ell,th}$ kernel linking the radial upwash to the thickness source strength, or pressure to the virtual lift (Appendices A and B)

$K_v^{th,th}$ kernel linking pressure to the cowl's dynamic thickness source strength (Appendices A and B)

μ relative angle between the vortical wavefronts of the impinging wake's effective gusts and the chord surfaces of the cutting blades, following the nomenclature in Goldstein's book[12]

ν circumferential mode; short for $mB_R - nB_S$, the spinning mode index

$\upsilon_R(r^\cdot)$ pitch angle for the B_R rotor blade sections at radial station r^*

$\upsilon_S(r^\cdot)$ pitch angle for the B_S stator blade sections at radial station r^*

ρ background fluid density

$\phi, \phi^\cdot$ field and source values of the circumferential angle

$\phi_\ell(r^*)$ parameter to describe wake lean

Ω propeller's rotational speed

ω frequency, ultimately $mB_R\Omega$ in the tonal problem investigated here

I ABSTRACT

This project has had two specific technical objectives: (1) To develop a realistic three-dimensional model of tonal noise due to rotor/stator interaction, as the input field for predictions of diffraction and dissipation by a lined cowl; and (2) To determine whether the generator curve of that cowl, or duct, could be "steered" to yield substantially lower values of propulsor noise along the engine's fore and aft open sectors. The more general and important aim of the research is to provide the commercial aircraft industry with a useful predictive tool to help it meet its noise-reduction goals.

The work has produced a tractable and yet realistic model of rotor/stator interaction noise. The blades in the fan stage are radially divergent, twisted, and of realistically wide chords to match the regime of high frequencies and speeds of the sound-production process. The resulting three-dimensional acoustic nearfield insonifies the interior wall of the diffracting cowl, whose shape, incidentally, does not affect fore or aft noise significantly. The predictions address both the fan's blade-passage frequency and its first overtone, "m=2". They indicate moderate acoustic shielding for the lined-cowl system; for example, see Fig. 17a.

II   INTRODUCTION

A.   GENERAL

The aims of the Phase I project have been twofold: (1) To produce, as an extension of the work in Ref. 1, a realistic three-dimensional theoretical model of rotor/stator noise from the fan stage of an Advanced Ducted Propulsor or Propeller (ADP[2-4], Figs. 1a-c); and (2) To couple the resulting theory rigorously to a model that calculates the diffraction effect of a short cowl, or lined duct, on the propagation of that complex propulsor nearfield.

This second goal was to be achieved through a coupling of formal unsteady lifting and nonlifting surfaces as mathematical replacements for the scattering unflanged cowl. Appendix A, excerpted from the Principal Investigator's Ref. 1, collects the integral equations that govern aeroacoustic diffraction for a straight duct of circular cross section. Myers and Lan[5] have recently implemented the time-domain version of the "lift" part of that theory, i.e., for an unlined cowl, in their own independent research effort.

An important side question for the present project was whether the generator shape of the modeled cowl could be generalized theoretically, and used practically, to broaden the zone of null near-axis radiation of the lower order spinning modes resulting from rotor/stator interactions. Appendix B documents that analytical extension of the cowl's coupled lifting- and nonlifting-surface theories to include arbitrary warp in the duct's fore/aft direction. The cowl's cross section remains circular at every axial station. The speed/frequency regime is still Ref. 1's high subsonic range for an arbitrarily noncompact cowl of "halfchord" L/2.

The predictions of cowl-diffracted rotor/stator noise were to be provided for two kinds of observers whose perception of that sound would differ fundamentally for moderate to high values of the flight Mach number: (a) for passengers on the aircraft, relative to which the position of the noise-producing stators clearly does not change; and (b) for listeners on the ground, who would experience both the incident and the cowl-diffracted fields as sweeping by, i.e., Doppler-shifted and with their rays amplified in the forward direction.

The Phase I theoretical development has considered rotor/stator as well as stator/rotor interactions. The study just completed has resulted in four computer codes that predict cowl diffraction rigorously for noise from blades that are radially divergent, twisted, and with chords

2

diffraction rigorously for noise from blades that are radially divergent, twisted, and with chords that may be either aerodynamically compact or noncompact. Code 1 takes the stator to be upstream of the rotor, and the downstream radiating rotor blades are chordwise compact. Code 2 is the same as 1 but for noncompact rotor chords. Codes 3 and 4 are the rotor-first, stator-second counterparts of codes 1 and 2 (codes 3 and 4 are of immediate interest to the civil aircraft industry, while codes 1 and 2 could have other applications).

The side question regarding the potential effect of cowl camber or taper on on-axis engine noise has been answered, at least temporarily, through the development and exercise of offline canonical models rather than through the implementation of Appendix B's exact theory for a doubly warped cowl in unsteady subsonic flow. That is because the canonical calculations concluded, relatively early on, that unrealistically high values of camber or taper would be required to achieve such off-axis kinematic "steering" of fan noise. The remaining Phase I research time was devoted to the thorough source modeling described in the previous paragraph, e.g., to the nontrivial analysis and numerical prediction of the nearfield velocities and pressures with which a set of radially divergent and twisted stator blades of wide chords would drive, aeroacoustically, a formally diffracting straight cowl.

Readers not primarily concerned with theoretical developments should proceed directly to Sections V and VI.

B.   ADVANTAGES/FEATURES OF THE PRESENT LIFTING/NONLIFTING SURFACE APPROACH OVER ALTERNATE FLUID-FINITE ELEMENT MODELS

(1)   Our system of surface equations addresses one dimension less than the volume approach[6], with a corresponding potential gain in computational efficiency.

(2)   The lifting-surface theory developed under Phase I is of the acceleration potential type. It contains implicitly, and exactly, the shed and trailed vortex flows of the cowl in its role of ring wing. Those trailed and shed vortex systems do not spread for inviscid flow, i.e., they do not decay spatially with distance past the cowl's outlet, or "trailing edge", so that their capture as part of the diffraction solution should be especially cumbersome via finite elements. Moreover, the

stator blades shed their own "incident" vortex system if the airloads resulting from the whipping effect of the rotor's wakes are properly modelled as the product of fully unsteady aerodynamics.

Only by invoking quasi-steady aerodynamics, which incidentally becomes untenable for the chordwise-noncompact regime of actual practice, could that pattern of directly shed vortices from the fan stage be neglected when calculating the volumetric flowfield. The present technique already accounts for these incident shed vortices, while the finite-element approach would again have to capture them through a laborious downstream gridding similar to that required past the cowl's trailing edge (the pole $\bar{k}+mB\Omega L/2U_{ax}\beta^2_{ax}$ in the wavenumber transform of Ref.1's Eq. 57b contains analytically the field of induced vortex flows from the radiating blades).

An important remaining problem in the overall research effort is the unified prediction of cowl diffraction and multiple scattering by all of the blades in the three-dimensional fan stage. That modelling extension would include the rotor's forward transmission loss as a by-product. Blade scattering, or diffraction, is a fundamentally unsteady-aerodynamics phenomenon which, for the frequencies of interest and for the reasons just stated, would seem to be beyond the feasible computational capabilities of the currently used finite-element technique. That finite-element code would have to remain practically "non-unified" and therefore fundamentally iterative, or approximate (cf., for example, Meyer's[7] nicely detailed paper on the importance of inlet reflections, calculated for one iteration). The volumetric approach would have to keep relying on an intermediate canonical code to furnish it with modal generalized forces that it would then "propagate". The surface approach could eventually handle the problem of inlet and outlet reflections in a unified rather than iterative manner. That is because its influence functions may, and in fact already are, expressed spectrally both for the incident and diffracted fields. Each such function appears in Appendix A and in Ref. 1 as a wavenumber transform in $\bar{k}$. The combination $\exp(-i\bar{k}z-iv\phi)$ could serve in a formal superposition to determine the a priori-unknown incident nearfield at every diffracting blade strip in the fan stage. The resulting system of running "plane waves" incident on each such strip could be converted analytically into a diffraction load distribution for that airfoil section. That chordwise load distribution would

4

"return" to the three-dimensional medium as an elemental reflection and transmission whose strength would be found as part of the otherwise rigorous solution of the global cowl/centerbody/blades scattering problem.

(3)   The surface approach meets the radiation condition exactly through the theory's building-block Green's function; i.e., through the point-source solution of the convected wave equation for a uniform freestream U_∞ of Mach number M_∞. The surface theory does not have to worry about spurious returns from infinity (although neither does the latest generation of volumetric techniques, which use infinite elements).

(4)   The lifting/nonlifting-surface solution of the cowl diffraction problem contains all of the information of duct acoustics, even though it is not formulated with a waveguide in mind. A post-processing of the combined incident plus diffracted fields inside the cowl would display all of the modal content of a leaky waveguide, with cut-on frequencies for each of the incident field's generalized forces, etc.; cf., for example, Fig. 4 from Ref. 8.

(5)   A more "buried" advantage of the surface approach is that its kernel functions have been analytically regularized, and that the singular parts have been found to be independent of the spinning mode number $\nu = mB_R - nB_S$ (B_R and B_S are the number of rotor and stator blades in the fan stage). The submatrices associated with those singular subkernels may therefore be recycled from each ν singular-equation system to the next. These singular subkernels show up as the first term on the right hand sides of Eqs. A.5 and A.7.

C.   DISADVANTAGES OF THE PRESENT LIFTING/NONLIFTING-SURFACE APPROACH RELATIVE TO FINITE ELEMENTS

Our approach is fundamentally boundary-element in nature.

The main drawback of boundary-element numerical solutions to problems in unbound media is that the governing differential equation on which those techniques are based may not have arbitrarily variable coefficients. All boundary-element techniques rely on the analytical existence of a free-field Green's function to convert the original volumetric differential statement into an integral one, expressed only over the domain's bounding surfaces (to be sure, a Green's

function can usually be found approximately for the general case, e.g., by WKB[9]).

For the problem at hand, i.e., for the rigorous prediction of diffraction or scattering by the cowl, and eventually also for the coupled centerbody, the restriction of having a convected wave equation with constant coefficients causes the freestream and associated Mach number to be constant throughout the engine. The main immediate consequences of that are, or would be:

(a)   A centerbody that would not satisfy steady flow tangency, i.e., that would remain hydrodynamically transparent to the axial steady freestream striking it. The surface-only exact approach would lack the effects of ray bending which the missing steady streamlines would have contributed.

(b)   Swirl between the rotor and the stator generates a local convected wave equation with effectively variable coefficients. It is generally not possible to deflate it as usual to a non-convected wave equation with even derivatives through the usual changes in independent and dependent variables (or through the equivalent use of simultaneous Lorentz and Galilean transformations). The present approach thus cannot account for the propagation effects of swirl, at least not exactly.

(c)   The effect on acoustic propagation of a fan exhaust that is larger than the external flight speed $U_{\alpha x}$ is also not be easily handled by the present approach, although it may be possible, with some work, to adapt the surface approach to treat abrupt changes in $U_{\alpha x}$ from one constant value to another through the engine.

III   INCIDENT FIELD ANALYSIS

A.   CHORDWISE-COMPACT AND CHORDWISE-NONCOMPACT SOURCE
      REPRESENTATIONS FOR TWISTED STATOR AND ROTOR BLADES

A.1   General

A major objective of the current study is to model mathematically not only the diffraction and dissipation effects of a short lined duct in a compressible freestream, but to generate also the incident field "p^{inc}" driving that cowl from within. The analysis of this part of the problem will confine itself here to well-known mechanisms of tonal noise from turbomachines: (1) the chopping of stator wakes by a rotor, as displayed on the left half of Fig. 2a, and the whipping effect of that rotor's "viscous" wake on a downstream stator[10], shown on the right-hand side of Fig. 2a[11]. This second type of unsteady-aerodynamics "interaction" is normally the only one of interest in the fan stage of current designs of civil-aircraft engines. Figs. 1a-c show modern examples without inlet guide vanes.

The theory developed here for the cowl's-felt incident "p^{inc}" pressure covers both of the sources of noise in Fig. 2a, though one at a time as described in split form by Figs. 2b,c[12]. Our aim in considering both cases is to further commercialize the work by having it apply also to turbomachines not necessarily within the civil aircraft industry. The equations given below in Sections A.2 through B.3 address the less relevant case in Fig. 2b. A final section, B.4, provides the key for the transfer of symbols and parameter values for the conversion to Fig. 2c.

A.2   Description of a Three-Dimensional Stator/Rotor Geometry for the Generation of the
       Cowl's Internal Incident Field (Stator-First, Rotor-Second Configuration)

Reference 1 considered a single generic inflow inhomogeneity stemming from an axially aligned stator blade. The downstream rotor blades were multiple in number but lay flat on their plane of rotation; i.e., they were untwisted and perpendicular to the implied single upstream vane. Their sound-producing unsteady loads were the result of assuming a chordwise compact aeroacoustic field from root to tip even when actual turning and flight speeds, and chord sizes, might have demanded otherwise.

The geometry of the stator/rotor stage for the rotor-airloads model will now instead be as

depicted in cross section in Fig. 2b. There are B_S stator blades rather than one. Moreover, they have an assigned pitch distribution $\upsilon_S(r^*)$ from root to tip, i.e., from $r^* = R_h$ to $r^* = R_t$, to be able to treat later the rotor-first case of Figs. 2c and 1a-c (Section B.4 below). The rotor blades are now similarly twisted according to $\upsilon_R(r^*)$, which, unlike $\upsilon_S(r^*)$, will not be prescribable but rather will be deducible from the criterion that all blade sections in the rotor operate at zero angle of attack relative to the local freestream $U_r(r^*)$. All leading edges in the rotor will be unswept, viz., straight from root to tip relative to that local grazing freestream.

The present study implements Fig. 2b to generate two separate models for the areoacoustic sources insonifying the cowl from within:

(1) The kinematically elaborate extension of Ref. 1's chordwise-compact rotor airloads to include the new geometric complexities for both sets of blades in Fig. 2b;

(2) A new chordwise noncompact rotor-loads model that will again go geometrically with Fig. 2b. The rotor blades will be a set of "leading-edge" semi-infinite flat plates, each with a $\upsilon_R(r^*)$ twist distribution from root to tip. The chordwise pressure distribution for each plate, at an arbitrary radial station r^*, will come from applying the "strip" assumption to that blade section.

A main feature of Fig. 2b is to account for a new "freestream $U_{S>}$" just downstream of the stator. The unsteady-aerodynamics model for the source strengths will allow that meanflow to differ not only in direction with respect to the axial flight speed $U_{\alpha x}$, as indicated in Fig. 2b, but also in terms of magnitude: $U_{S>} = U_{S>}(r^*)$ could be radially variable.

This ends the qualitative description of the new airloads models of the rotor in its role of aeroacoustic source. The second half of the insonifying part of the theory is to "propagate" the sound from these blade-based sources to the cowl's two-sided wall to drive the diffraction problem posed there. Fig. 2d shows the freestream model adopted during the current phase of work for this second part of the incident-field calculation: the swirl implied by $U_{S>}(r^*)$ has been taken away and the uniform axial flight speed $U_{\alpha x}$ applies throughout. The omission is typical of most "classical" solutions of the rotor/stator interaction problem; cf., for example, Envia's[10] Eq. 2.11d, where the substantial derivative for the convected wave equation contains

only the axial freestream component. A modern exception, though essentially two-dimensional or cascade in nature, is Hanson's recent analysis[4] of sound refraction through the tilted flow between the two sets of blades in our Fig. 2c.

A.3   Mathematical Construction of the Impinging Wakes

Fig. 3 displays the modeled spatial perturbation of the mean flow $U_{S>}(r)$ downstream of the stator blades. That "momentum-deficit" field will be Gaussian in shape and given by

$$u(r,\phi,\Delta z) = \bar{u}(r,\Delta z)\, e^{-A(r,\Delta z)[\phi-\phi_t(r)]^2} \quad , \tag{1}$$

where $\bar{u}(r,\Delta z)$ is the nonuniformity's maximum value and $A(r,\Delta z)$ a free dimensionless function that regulates the circumferential sharpness of each modelled stator wake. Both $\bar{u}$ and A are typically taken to have a strong dependence on the axial distance Δz downstream of the stator disk. The value of Δz relevant to the present theory is obviously the axial gap between the rotor and the stator. Parameter $\phi_t(r)$ traces out the circumferential position of maximum deficit as a function of radius; i.e., $\phi_t(r)$ is the wake's "lean" angle as described, for example, by Envia.[10]

The Fourier-series expansion of $u(r,\phi,\Delta z)$ in the angular segment $0<\phi<2\pi/B_S$ between adjacent stator blades yields a set of harmonic components $u_{\bar{n}}$ given by

$$u(r,\phi,\Delta z) = \sum_{\bar{n}=-\infty}^{\infty} u_{\bar{n}}(r,\Delta z)\, e^{i\bar{n}\phi} \quad , \tag{2a}$$

$$u_{\bar{n}}(r,\Delta z) = \frac{B_S}{2\pi} \int_0^{2\pi/B_S} d\tilde{\phi}\, e^{-i\bar{n}\tilde{\phi}}\, u(r,\tilde{\phi},\Delta z) \quad . \tag{2b}$$

A similar expansion again in ϕ, but now over the whole circumferential range

$0 < \phi < 2\pi$, introduces the components $u_n(r, \Delta z)$ for the counter "n" that are ultimately of interest in the airloads model (n without the overbar). For a stator with B_S identical blades, that circumferential "n" spectrum filters down to a sparser nB_S spectrum whose $u_{nB_S}(r, \Delta z)$ components are related to the $u_{\bar{n}}(r, \Delta z)$ values of Eqs. 2a,b by

$$u_{nB_S}(r, \Delta z) = \sum_{\bar{n}=-\infty}^{\infty} u_{\bar{n}}(r, \Delta z) e^{-i\pi(nB_S - \bar{n})/B_S} \frac{\sin[\pi(nB_S - \bar{n})/B_S]}{\pi(nB_S - \bar{n})/B_S} \quad . \tag{3}$$

The exponential and sine factors on the right side of Eq. 3 combine to give a Kronecker delta $\delta_{n\bar{n}}$ when $B_S = 1$, as they should.

The u_{nB_S} components normalized by the flight speed $U_{\alpha x}$ become

$$\frac{u_{nB_S}(r)}{U_{\alpha x}} = \frac{\bar{u}(r)}{U_{\alpha x}} \cdot \frac{B_S}{2\pi} \sum_{\bar{n}=-\infty}^{\infty} e^{-i\pi(nB_S - \bar{n})/B_S} \frac{\sin[\pi(nB_S - \bar{n})/B_S]}{\pi(nB_S - \bar{n})/B_S}$$

$$\int_0^{2\pi/B_S} d\tilde{\phi} \, e^{-i\bar{n}\tilde{\phi} - A(r)[\tilde{\phi} - \phi_t(r)]^2} \quad . \tag{4}$$

The dependence of $\bar{u}$ and A on Δz will be implied throughout.

A.4   The Near Field Radiated by the Rotor in Fig. 2a for Both Chordwise-Compact and Noncompact Loadings

    We postpone stating the precise form of the rotor's source-strength solutions, and present now the generalization by the present theory of Ref. 1's Eq. 57a:

$$p^{inc}(a, \phi, z, t) = \sum_{m=-\infty}^{\infty} e^{-imB_R \Omega t} \sum_{n=-\infty}^{\infty} e^{-i(mB_R - nB_S)(\phi - \phi^*)} \tilde{p}^{inc}_{mB_R - nB_S}(a, z) \quad , \tag{5a}$$

where the tilde on $\tilde{p}^{inc}$ on the right side, as in Ref. 1, denotes the harmonic spectral value of the

tonal signal, and the $mB_R - nB_S$ subscript has turned out to be the circumferential modal counter relevant to the problem. This double spectrum $\tilde{p}^{inc}_{mB_R - nB_S}$ is, for r=a, i.e., along the cowl's wall,

$$\tilde{p}^{inc}_{mB_R - nB_S}(a,z) = - \frac{B_R}{4\pi} \int_C d\bar{k} H^{(1)}_{mB_R - nB_S}(\gamma_m a) \int_{R_h}^{R_t} dr^* \frac{u_{nB_S}(r^*) T_{nB_S}(r^*, \bar{k}) \sin[\mu(r^*)]}{\rho U_{ax}^2 L}$$

$$\exp\left[-i\left(\frac{mB_R \Omega L M_{ax}}{2c\beta_{ax}^2} + \bar{k} \right)(z-z^*) \right] \tag{5b}$$

$$\cdot J_{mB_R - nB_S}(\gamma_m r^*) \left\{ \left(\bar{k} + \frac{mB_R \Omega L M_{ax}}{2c\beta_{ax}^2} \right) \sin[\upsilon_R(r^*)] + \frac{(mB_R - nB_S)\cos[\upsilon_R(r^*)]}{r^*} \right\} ,$$

where C is the contour shown in Fig. A.1, where the product of the cowl's reduced frequency k and the flight Mach number M_{ax} become $mB_R \Omega L/2c$. The new variables in Eq. 5b are

$$\gamma_m = \sqrt{\left(\frac{mB_R \Omega L}{2c}\right)^2 \frac{1}{\beta_{ax}^2} - \beta_{ax}^2 \bar{k}^2} \quad , \tag{5c}$$

$$\sin[\mu(r^*)] = \frac{\Omega L r^* \cos[\upsilon_S(r^*)]}{2U_r(r^*)} \quad , \tag{5d}$$

$$\sin[\upsilon_R(r^*)] = \frac{\frac{\Omega r^* L}{2} - U_{S>}(r^*)\sin[\upsilon_S(r^*)]}{U_r(r^*)} \quad , \tag{5e}$$

11

$$\cos[\upsilon_R(r^*)] = \frac{U_{S>}(r^*)\cos[\upsilon_S(r^*)]}{U_r(r^*)} \quad , \tag{5f}$$

$$U_r(r^*) = \sqrt{U_{S>}^2(r^*)\cos^2[\upsilon_S(r^*)] + \left(\frac{\Omega L}{2}r^* - U_{S>}(r^*)\sin[\upsilon_S(r^*)]\right)^2} \tag{5g}$$

Variable r^* is nondimensional throughout Eqs. 5b-g; its original dimensional form has been normalized by the cowl's axial half length $L/2$.

Eq. 5b returns to Ref. 1's Eq. 57a for $\upsilon_R(r^*) = \pi/2$, $\upsilon_S(r^*) = 0$, and $U_{S>} = 0$ in Eq. 5d (so that $U_r(r^*) = \Omega r^* L/2$ and $\sin[\mu(r^*)] = 1$). The second term within curly brackets in the $\bar{k}$ integrand accounts for the new component in the circumferential direction ϕ for the unsteady blade loads. It plays the role of the "drag" dipoles in Ref. 12's Eq. 3.119.

The group $\{u_{nB_S}(r^*)T_{nB_S}(r^*,\bar{k})\sin[\mu(r^*)]\}/\rho\, U_{ax}^2 L$ comes from the aerodynamic theories of the chordwise-compact and noncompact models. The $\bar{k}$ variable will drop out of the argument list of the aerodynamic transfer function T_{nB_S} in the former case.

A.5 Chordwise-compact and Noncompact Airload Solutions for the Rotor Blades

A.5.a The Improved Compact Model

Dittmar et al.[2b] have investigated the potentially beneficial effects of stator systems that were designed to be drastically chordwise noncompact. But that study will turn out to be qualitatively relevant also to more conventional modern stator designs, essentially because the aeroacoustic parameter $\omega\bar{c}/2c\,\beta_r^2$ of these recent stators sometimes approaches the effectively infinite value of those in Ref. 2b.

We report here only final results. Beginning with the chordwise-compact case, the normalized unsteady sectional lift on the rotor blades for $R_h < r^* < R_t$ is

$$\frac{u_{nB_s}(r^*)T_{nB_s}(r^*)\sin[\mu(r^*)]}{\rho U_{\alpha x}^2 L} = \frac{\pi B_S}{4J_t} \cdot \frac{\bar{u}(r^*)}{U_{\alpha x}} \cdot \frac{\bar{c}(r^*)}{R_t} r^* \cos[\upsilon_s(r^*)]$$

$$\cdot S\left(\frac{nB_S \Omega L \bar{c}(r^*)}{4U_r(r^*)}\right) \sum_{\bar{n}=-\infty}^{\infty} e^{-i\pi(nB_S - \bar{n})/B_S} \frac{\sin[\pi(nB_S-\bar{n})/B_S]}{\pi(nB_S-\bar{n})/B_S} \qquad (6)$$

$$\int_0^{2\pi/B_S} d\tilde{\phi} e^{-i\bar{n}\tilde{\phi}-A[\tilde{\phi}-\phi_t(r^*)]^2} \quad ,$$

where $\bar{c}(r^*)$ is the blade chord at the radial station r^* normalized by $L/2$, and S is the Sears function. J_t is short for the advance ratio $\pi U_{\alpha x}/(\Omega LR_t/2)$, with R_t similarly normalized by the cowl's halflength $L/2$.

A.5.b The New Analytical Noncompact Model

Variable z^* in the exponential term in Eq. 5b marks the axial positions of the source distribution. For the compact case z^* has a single value so long as the propeller's set of quarter-chord lines has no rake, i.e., so long as it is coplanar. That was implied in Ref. 1's Eq. 57a. Variable ϕ^* in Eq. 5a above plays a similar role for the circumferential direction: $\phi^* = 0$ refers to a circumferential datum position for the points on the surface of each rotor blade. ϕ^* is dispensable when the loading on the rotor blades is chordwise compact and when the blades are straight rather than swept; i.e., ϕ^* is to sweep what z^* is to rake, for a set of chordwise compact rotor blades. Ref. 1 considered unswept blades only and therefore set ϕ^* to zero throughout its analysis.

Both z^* and ϕ^* become necessary in Eqs. 5a and b when the blade airloads are chordwise noncompact even if the blades are straight and their rake is zero. One begins by setting $z^* = z_{g\ell}^* + z_{\ell o}^*$, where $z_{g\ell}^*$ is the "global" axial position of a chosen point in the radiating rotor, and $z_{\ell o}^*$ measures the local axial positions of blade points away from there. Variable ϕ^* is

13

now understood to be similarly local without need of the "ℓo" designating subscript. Then the relationship between z^*, ϕ^* and the chordwise variable x^*, which appears marked on the uppermost rotor blade in Fig. 2a, is

$$-r^*\phi^* = x^*\sin[\upsilon_R(r^*)] \quad , \tag{7a}$$

$$z^* - z_{g\ell}^* = z_{\ell o}^* = x^*\cos[\upsilon_R(r^*)] \quad . \tag{7b}$$

And the phase factors in Eqs. 5a and b become

$$\exp\left[-i(mB_R - nB_S)(\phi - \phi^*) - \frac{imB_R\Omega LM_{ax}(z-z^*)}{2c\beta_{ax}^2} - i\bar{k}(z-z^*)\right]$$

$$= \exp\left[-i(mB_R - nB_S)\phi - \frac{imB_R\Omega LM_{ax}(z-z_{g\ell}^*)}{2c\beta_{ax}^2} - i\bar{k}(z-z_{g\ell}^*)\right] \cdot Ph(x^*) \quad , \tag{8a}$$

where

$$Ph(x^*) = \exp\left\{x^*\left[-\frac{(mB_R - nB_S)}{r^*}\sin[\upsilon_R(r^*)]\right.\right.$$

$$\left.\left. + \left(\bar{k} + \frac{mB_R\Omega LM_{ax}}{2c\beta_{ax}^2}\right)\cos[\upsilon_R(r^*)]\right]\right\} \quad . \tag{8b}$$

The group $u_{nB_S}T_{nB_S}\sin\mu / \rho U_{ax}^2 L$ in Eq. 5b's r^* integrand now changes to

$$\frac{u_{nB_s} T_{nB_s} \sin\mu}{\rho U_{ax}^2 L} \rightarrow \frac{u_{nB_s} \sin\mu}{\rho U_{ax}^2 L} \int_0^{\bar{c}(r^*)} dx^* \left(\frac{\Delta p(x^*)}{u_{nB_s}} \right) Ph(x^*) \quad . \tag{9}$$

Quantity $\Delta p(x^*)/u_{nB_s}$ denotes the loading on the blade section in question normalized by the effective gust amplitude u_{nB_s}. This ratio is given analytically by Eq. 37 of Ref. 13 or by Eq. 15 of Ref. 14. In the former case the sweep angle is set to zero with the interpretation of the formulas in both studies considering a gust parallel to the leading edge.

We shall further simplify those canonical results by stripping them of their trailing-edge contribution, given that that contribution acts as a small correction to the dominating leading-edge part for the high-noncompact regime of interest here. Based on the $\exp(-i\omega t)$ $(= \exp(-imB_R\Omega t))$ temporal behavior adopted in Eq. 5a, then

$$\frac{\Delta p(x^*)}{u_{nB_s}} = -2\rho U_r \frac{e^{i\pi/4 + i\frac{nB_s \Omega L x^*}{2c(1+M_r)}}}{\pi \sqrt{1+M_r} \sqrt{\frac{nB_s \Omega L}{2U_r} x^*}} \quad . \tag{10}$$

Substitution into Eq. 9 yields, with Eq. 5d,

$$\frac{u_{nB_s}(r^*) T_{nB_s}(r^*, \bar{k}) \sin[\mu(r^*)]}{\rho U_{ax}^2 L} = -\frac{u_{nB_s}(r^*)}{U_{ax}} \cdot \frac{\Omega L}{2U_{ax}} \cdot r^* \cos[\upsilon_S(r^*)]$$

$$\cdot \frac{(1+i)}{\sqrt{\pi(1+M_r)}} \frac{1}{\sqrt{\frac{nB_s \Omega L}{2U_r}}} \frac{E\{\bar{c}(r^*)f(\bar{k})\}}{\sqrt{f(\bar{k})}} \quad , \tag{11}$$

where

$$
f(\bar{k}) = \frac{nB_S \Omega L}{2c(1+M_r)} + \left(\bar{k} + \frac{mB_R \Omega L M_{ax}}{2c\beta_{ax}^2} \right) \cos[\upsilon_R(r^*)]
$$

(12)

$$
- \frac{(mB_R - nB_S)}{r^*} \sin[\upsilon_R(r^*)] .
$$

E is a Fresnel integral defined by

$$
E(\psi) = \int_0^\psi \frac{d\xi e^{i\xi}}{\sqrt{2\pi\xi}} .
$$

(13a)

For $f(\bar{k})$ real and less than zero, the following would take over in Eq. 11:

$$
\frac{E\{\bar{c}(r^*)f(\bar{k})\}}{\sqrt{f(\bar{k})}} \rightarrow \frac{E^*\{-\bar{c}(r^*)f(\bar{k})\}}{\sqrt{-f(\bar{k})}} ,
$$

(13b)

where the asterisk on E^* stands for complex conjugate. The final step for the present development is to bring Eq. 4's expression for u_{nB_S}/U_{ax} into the first term on the right side of Eq. 11. We omit it for the sake of brevity.

B. FARFIELD EXPRESSIONS FOR $\tilde{p}_{mB_R-nB_S}^{inc}$

B.1 General

We shall follow Ref. 1 by considering again not one, but two separate farfield calculations that produce clearly different results when the flight Mach number M_{ax} is high subsonic (otherwise the two farfields coincide): (1) the directivity pattern perceived by observers

16

traveling with the aircraft, and (2) the corresponding field for ground-based observers. Farfield (1) is the one of interest for studies of transmission of engine noise into the cabin while in flight (assuming the distance from the engine to the cabin is large in terms of wavelengths). Farfield (2) becomes relevant for predictions of the environmental impact of the ducted or unducted propulsor on listeners on the ground, e.g., dwellers near an airport.

The following two subsections document the final results of both types of field for the chordwise-compact and noncompact models of loading on the radiating rotor blades. Those final results for $\tilde{p}_{mB_R - nB_S}^{inc}$ are interesting on their own right, but our main objective for generating them here is to complete the field of total pressures, incident plus diffracted, which are expected to have low levels in the shadow of the cowl's wall.

B.2 Farfield for Incident Rotor Sources in the Aircraft's Frame of Reference

Ref. 1's Eqs. 61a, b defined the directivity angle θ_o as $\tan^{-1}(-\beta_{ax} r/z)$ and the nondimensional range R_o to the observer as $\sqrt{r^2 + z^2 / \beta_{ax}^2}$. Neither variable was therefore completely physical in that both invoked β_{ax} for convenience. We redefine them here to be the more directly useful quantities $\tan^{-1}(-r/z)$ and $\sqrt{r^2 + z^2}$, respectively. E.g., R_o is now given by Ref. 1's symbol for R_o divided by $\beta_{ax}^{-1}\sqrt{1 - M_{ax}^2 \sin^2 \theta_o}$, a new factor taken now into the denominator of the right-hand sides of Ref. 1's expressions for incident and diffracted fields. These name changes also have the effect of turning Ref. 1's "$\cos\theta_o$" into

$\cos\theta_0 / \sqrt{1 - M_{ax}^2 \sin^2 \theta_o}$, and Ref. 1's "$\sin\theta_o$" into $\beta_{ax}\sin\theta_o / \sqrt{1 - M_{ax}^2 \sin^2 \theta_o}$. The final result for $\tilde{p}_{mB_R - nB_S}^{inc}$ now is

$$\frac{R_o \tilde{p}_{mB_R-nB_S}^{inc}(\theta_o)}{\rho U_{\alpha x}^2 \exp\left\{i \dfrac{mB_R \Omega L}{2c\beta_{\alpha x}^2}\left(\sqrt{1-M_{\alpha x}^2 \sin^2\theta_o}\, R_o - M_{\alpha x} z\right)\right\}} = \frac{B_R}{2\pi \beta_{\alpha x}^2 \sqrt{1-M_{\alpha x}^2 \sin^2\theta_o}}\, e^{-i(mB_R-nB_s-1)\pi/2}$$

$$\cdot\, \exp\left\{\frac{imB_R \Omega L}{2c\beta_{\alpha x}}\left(\frac{M_{\alpha x}}{\beta_{\alpha x}} + \frac{\cos\theta_o}{\sqrt{1-M_{\alpha x}^2 \sin^2\theta_o}}\right) z_{gl.}^*\right\} \tag{14}$$

$$\cdot \int_{R_h}^{R_t} dr^* \frac{u_{nB_s}(r^*) T_{nB_s}(r^*,\theta_o)\sin[\mu(r^*)]}{\rho U_{\alpha x}^2 L}\, J_{mB_R-nB_s}\left(\frac{mB_R \Omega L r^*}{2c}\, \frac{\sin\theta_o}{\sqrt{1-M_{\alpha x}^2 \sin^2\theta_o}}\right)$$

$$\cdot \left\{\frac{mB_R \Omega L}{2c}\left(\frac{\cos\theta_o}{\sqrt{1-M_{\alpha x}^2 \sin^2\theta_o}} + M_{\alpha x}\right)\sin[\upsilon_R(r^*)] + \beta_{\alpha x}^2 \frac{(mB_R-nB_S)}{r^*}\cos[\upsilon_R(r^*)]\right\}$$

The aerodynamic transfer function $T_{nB_s}(r^*,\theta_o)$ for the compact case ceases to be a function of θ_o, and Eq. 6, as is, supplies then the expression for $u_{nB_s} T_{nB_s} \sin\mu / \rho U_{\alpha x}^2 L$. For the noncompact case, one finds that this group function now takes on the form

$$\frac{u_{nB_s}(r^*)T_{nB_s}(r^*,\theta_0)\sin[\mu(r^*)]}{\rho U_{\alpha x}^2 L} = -\frac{\bar{u}(r^*)}{U_{\alpha x}} \cdot \frac{B_S}{2\pi} \cdot \frac{\Omega L}{2U_{\alpha x}} \cdot r^* \cos[\upsilon_S(r^*)]$$

$$\cdot \left\{ \sum_{\bar{n}=-\infty}^{\infty} e^{-i\pi(nB_S-\bar{n})/B_S} \frac{\sin[\pi(nB_S-\bar{n})/B_S]}{\pi(nB_S-\bar{n})/B_S} \int_0^{2\pi/B_S} d\tilde{\phi}\, e^{-i\bar{n}\tilde{\phi}-A[\tilde{\phi}-\phi_i(r^*)]^2} \right\} \quad (15a)$$

$$\cdot \frac{(1+i)}{\sqrt{\pi(1+M_r)}} \frac{1}{\sqrt{\dfrac{nB_S\Omega L}{2U_r}}} \cdot \frac{E\{\bar{c}(r^*)f(\theta_o)\}}{\sqrt{f(\theta_o)}} \quad ,$$

where

$$f(\theta_o) = \frac{nB_S\Omega L}{2c(1+M_r)} + \frac{mB_R\Omega L}{2c\beta_{\alpha x}^2}\left(\frac{\cos\theta_o}{\sqrt{1-M_{\alpha x}^2\sin^2\theta_o}} + M_{\alpha x}\right)\cos[\upsilon_R(r^*)]$$

$$\quad (15b)$$

$$\quad -\frac{(mB_R-nB_S)}{r^*}\sin[\upsilon_R(r^*)] \quad .$$

B.3   Incident Farfields in the Ground Reference Frame

Instead of Eq. 14, one now finds that

$$\frac{R_o \tilde{p}_{mB_R - nB_S}^{inc}}{\rho U_{ax}^2 \exp\left\{-\dfrac{imB_R \Omega}{1 - M_{ax}\cos\theta_o}\left(t - \dfrac{\hat{R}_o}{c}\right)\right\}}$$

$$= \frac{B_R}{2\pi} \frac{\exp\left\{-i(mB_R - nB_S - 1)\pi/2 + i\dfrac{mB_R \Omega L}{2c} z_{gl}^* \dfrac{\cos\theta_o}{1 - M_{ax}\cos\theta_o}\right\}}{(1 - M_{ax}\cos\theta_o)^2} \quad (16)$$

$$\cdot \int_{R_h}^{R_t} dr^* \; \frac{u_{nB_S}(r^*) T_{nB_S}(r^*,\theta_o)\sin[\mu(r^*)]}{\rho U_{ax}^2 L} \; J_{mB_R - nB_S}\left(\frac{mB_R \Omega L}{2c} \frac{r^*\sin\theta_o}{1 - M_{ax}\cos\theta_o}\right)$$

$$\cdot \left\{\frac{mB_R \Omega L}{2c}\cos\theta_o\sin[\upsilon_R(r^*)] + \frac{(mB_R - nB_S)}{r^*}(1 - M_{ax}\cos\theta_o)\cos[\upsilon_R(r^*)]\right\} \quad .$$

Eq. 6 again provides without changes the r^*-integrand factor $u_{nB_S} T_{nB_S}\sin\mu$ for the rotor blades with chordwise-compact loads. For the noncompact case, one obtains

$$\frac{u_{nB_S}(r^*) T_{nB_S}(r^*,\theta_o)\sin[\mu(r^*)]}{\rho U_{ax}^2 L} = -\frac{\bar{u}(r^*)}{U_{ax}} \cdot \frac{B_S}{2\pi} \cdot \frac{\Omega L}{2U_{ax}} \cdot r^*\cos[\upsilon_S(r^*)]$$

$$\cdot \left\{\sum_{n=-\infty}^{\infty} e^{-i\pi(nB_S - \bar{n})/B_S} \frac{\sin[\pi(nB_S - \bar{n})/B_S]}{\pi(nB_S - \bar{n})/B_S} \int_0^{2\pi/B_S} d\tilde{\phi}\, e^{-i\bar{n}\tilde{\phi} - A[\tilde{\phi} - \phi_t(r^*)]^2}\right\} \quad (17a)$$

$$\cdot \frac{(1+i)}{\sqrt{\pi(1+M_r)}} \cdot \frac{1}{\sqrt{\dfrac{nB_S \Omega L}{2U_r}}} \cdot \frac{E\{\bar{c}(r^*)f(\theta_o)\}}{\sqrt{f(\theta_o)}} \quad ,$$

where now

$$f(\theta_o) = \frac{nB_S \Omega L}{2c(1+M_r)} + \frac{mB_R \Omega L}{2c} \cos[\upsilon_R(r^*)]\cos\theta_o - \frac{(mB_R - nB_S)}{r^*}\sin[\upsilon_R(r^*)] \ . \quad (17\text{b})$$

B.4 Conversion of the Blade-Source Analysis in Sections A.2 - B.3 to Apply to the Rotor-First Stage in Fig. 2c

Again, the analysis of the fan stage as a source of noise, described above in Sections A.2 - B.3, addressed Fig. 2b's case of inlet guide vanes preceding a rotor. The purpose of this section is to modify all of that work to make it also fit the rotor-first arrangements shown in cutaway form in Fig. 2c and for whole engines in Figs. 1a - c. This second configuration has been the subject of numerous recent analyses, cf. Envia[10] for a "classical" problem of the Wiener-Hopf type, and Kousen & Verdon[15] for a CFD cascade solution in two dimensions.

In terms of parameter values, the rotor-first arrangement differs from the stator-first as follows:

(a) The rotor's viscous wakes clearly belong to a higher Reynolds number flow, and their "laminar" widths are accordingly narrower;

(b) Their "lean" could be greater than for the stator-first case (cf. Envia[10]), because ...

(c) Both the axial and circumferential components of the rotor's exhaust freestream $U_{B>}(r)$ would be numerically greater than $U_{S>}(r)$ for the stator-first case: Momentum conservation requires that the rotor's performance thrust and torque be reflected in "kicked-up" values for these quantities;

(d) The final exhaust angle for the stage would now have a practically small chordwise-average value, unlike the values suggested in Figs. 2a and 2c, and more like those in Fig. 1c.

In terms of the character of the unsteady-aerodynamics problem, and of the resulting

21

noise from the downstream blades, the stator-first and rotor-first pictures differ as follows:

(a) In Section A.3 the stator's wakes were spatially stationary with respect to the downstream rotor, which cut through them. Now they are obviously in the nature of convected gusts passing over the downstream stator blades at the collectively sampled blade-passage frequency plus harmonics, which remain the same as on Sections A.2 - B.3; i.e., given by $mB_R\Omega$. The airfoil-felt disturbance wavenumbers are now given by $mB_R\Omega/U_r$ rather than by $nB_s\Omega/U_r$.

(b) The character of the convected wave equation in the "propagation" part of the problem does not change, because the formulation in Eq. 5b neglects the swirl component of $U_{s>}$ and $U_{B>}$ for the two situations in Figs. 2b,c, and takes U_{ax} as applying throughout. I.e., as modelled, for example, by Envia[10] (again, his Eq. 2.11d), and in Fig. 2d here, the blade-radiation part of the analysis is the same for rotor-first and stator-first configurations.

One concludes from all of the above that the following conversion key carries the stator-first source theory developed in A.3 - B.3 to apply to the rotor-first configuration:

(1) Exchange the symbol B_R, which appears in the numerator of the coefficient immediately to the right of Eqs. 14 and 16, for B_s, the number of now-radiating stator blades. Also switch in those expressions the local pitch angle $\upsilon_R(r)$ of the radiating blade section to be $\upsilon_S(r)$;

(2) The index "nB_s" of the $u_{nB_s}T_{nB_s}$ group that denotes the submodel for the unsteady load on the radiating blades now becomes mB_R, the index for the new convected wavenumbers striking the downstream stator;

(3) Accordingly, in the compact-loads model of Eq. 6, the nB_s part of the Sears function, and B_s itself, become mB_R and B_R, respectively. The blade chords $\bar{c}(r^*)$ now refer to the stator rather than to the rotor, and again $\upsilon_S(r^*) \to \upsilon_R(r^*)$;

(4) For the noncompact load results in Eqs. 15a,b and 17a,b, items (2),(3) just above apply as well in Eqs. 15b, 17d.

One final remark: Sections A.1 through B.3 dealt with a radiating rotor with blades that obviously did not reach the cowl's inner wall. I.e., the tip radius R_t was less than the cowl's

radius "a". The same is clearly not true for radiating stator blades, which do connect structurally to the cowl. For reasons of numerical convergence, however, we assume here that the effective radial extent of stator radiation is again less than "a". The justification is a consistent use of strip theory for the now-downstream stator blades, together with a picture of rotor wakes that do not extend radially outboard to the cowl's inner wall at $r=a$.

IV A CANONICAL MODEL OF COMBINED LEADING- AND TRAILING-EDGE DIFFRACTION FOR THE COWL: ACOUSTIC SHIELDING BY AN "UNWRAPPED" DUCT

A. MOTIVATION

Figs. 4a,b show the geometry under consideration: Fig. 1a's cylindrical cowl has been unwrapped into a strip of width equal to the original cowl chord L. The length of that strip, which corresponds to the cowl's original spanwise extent $2\pi a$ as a ring wing, will now become irrelevant as per the rules of the Geometric Theory of Diffraction (GTD)[16], which this section adopts. GTD concludes that only one point on the cowl's inlet and outlet circular edges plays a role in the diffraction process: That which is closest to both the interior insonifying source and the external receiving field position.

This somewhat narrow application, or interpretation of that theory, obviously neglects the multiple reflections that the cowl's actual waveguide geometry generates in its interior (more on this under Section V.B.1d). The unwrapped shape in Fig.4b provides a spurious infinite-medium reservoir "below" the source. The true geometry in Fig. 4a instead confines the acoustic energy of those lost "lower" rays to the cowl's finite internal cylindrical space. The duct's interior becomes a classical "whispering gallery" to those rays, which eventually work their way to the two "primary" edges shown in Fig. 4b and affect the indicated listener through additional edge diffractions and possible specular reflections.

The unwrapped-cowl model is nonetheless useful because it provides an estimate of the best shielding performance possible under the assumption that the duct's waveguide effects, i.e., its multiple reflections, etc., could be completely eliminated through absorption by a liner. The

remaining physical picture would ideally then justify the unwrapped-geometry limit in Fig. 4b. These long overdue canonical calculations will also help interpret the formal predictions of duct diffraction in Section V.

The insonifying field in this canonical sub-study will be that of a single three-dimensional monopole source of volume-velocity strength $\ddot{Q}_o$. The same freestream of subsonic Mach number M_{ax} of Figs. 2b-d will continue to tilt all of the acoustic fields in the downstream direction: incident, reflected, and edge-diffracted (more on ray tilting in V.A).

B. BRIEF BACKGROUND OF SCREEN-DIFFRACTION PROBLEMS WITH AND WITHOUT FLOW

The classical problem of diffraction by a rigid screen in a still medium produces a field that applies equally to the velocity potential and the pressure. That is because the two quantities differ then only by a multiplicative constant, namely, $i\omega\rho$, as in the statement

$\Delta p = -\rho\partial(\Delta\Phi)/\partial t = i\omega\rho\Delta\Phi$, which relates the "diffraction load" Δp across the screen to a similar jump in potential Φ. Either dependent variable is furthermore found to vanish as the square root of the distance to the screen's edges. And both p and Φ are zero over the coplanar extension of the screen.

The presence of a mean flow changes that picture radically. A leading-edge screen then generates a diffraction load Δp that blows up on approach of the screen's vertex, while $\Delta\Phi$ acts just as it did in the flowless problem (Fig. 4c). The reason for Δp's change in behavior is that now the relationship connecting it to $\Delta\Phi$ contains a spatial derivative:

$\Delta p = -\rho D(\Delta\Phi)/Dt$, which on approach of the edge at z=0 yields

$\Delta p \sim -\rho U_{ax}\partial(\Delta\Phi)/\partial z \sim z^{-1/2}$, since $\Delta\Phi \sim z^{1/2}$ as before.

If the screen is a "trailing-edge" one, with M_{ax} flowing past it as shown in Fig. 4d, then Δp is zero along the screen's wake extending to $z = +\infty$, again as in the flowless problem (where there was no wake), while $\Delta\Phi$ should now be finite rather than zero there.

Candel[17], and then Amiet[18], exploited these well-known features, of flow versus nonflow problems for the screen geometry, to construct leading- and trailing-edge pressure solutions for

$M_{ax} \neq 0$ for incident fields of the "appropriate" kind. The more relevant of the two studies is Amiet's because it addresses the point-source problem in our Fig. 4a (Candel considers a plane wave incident from infinity).

By incident fields of the "appropriate" kind we mean the following: The driving point source in Amiet's leading-edge solution could afford to be a standard velocity source of volume strength $\ddot{Q}_o$. The primary dependent variable in the boundary value problem was accordingly the velocity potential, since its particular solution (without the barrier) could be immediately connected to the point velocity source through a gradient operator that did not include the freestream U_{ax}. Amiet then obtained, or could have obtained, the associated pressure field through a standard post-application of the operator $-\rho D/Dt$ to the independent time and axial field variables. Summarizing then, the leading-edge problem for $M_{ax} \neq 0$ has a straight-forward solution for the velocity potential and for the pressure field, for a standard velocity source of strength $\ddot{Q}_o$ generating the incident field.

The same is not true of the trailing-edge screen in Fig. 4d here. There is then no analogy with a flowless problem unless the primary dependent variable is the pressure throughout the picture. That includes an exchange of the true velocity source driving the system, $\ddot{Q}_o$, for an artificial "pressure" source, say of strength "P_o". Amiet's (and Candel's) leading- and trailing-edge solutions are therefore irreconcilable because their source fields are incompatible.

C.   POSTULATED RECONCILIATION OF EXISTING LEADING- AND TRAILING-EDGE CANONICAL SOLUTIONS

One replaces the pressure source P_o cited above with the product of $-\rho\ddot{Q}_o$ and the "source-adjoint" version of the standard substantial derivative:

$$P_o \rightarrow -\rho\ddot{Q}_o \left(\frac{\partial}{\partial t} - U_{ax} \frac{\partial}{\partial z^.} \right) \tag{18}$$

25

The spatial derivative is with respect to the source position z*, and the coefficient $U_{\alpha x}$ in the ordinary substantial derivative has been replaced by $-U_{\alpha x}$.

The application of the right side of Eq. 18 to Amiet's trailing-edge solution for $M_{\alpha x} \neq 0$, after removal of his implied symbol P_o, contains the following features and we therefore argue is the correct solution for the trailing-edge problem driven by a velocity source:

(1) The problem's particular solution is recoverable as the field-point vector $\vec{x}$ approaches the incident source point $\vec{x}^*$, given that $\partial/\partial z^* = -\partial/\partial z$. I.e., the solution captures radiation by the velocity source in free space, a weak but necessary requirement;

(2) The resulting solution still satisfies the Kutta condition and flow tangency. The new construction has simply exercised its right to interpret the original complete solution as the barrier problem's fundamental influence function. The operation in Eq. 18 builds up a more complicated field from that original total "Green's function";

(3) $\Delta\Phi$ continues to be nonzero along the screen's wake. The inversion of the standard substantial derivative $-\rho D/Dt$, through the integral operation

$$- \frac{e^{i\omega z/U_{\alpha x}}}{\rho U_{\alpha x}} \int_{-\infty}^{z} d\tilde{z} \, \frac{e^{-i\omega \tilde{z}/U_{\alpha x}}}{\rho U_{\alpha x}} \quad ,$$

does not "undo" the right side of Eq. 18 when $\tilde{z}$ refers to the axial positions of the virtual sources that make up the screen's surface. Eq. 18 does not "trivialize" the associated solution for the potential: the shed wake stays (recall Eqs. 13-17 of Ref. 1).

We avoid writing down the complicated result of applying Eq. 18 to Amiet's trailing-edge solution[18]. The differential operation yields derivatives of Fresnel integrals, etc., that provide no great new insights into the nature of the diffraction process. Section E below will present sample results from the numerical implementation of that unstated expression.

D.   HIGH-FREQUENCY JUSTIFICATION OF A COMBINED LEADING- AND TRAILING-EDGE DIFFRACTION MODEL

The end products of Section C are leading- and trailing-edge solutions for $M_{ax} \neq 0$ driven by the same velocity source of strength $\ddot{Q}_o$. They may now be referred to a common coordinate system, e.g., to one centered at the field position of the driving monopole source, and added to generate an aeroacoustic diffraction model for the wing of finite chord earlier discussed in Fig. 4a. The implied assumption is that the edges decouple aerodynamically for the relatively high frequencies of interest, viz., for $\omega L/(2c\beta_{ax}^2)$ in the range of 20. Cf. Peake,[19] for a recent development of a leading-edge solution for a quarter-wing in unsteady supersonic flow, based on Landahl's[20] chordwise decoupling of edge behaviors. Ring-shaped signals created at our cowl's leading edge directly by $\ddot{Q}_o$ would also spread downstream quasi two-dimensionally, and their amplitude at the trailing edge would have decayed at least by the factor $\{\omega L/[c(1+M_{ax})]\}^{-1/2}$. Pressure signals similarly generated at the trailing edge would be cut down by the even smaller multiplier $\{\omega L/[c(1-M_{ax})]\}^{-1/2}$ on reaching the leading edge.

E.   NUMERICAL PREDICTIONS OF NOISE SHIELDING BY THE , TWO-EDGED CANONICAL MODEL FOR $M_{ax} \neq 0$: EFFECTS OF COWL CAMBER AND TAPER

The set of canonical diffraction calculations about to be discussed generalizes those of Dittmar[2a], who also invoked diffraction by a rigid screen in the context of the cowl but considered only the flowless case.

Fig. 5a shows the directivity pattern of incident (p^{inc}), and incident-plus-diffracted (total) pressures for a leading-edge screen. This solution is immediately available from Amiet's work.[18] The three-dimensional point monopole is $30°$ off the screen at a dimensional distance R* away from the vertex such that $\omega R^*/c = 10$. The picture is the same as the sketch on the right side of Fig. 4b but with the trailing-edge point set at $z = +\infty$ rather than at L/2. M_{ax} is .8. The upper part of Fig. 5a's directivity pattern contains the shadow zone. The lower part contains the spatial region of specular reflections and a transitional zone connecting it to the shadow. The directivity pattern of the incident field would be a perfect circle were it not for the freestream, which distorts it into an oval shape. The gap between p^{inc} and the total pressure on the shadow-zone (upper) half of the figure indicates the degree of shielding provided by the rigid barrier as a

zone (upper) half of the figure indicates the degree of shielding provided by the rigid barrier as a rigid leading-edge wing.

Fig. 5b plots similar directivity patterns for the trailing-edge solution, with the same velocity source $\ddot{Q}_o$ now supplying the incident field for the first time (cf. the analytic construction under Section C above).

Fig. 6 adds coherently the two total-pressure fields in Figs. 5a,b and thereby arrives at the diffracted field of the wing of finite chord L displayed in Fig. 4b. Whereas the shadow-zone patterns of the individual leading- and trailing-edge cases in Figs. 5a,b were smooth, their combination in Fig. 6 now contains the fringe typical of two effective "diffraction sources", one at each of the wing's two edges a distance L apart.

Fig. 7a checks that Fig. 6 contains the right number of lobes within a sector roughly defined about the normal direction in the shadow zone. Fig. 7a plots the combined phase factors of two sources of arbitrary but equal amplitude, again separated by L. Fig. 7b checks the parts of Figs. 5a,b that are less physically relevant to our purposes though important as diagnostics: the roughly-equal lobe patterns of specular reflections generated by both semi-infinite screen problems on their illuminated side. One of the two curves in Fig. 7b is the total pressure from the leading-edge solution. The other is from the even more primitive problem of a source near an infinite wall, with $M_{\alpha x} = .8$ again. The lobe patterns differ at the beginning of the zone of full illumination, as they should, but then quickly merge as required.

Fig. 8 generalizes the two-barrier construction of Fig. 6 by staggering the two screens to model the diffracting ends of the generator curve of a "truer" geometry, shown below as a bell-shaped cowl of the same axial length as the straight duct in Fig. 6. The slope of its generator is zero at both the inlet and outlet. The source is now closer to the trailing edge; i.e., $\omega R \cdot / c = 3.34$. The fringe pattern is less textured because the diffracting strengths of the two ends differ substantially from what they were in Fig. 6. The overall depth of the shadow, however, is about the same as in Fig. 6.

Fig. 9 "pushes" the two-edge screen model by tilting the edges relative to each other. Otherwise the picture is the same as in Fig. 8. The tilted screens are a "tougher sell" now as a

28

model for the cowl shape, as depicted at the bottom of Fig. 9, because they require that the freestream also be tilted, but in different directions following the edges. The shadow softens, especially near the horizontal direction, because the source is now more "exposed": the leading edge's angle relative to the source is now greater by $20°$ than it was in Fig. 8; the trailing-edge angle is greater by $25°$.

The main conclusion of Figs. 6 through 9 is that over a fairly large sector about the horizontal none of the three two-edge models provides substantial shielding of noise. The stipulated use of "steering" of the cowl's virtual dipoles to reduce on-axis noise is therefore not really practical unless the fundamental mode index $B_R - B_S$ of the incident field is very high. The conclusion holds even for the relatively high realistic frequencies investigated through these canonical models. Fig. 10 summarizes why this is so. The remaining calculations will use the rigorous cowl-diffraction model to explore other means of achieving reductions of near-axis noise from ducted rotor/stator interactions, e.g., through liner dissipation coupled formally to the short cowl's diffraction effects.

V   SAMPLE PREDICTIONS OF FORMAL COWL DIFFRACTION FOR STATOR-FIRST AND ROTOR-FIRST SYSTEMS

A.   KINEMATICS OF RAY TILTING IN A UNIFORM FREESTREAM

The purpose of this subsection is to add a few remarks to the canonical groundwork of IV. The new comments will help interpret the calculations discussed below for the rigorous diffraction of fan noise by the cowl. The issue at hand here is the expected ray-tilting effect of the uniform freestream on the cowl's pattern of reflection and diffraction lobes.

Fig. 11a shows a pair of typical rays shooting out of an arbitrary point of radiation in the fan stage. One ray travels upstream and the other downstream. Both do so at the standard speed of sound "c" relative to the medium that convects them. The figure suffers no loss of generality in assigning the cowl's midaxis station to the two rays' point of origin. The cowl's inlet ring appears as a point, at a "visual", or nominal angle $\theta_{o,nom}^{inlet}$ with respect to the source. The corresponding outlet value is $\theta_{o,nom}^{inlet}$; it is equal to the inlet value for the special arrangement considered in the figure.

The lower part of the picture gives the solutions for the ray tilt needed to clear the cowl in both upstream and downstream directions. The upper part of the figure displays the cowl's optical, or geometric shadow $\Delta\theta_o^{shadow}$ along with a sector of equal width spanning the tilted ray directions. To be precise: the cowl's acoustic shadow, in the presence of the flow, remains symmetric about the midaxis and matches the optical shadow. However, within the upstream complement of the figure's uppermost sector, i.e., for field angles θ_o satisfying $\theta_o < \theta_{o,nom}^{inlet}$, the directional content of the unblocked ray field would be limited to the angle $\theta_{o,act}^{inlet}$.

A corresponding observation applies to Fig. 11a's downstream direction, reconsidered in Fig. 11b for a typical ray that does not clear the cowl. The contents of ray directions for incident and cowl-reflected rays include the indicated sector, which due to the flow is greater than the nominal.

B.   RIGOROUS PREDICTIONS OF COWL DIFFRACTION FOR SECTION III.B'S
      INCIDENT FIELDS

B.1   Calculations for a rigid-walled (unlined) Cowl

B.1a Parameter Values

The parameters for the cowl and the fan stage are: The number of rotor blades B_R is 16. The number of stator blades B_S is 22 (following the Advanced Ducted Propeller case in Meyer's paper[7]). The fundamental value of the spin-mode index $v = mB_R - nB_S$ is therefore -6, for the first temporal harmonic counter m=1 and the stator's first Fourier counter n=1. The flight Mach number M_{ax} will be .4 for all of the calculations. The rotor's RPM is 4000, yielding a Blade-Passage Frequency (BPF) of 1067 Hz. The cowl's length L is 8 feet and its dimensional radius aL/2 is 2.5 feet. The resulting width $\Delta\theta_o^{shadow}$ of the cowl's geometric shadow is 78° for a blade-tip radiating point (see engine insert at the top of Fig. 12). The calculations do not include the engine's afterbody, which is transparent both hydrodynamically and acoustically. The value of $(\omega/c)(aL/2)$ is 15.2. Wake lean is neglected for simplicity's sake: $\phi_t(r^*) = 0$. The wake parameters "A" and $\bar{u}/U_{ax}$ have the constant values $(2/\pi)^2\log_e 10$ and .2, respectively.

The present lifting- and nonlifting-surface theory of cowl diffraction does not invoke duct modal concepts explicitly, though it nonetheless "contains" them. I.e., the new theory makes no explicit use of the fact that at the BPF at least three radial modes have cut on in a hard-walled duct lacking a centerbody: the eigenvalue problem for an infinite rigid-walled cowl is $J_v'(\gamma_t a) = 0$, which for v=∓6 yields $\gamma_t a$=7.2, 11.6, 15.4, ... for t=1,2,3,... The associated cut-on values for $(\omega/c)(aL/2)$ are given by $\beta_{ax}\gamma_t a$ (see, for example, Fleeter[3]), which for M_{ax}=.4 (β_{ax}=.92) gives that $(\omega_t/c)aL/2$=6.6, 10.7, and 14.2 as the three relevant values below the fundamental operational value of $(B_R\Omega/c)aL/2$, i.e., below 15.2.

Regarding chordwise compactness versus noncompactness for the radiating blades: They will be chordwise compact at the BPF and noncompact at the first overtone, 2xBPF. This modelling decision is based on a conclusion reached by Amiet[21] for an airfoil's unsteady lift at high frequencies and speeds. It turns out that values of $(\omega/c)[\bar{c}(r)L/4]/(1 - M_r^2)$ greater than $\pi/4$ justify the use of the leading-edge solution alone, which in the present case is the

chordwise pressure distribution given in Eq. 10. Values of the parameter lower than $\pi/4$ conversely call either for a multiply corrected noncompact solution, or for a fallback on the compact Sears solution given here in Eq. 6. The chord dimensions used in our calculations are such that the BPF value of Amiet's chord parameter is roughly .54 for airfoil sections near the tip of the radiating blades (i.e., lower than $\pi/4$). The appropriate model is therefore a chordwise-compact one. At the first overtone, however, the parameter value doubles to 1.085 and crosses to the noncompactness regime of Section III.A.5b.

B.1b   Predictions for an Academic Stator-First, Rotor-SecondFan Stage

Fig. 12 documents an example calculation of diffraction by a rigid cowl for the study's only reported stator-first case. The frequency is blade-passage. The reference frame of the directivity pattern is that relevant to community noise (Section III.B.3). The solid curve displays the rotor's incident field in the absence of the cowl ($20\log_{10}$ of Eq. 16, etc.). The dashed curve is the total field obtained from the phased sum of incident and cowl-diffracted fields. The shielding performance of the rigid-walled cowl is mixed, with the original incident field intertwining the "total" curve.

B.1c   Predictions of Diffraction of Stator Noise by an Unlined Rigid Cowl: m=1, the BPF

The remaining calculations address the rotor-first, stator-second configuration of current interest to civil aviation. The flow parameters have been adjusted artificially to keep Fig. 12's radial distribution of rotor-blade twist for the now-radiating stator blades. The airfoil disturbance wavenumbers are now given by $mB_R\Omega/U_r(r^*)$ rather than by $nB_S\Omega/U_r(r^*)$, as explained in III.B.4. Again, $U_r(r^*)$ is artificially the same as in Fig. 12, just as the shape and amplitude of the wake, etc., are kept the same.

Fig. 13a plots incident and total fields for a ground observer. The frequency is again blade-passage and the radiating stator blades are chordwise compact. The cowl's mixed shielding performance is similar to that of Fig. 12. The lower overall levels of this rotor-first calculation relative to those in Fig. 12 are chiefly attributable to the difference in values of the relevant wake harmonic u_{B_S} versus u_{B_R}, which in Fig. 12 had a much higher value due to the fact that $B_R=16$ is significantly lower than $B_S=22$.

Fig. 13b compares Fig. 13a's ground prediction (dashed) for the total field to that on the aircraft's frame of reference (solid). Even for the relatively low Mach number of these cases, i.e., for $M_{ax}=.4$, the two patterns differ considerably. Community noise is significantly higher in the flight direction while cabin noise gets washed downstream, both according to expectations. Fig. 13c shows similar results for the incident field alone.

Fig. 13d is a diagnostic comparison of the cowl's complete scattered field and the stator blades' incident field. The figure has tentatively labelled the parts of the directivity pattern associated with the simple, one-bounce reflection phenomenon depicted in Fig. 11b and originally explored quantitatively in Figs. 5a,b and 7a,b. The number of lobes in the specular zones makes rough sense upon taking account of the difference in frequencies and Mach numbers between Fig. 13d and the earlier canonical results. The purpose of Fig. 13d is both to support and question the rigorous total field prediction in Fig. 13a: The scattered field appears to have the correct spatial structure, and yet the predicted shielding in Fig. 13a is far from the impressive conclusions reached by the canonical model. A hypothesis for the rigorously calculated cowl performance will be offered below for the unlined case.

B.1d Predictions of Cowl Diffraction of Stator Noise by an Unlined Cowl: m=2, the First Overtone of the BPF

Figs. 14a-e are the m=2 versions of Figs. 13a-d: The frequency is now twice blade-passage and the radiating stator blades have become chordwise noncompact from root to tip, thereby calling for a computational switch from Eq. 6 to 11, etc. The spin-mode index ν has climbed from -6 to +10 for "n" still equal to 1. Fig. 14a shows incident (solid) and total (broken) fields for an observer on the aircraft's reference frame. Fig. 14b is for a ground-based listener. The levels in both figures are considerably lower than those in Figs. 13a,b for the BPF, for this particular sample propulsor case.

The cowl's shadowing performance displayed by Fig. 14a is somewhat better than that of blade-passage. It is still, however, below the expectations raised by the canonical model. Figs. 14c,d compare again the incident to the total field for aircraft and ground-based observers. Fig. 14e contains the overtone's diagnostic plot of incident and cowl-scattered fields. The upstream

and downstream lobe patterns for specular reflections are now clearer, and therefore more credible than they were at blade-passage. The potentially "shadow-producing" central zone is likewise more monolithic. The question remains regarding why the cowl's shielding performance is at best only moderate.

We believe these duct diffraction calculations to be correct, if for no other reason because the boundary-value problem of the rigid cowl as purely "lifting" object is a fairly straightforward one (as opposed to when the cowl is lined, to be discussed below). All of the numerical results reported here have converged with respect to every computational parameter in the lifting-surface theory, and, again, the predicted scattered fields contain the physical features expected of them (the specular lobe patterns, etc.).

One promising hypothesis for the lack of a deep shadow in these rigorous calculations of cowl diffraction is the ever presence of a pair of modes whose cut-off and cut-on frequencies straddle the frequency of interest, e.g., the BPF. The cut-on member of the pair would naturally have the greater impact. At conventional cut-on, based on "infinite-duct thinking," there is a severe mismatch between the axial impedance of the fluid inside versus that outside the cowl. The fluid within the duct behaves then as an axially incompressible air column with radial corrugations corresponding to the acoustic wavenumber divided by the Prandtl-Glauert factor β_{ax}. I.e., the mode's "z" wavenumber becomes by definition zero. The duct's interior becomes an effective resonant space with respect to the two straddling modes.

Figs. 15a,b, respectively from Meyer[7] and the author's Ref. 8, support that working hypothesis. Fig. 15a shows computed reflection coefficients versus frequency for an inlet duct driven from within by the fan stage of an Advanced Ducted Propeller having the same number of rotor and stator blades as that of our calculations. The reflections are largest at cut-on for the reasons just cited, viz., due to the forced coexistence of an axially hydrodynamic interior and a standard wave-bearing exterior. What is interesting, as well as important to the present argument, is that the amplitudes of the reflections remain fairly high over wide bands of frequencies: the cowl's interior leaks energy to the exterior but nonetheless stays largely locked in a semi-resonant state. The resistance supplied by the exterior is not enough to keep that from

happening.

Fig. 15a is actually a recreation of Fig. 15b in a different guise. The solid curve in this second figure plots the formally computed power radiated by a single axial dipole within a rigid unflanged duct of finite length. There is no freestream. The ordinate has been normalized by the dipole's power output in freefield, so that values above zero represent an amplification of the leaking acoustic field due to the interior's quasi-resonant state. Fig. 15b's solid curve remains consistently above that zero level even at the highest frequencies "k" in the graph (the abscissa k stands for $\omega L/2c$ in the nomenclature of this report). The author further recalls that the resulting amplified directivity patterns (not published in Ref. 8) did not always beam away from the duct's nominal shadow to collect in the duct's unprotected sectors, so that much of the added radiation in fact went to fill in the shape's expected shadow. This comment would likely apply also to Meyer's predictions, perhaps even more so because they address relatively high-index spinning modes with naturally low near-axis levels (Meyer does not report directivity patterns in Ref. 7).

To summarize the dual message of Figs. 15a,b: 15a proves that inlet reflections near cut-on are high over bands of frequencies that are surprisingly broad; and Fig. 15b concludes that even though the semi-resonant fluid interior is reactively isolated from the exterior, the same is clearly not true of its resistance. The resulting power output of the partly encased dipole is greater than it would have been in freefield, over wide bands of frequencies: The true waveguide character of the rigid cowl largely nullifies the shielding predicted canonically for the unwrapped shape. Section B.2 will explore whether practical arrangements of a lossy liner might sufficiently dampen the interior's quasi-resonances and thereby allow the waveguide system to approach the ideal canonical state.

B.2   Calculations of Cowl Diffraction for a Lined Cowl

B.2a   Preliminary Remarks

The liner calculations will address only the BPF (m=1). It was earlier found that for the stator blades in question Amiet's[21] chordwise compactness parameter produced a typical value of .54. That number is lower than the $\pi/4$ rough dividing line beyond which noncompactness

effects are so pronounced that a leading-edge solution is a good approximation to the exact inversion of the Possio kernel and its convolution with the input gust.

For no particularly compelling reason, however, the brief liner study about to be discussed does not invoke the chordwise compactness condition even though the radiating stator blades meet it from root to tip (i.e., ".54<<π/4"). The calculations instead treat all blade loadings as chordwise noncompact. The stator's incident field will therefore not match exactly those earlier computed via the alternate chordwise-compact code.

All liner cases will use the same ring-band patch. The cases examined will shift that patch axially along the cowl's interior to determine the effect of its position on overall cowl shielding. The locally reacting microducts that make up the liner's surface will be tuned to the driving frequency, i.e., to the BPF: RPM_{choice} in Eq. A.9 will be the rotor's RPM. The loss factor η will be unity. The movable lined ring band will measure one-third of the cowl's length L: $L_{liner}=L/3$.

All predictions will be for the ground reference frame relevant to community noise.

B.2c   Formal Diffraction by a Lined Cowl: Numerical Results

Fig. 16a shows predictions of incident and total fields for an inlet placement of the liner segment (see upper engine sketch). The cowl's shielding performance is somewhat improved over that earlier displayed in Fig. 13a for the perfectly rigid case. Fig. 16b compares the incident field to that scattered by the now-partially lined system. This second field differs significantly from its rigid-cowl version in Fig. 13d. Fig. 16b's specular lobes appear split into smaller sub-lobes, more so in the forward than in the rear direction. The scattered field remains roughly unaffected by the inlet liner for angles near $\theta_o=90°$.

Figs. 17a,b repeat Figs. 16a,b but for a central lined segment (for manufacturing and maintenance reasons, this case is probably only academically interesting). The cowl's shielding performance in Fig. 17a appears to be better yet than in Fig. 16a, except for some degradation along the strong forward lobe around $\theta_o=25°$.

Figs. 18a,b are for an outlet liner. This configuration does not appear to perform globally as well as the other two, although it reduces noise somewhat along the downstream axis as

expected. The outlet liner has not changed much the three forward lobes in Fig. 18b's scattered field upon comparison to what they were in Fig. 13a. That is again according to physical expectations: those lobes are chiefly due to a local bounce-off of stator noise striking once the nearby untreated inlet.

Fig. 19 collects the total fields from Figs. 16a-19a in order to showcase their differences. The picture's conclusion is that each of the three liner layouts enhances the cowl's rigid shielding performance in a roughly understandable way: the inlet liner dissipates some of the forward fan noise and so, reduces somewhat the total field within the main forward lobe at $\theta_o=25°$; and (2) the outlet liner similarly cuts down the already-low rearward radiation; (3) the center liner sends slightly less acoustic energy both forward and backward than the rigid case. The radial content of that energy appears to be such, that while it improves the cowl's shielding performance for θ_o near 90°, it does so in part at the expense of fore and aft radiations.

VI CONCLUSIONS

(1) The project has produced a fairly sophisticated model for the cowl's incident field due both to stator/rotor and to rotor/stator interactions. The source analysis has relied on strip aerodynamics, although all blades and impinging wakes were otherwise three-dimensional. The blades were twisted from root to tip and their spanwise-variable chords were aeroacoustically wide, or noncompact. The theory has generated formal expressions for both the nearfield pressures and fluid particle velocities along the cowl's diffracting walls.

(2) Part of the work centered on the development of a novel set of circumferentially unwrapped, but axially warped canonical models to predict the ideal performance of a cowl of arbitrary generator curve under conditions of perfect absorption for its interior. The remaining acoustic rays were made to diffract around the ends of a two-edged generalized screen in a flow. Those canonical calculations determined that cowl camber and/or taper should be inefficient agents for steering rotor/stator noise away from near-axis directions. The numerical predictions of the canonical models also supplied important benchmark features against which the physical content of the later calculations of rigorous cowl diffraction could be judged.

(3) The formal predictions of cowl diffraction of the rotor/stator incident fields, described under (1) above, led to the following conclusions: (a) an unlined system should perform at best moderately, whether its insonifying blades are chordwise-compact or noncompact, and both for the blade-passage frequency and for its overtone. (b) A lined cowl should perform somewhat better, with typical shieldings in the range of several dB. That higher performance came to be roughly consistent here with one's expectations: an inlet liner has its greatest effects in the forward direction, etc.

ACKNOWLEDGEMENTS

REFERENCES

1   R. Martinez, "Aeroacoustic Diffraction and Dissipation by a Short Propeller Cowl in Subsonic Flight", NASA CR 190801 (April 1993); cf., also by the author, "Liner Dissipation for an Acoustically Driven Propeller Duct", AIAA Paper 93-4426, 15th Aeroacoustics Conference, Long Beach, CA , October 1993.

2   J.H. Dittmar, (a) "An Estimate of the Noise Shielding on the Fuselage Resulting from Installing a Short Duct Around an Advanced Propeller," NASA TM 100262, 1988; (b) "Effects of Long-Chord Acoustically Treated Stator Vanes on Fan Noise, I: Effect of Long Chord" (with J.N. Scott, B. Leonard, and E.G. Stakolich), NASA TN D-8062, Oct. 1975.

3   S. Fleeter, "Active Control of Turbomachinery Discrete Tones," NOISE-CON 94, Ft. Lauderdale, FL, May 1-4, 1994, pp. 379-388.

4   D.B. Hanson, "Unsteady Coupled Cascade Theory Applied to the Rotor/Stator Interaction Problem," DGLR/AIAA 14th Aeroacoustics Conf., AIAA Paper 92-02-084, 1992, Aachen, Germany.

5   M.K. Myers and J.H. Lan, "Sound Radiation from Ducted Rotating Sources in Uniform Motion," AIAA Paper 93-4429, 15th Aeroacoustics Conf., 1993, Long Beach, CA.

6   W. Eversman and I. Danda Roy, "Ducted Fan Acoustic Radiation Including the Effects of Nonuniform Mean Flow and Acoustic Treatment," AIAA Paper 93-4424, 15th Aeroacoustics Conf., Long Beach, CA, Oct. 25-27, 1993.

7   H.D. Meyer, "Effect of Inlet Reflections on Fan Noise Radiation," AIAA Paper 93-4427, 15th Aeroacoustics Conf., Long Beach, CA, Oct. 25-27, 1993.

8   R. Martinez, "A Boundary-Integral Formulation for Thin-Walled Shapes of Revolution," J. Acoust. Soc. Am., Feb. 1990, 87(2), pp. 523-531.

9   M.A. Goldstein, "Scattering and Distortion of the Unsteady Motion on Transversely Sheared Mean Flows," J. Fl. Mech., 1979, Vol. 91, Part 4, pp. 601-632.

10 E. Envia, "Influence of Vane Sweep on Rotor/Stator Interaction Noise," NASA CR 187052, Dec. 1990.

11 M.V. Lowson, "Theoretical Studies of Compressor Noise," NASA CR 1287, March 1969.

12   M.A. Goldstein, Aeroacoustics, McGraw Hill, 1976.

13   J. J. Adamczyk, "The Passage of an Infinite Swept Airfoil Through an Oblique Gust", NASA CR-2395, 1974.

14   R. Martinez and S.E. Widnall, "Unified Aerodynamic-Acoustic Theory for a Thin Rectangular Wing Encountering a Gust", AIAA J., 18 (6), 1980, pp. 636-645.

15   K.A. Kousen and J.M. Verdon, "Active Control of Wake/Blade-Row Interaction Noise," AIAA Paper 93-4351, 15th Aeroacoustics Conference, Long Beach, CA, Oct. 1993.

16   J. B. Keller, "Geometrical Theory of Diffraction", J. Opt. Soc. Am., 52(2), 1962, pp. 116-139.

17   S. M. Candel, "Diffraction of a Plane Wave by a Half Plane in a Subsonic and Supersonic Medium", J. Acoust. Soc. Am. 54 (4), 1973, pp. 1008-1016.

18   R. K. Amiet, "Unified Aeroacoustics Analysis for High-Speed Turboprop Aerodynamics and Noise", Vol. II: Development of theory for Wing Shielding, NASA CR 185192, May 1991.

19   N. Peake, "The Unsteady Lift on a Swept Blade Tip", to appear in the Journal of Fluid Mechanics.

20   M.T. Landahl, Unsteady Transonic Flow, 1961, Pergamon; e.g., p. 28.

21   R.K. Amiet, "High Frequency Thin-Airfoil Theory for Subsonic Flow", AIAA Journal, 14(8), (Sept. 1976) pp. 1076-1082; see discussion beginning on new paragraph after Eq. 20.

(a)
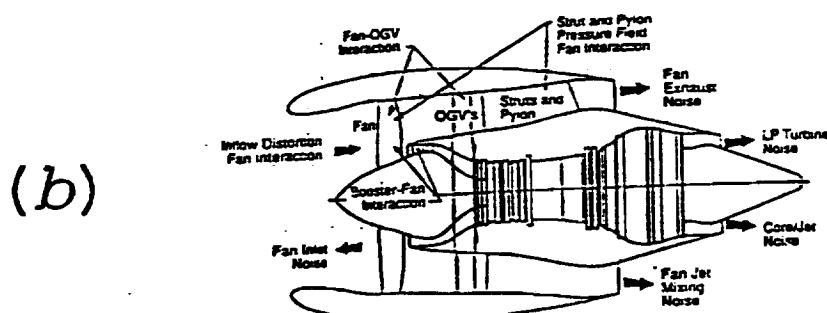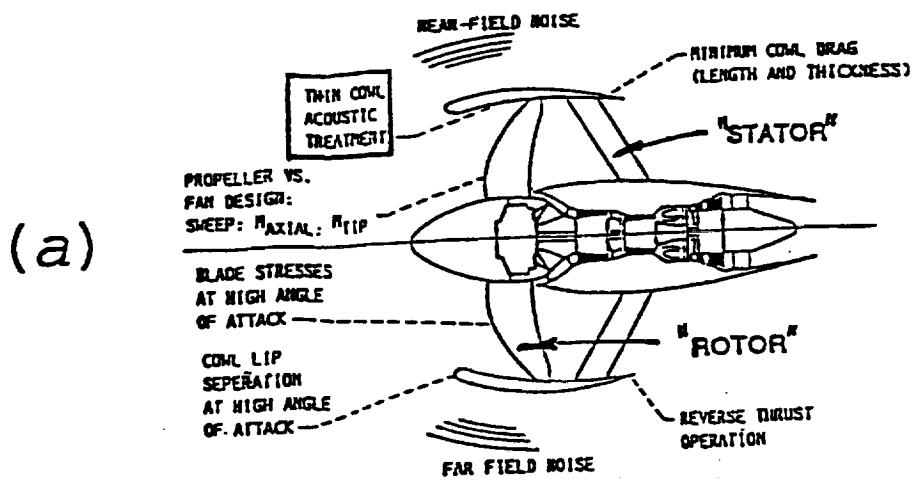
High bypass engine primary noise sources

(b)

(c)
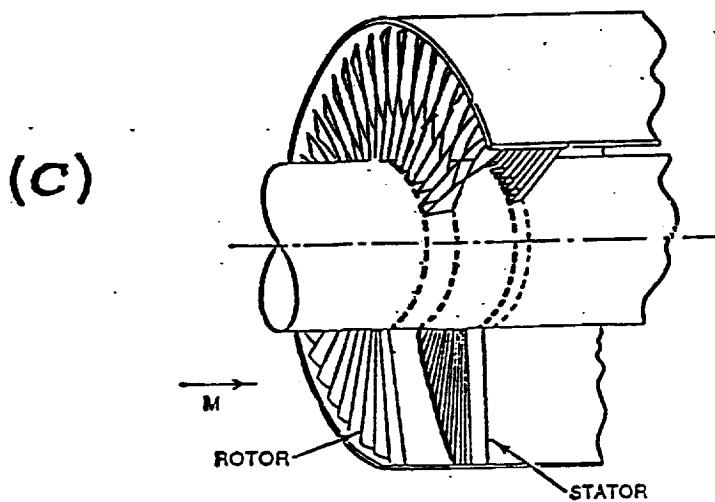
Figs. 1a-c - (a): From Dittmar[2a]: Advanced Ducted Propeller;
(b-c): From Fleeter[3] and Hanson[4], respectively: Advanced Ducted Propulsors

41
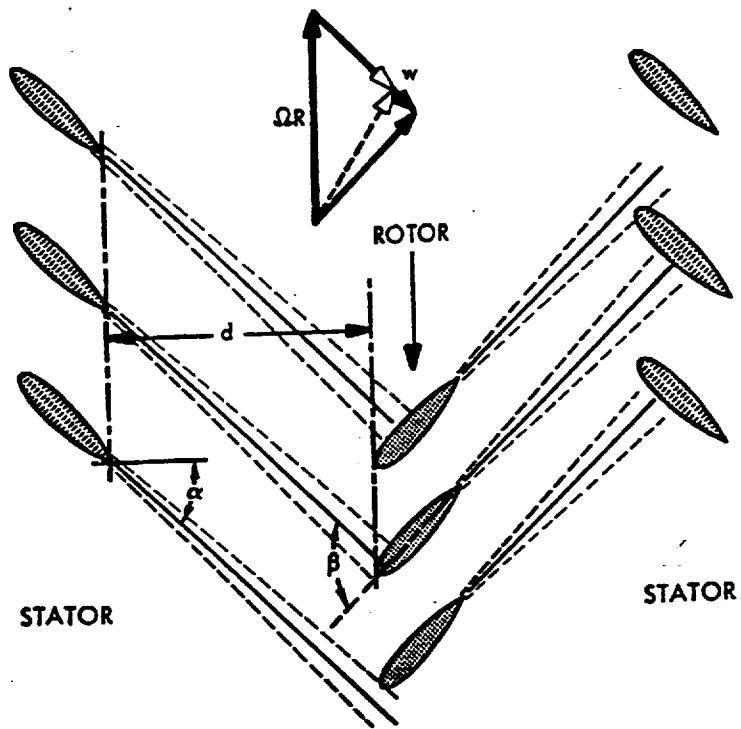
Fig. 2a - From Lowson[11]: Three-element stage showing stator/rotor and rotor/stator
interactions.
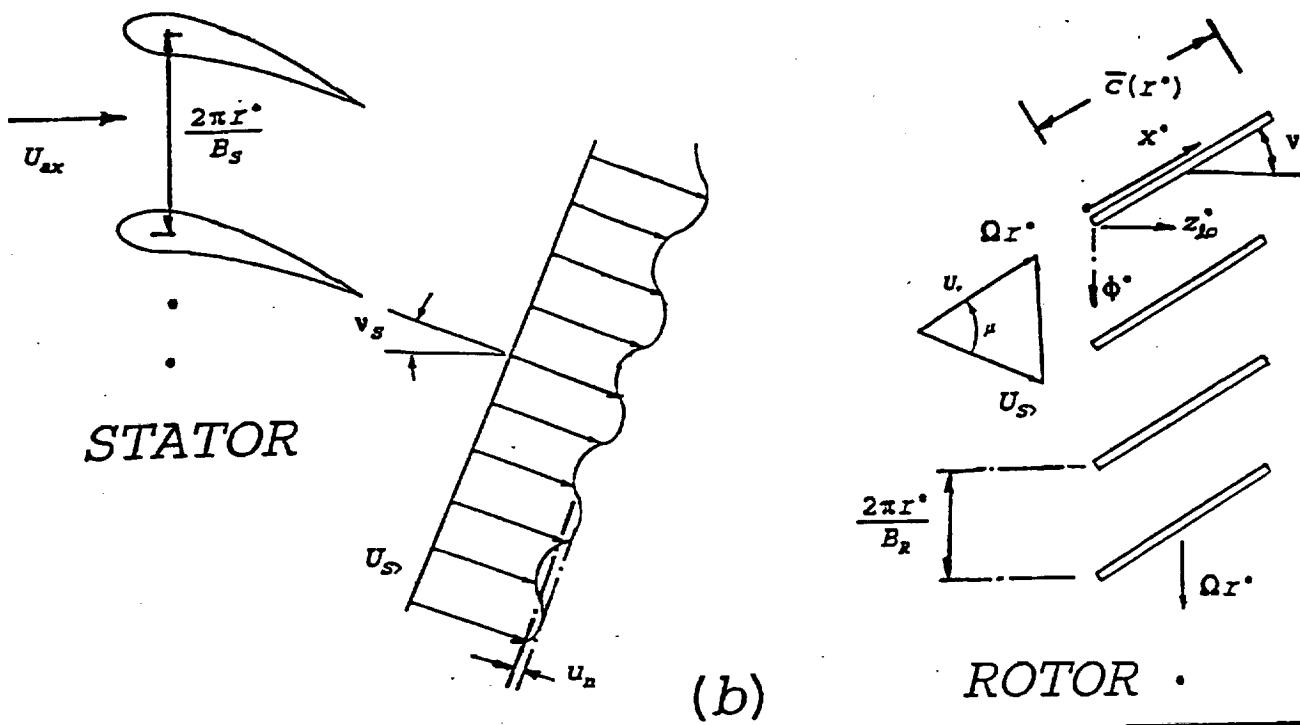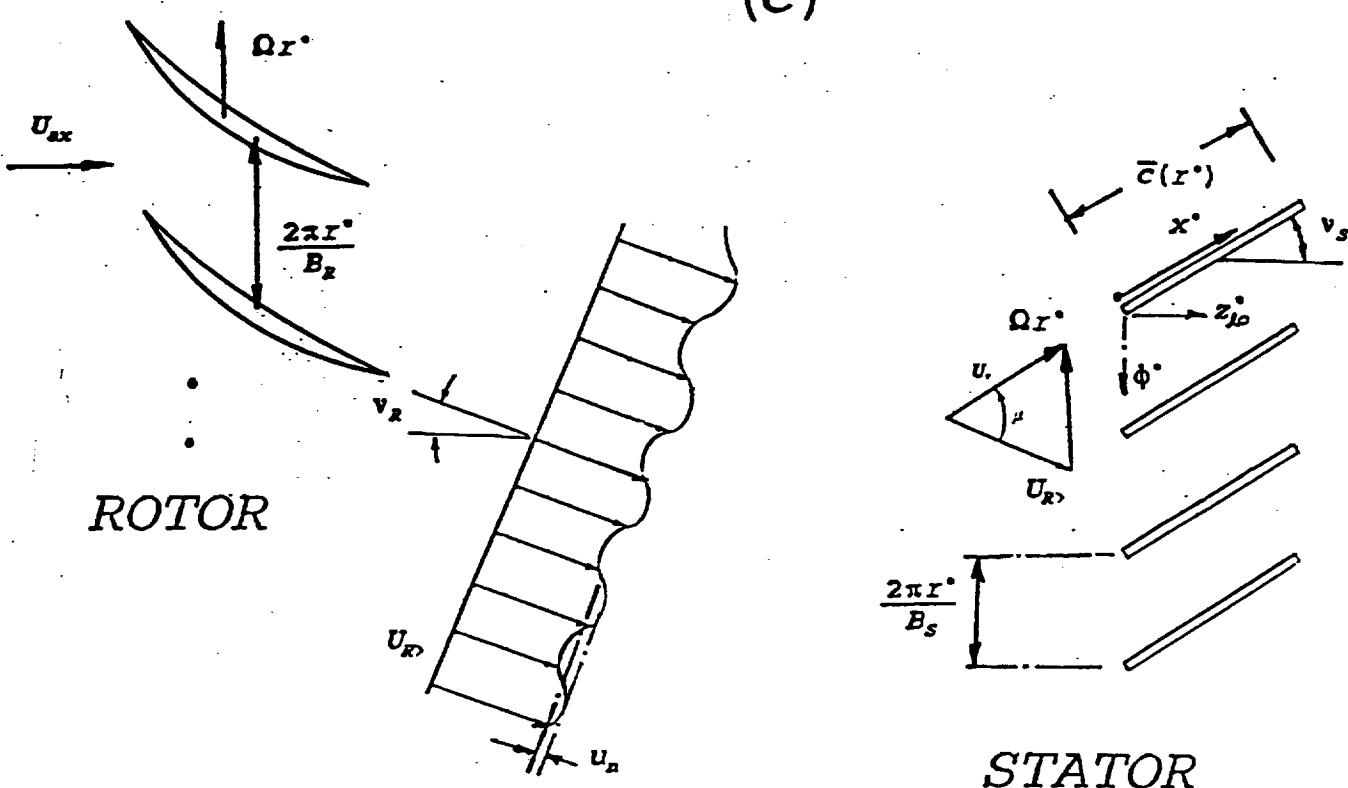
Figs. 2b,c - Adapted from Goldstein[12]: (b) Stator-first, rotor-second stage from the left half of Fig. 2a, but with that figure generalized to three dimensions. View at radial station r^*. B_S stator blades now generate a tilted wake of mean flow $U_{S>}(r^*)$ and a nonuniform perturbation field with circumferential harmonics $u_{nB_S}(r^*)$. The rotor blades see a relative freestream $U_r(r^*)$ at zero angle of attack. Their x^* leading-edge coordinate comes into play in the noncompact version of the airloads theory. (c) Rotor-first, stator-second arrangement typical of the fan stage of most modern commercial aircraft engines.

43

$$\frac{2\pi r^*}{B_S}$$

U_{ax}

STATOR

U_{ax}

$c\,(1-M_{ax})$

x^*

v_R

ROTOR

Ωr^*

(d)
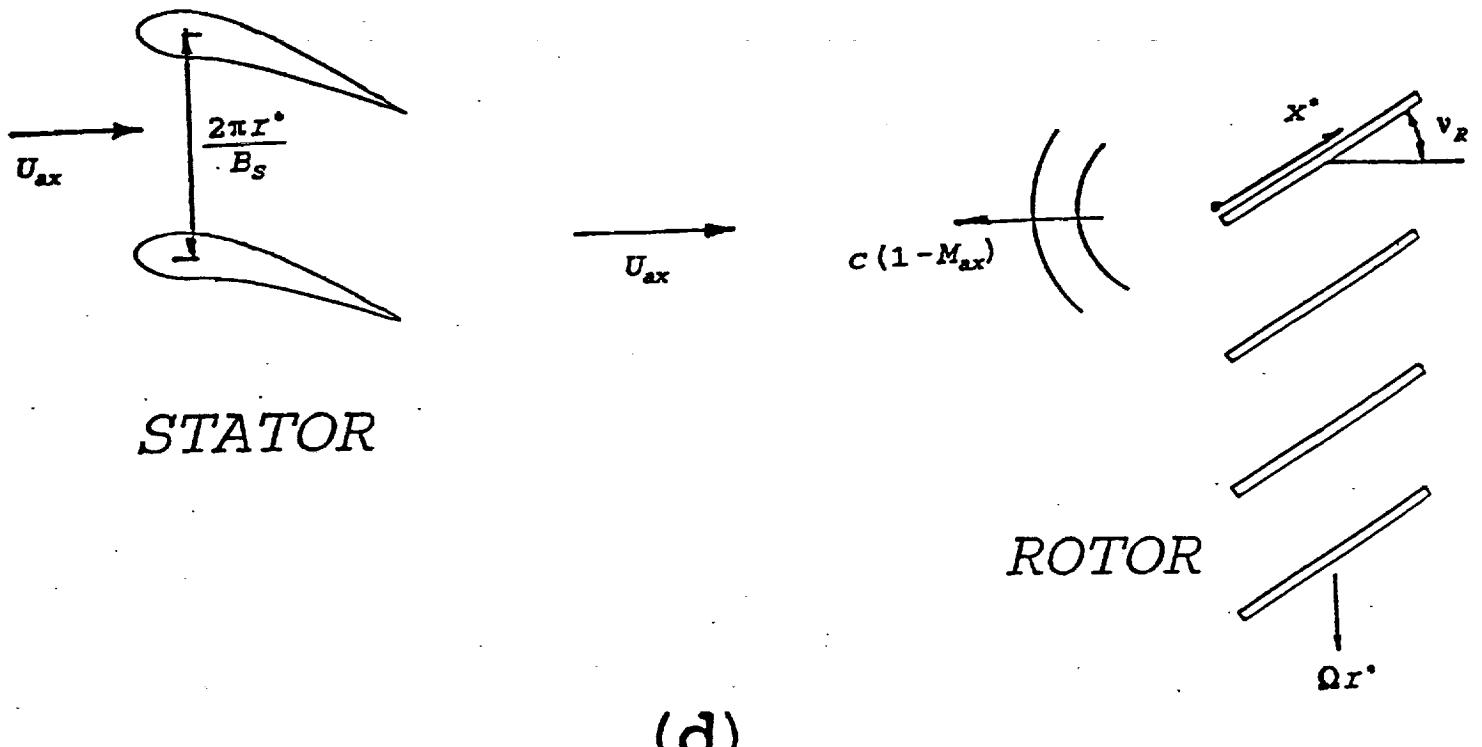
Fig. 2d - Once their strength has been calculated, the dipole sources on the rotor blades in Fig. 2b radiate in a medium with a globally uniform freestream; i.e., the propagation model removes the swirl component of $U_{S>}(r^*)$ in Fig. 2b.

$$\frac{2\pi r^*}{B_S}$$

$$u(r^*,\phi:\ 0<\phi<2\pi/B_S)$$

$$\phi$$
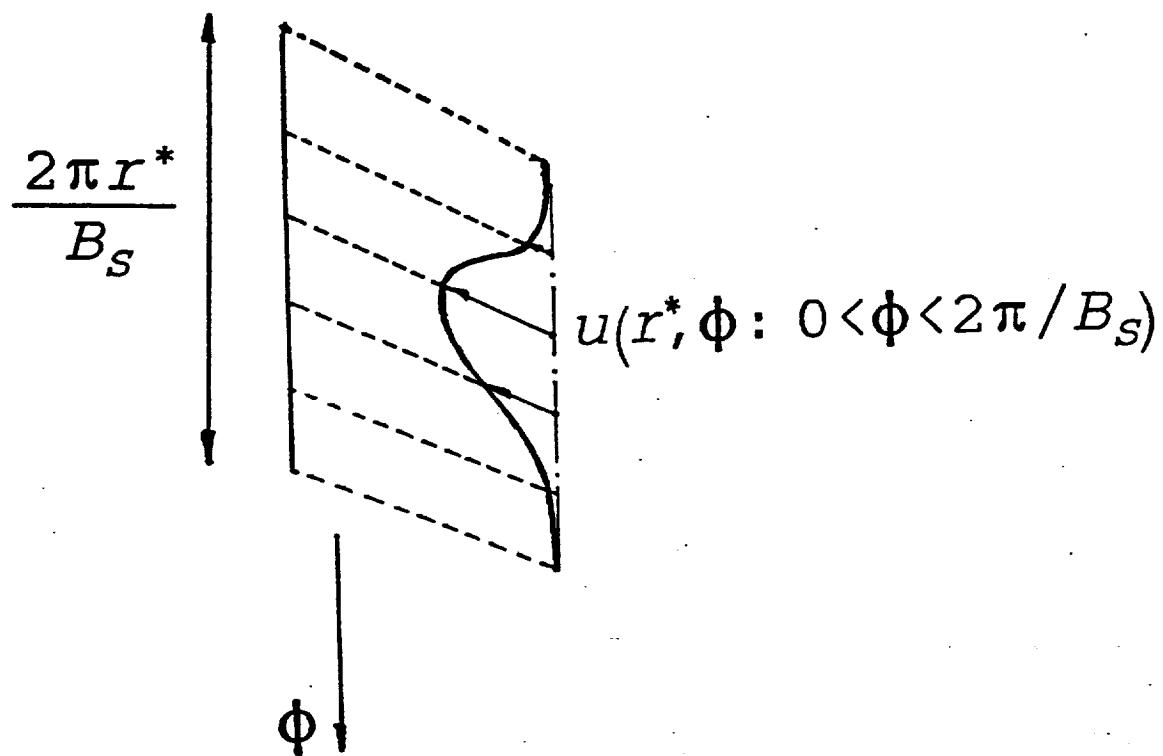
Fig. 3 - Modeled Gaussian form of the mean wake deficit u for a stator blade. Variable ϕ ranges from 0 to $2\pi/B_S$, and the distance indicated corresponds to the L/2-normalized form of the distance λ_o in Ref. 12's Fig. 3.18.

(a)

(b)
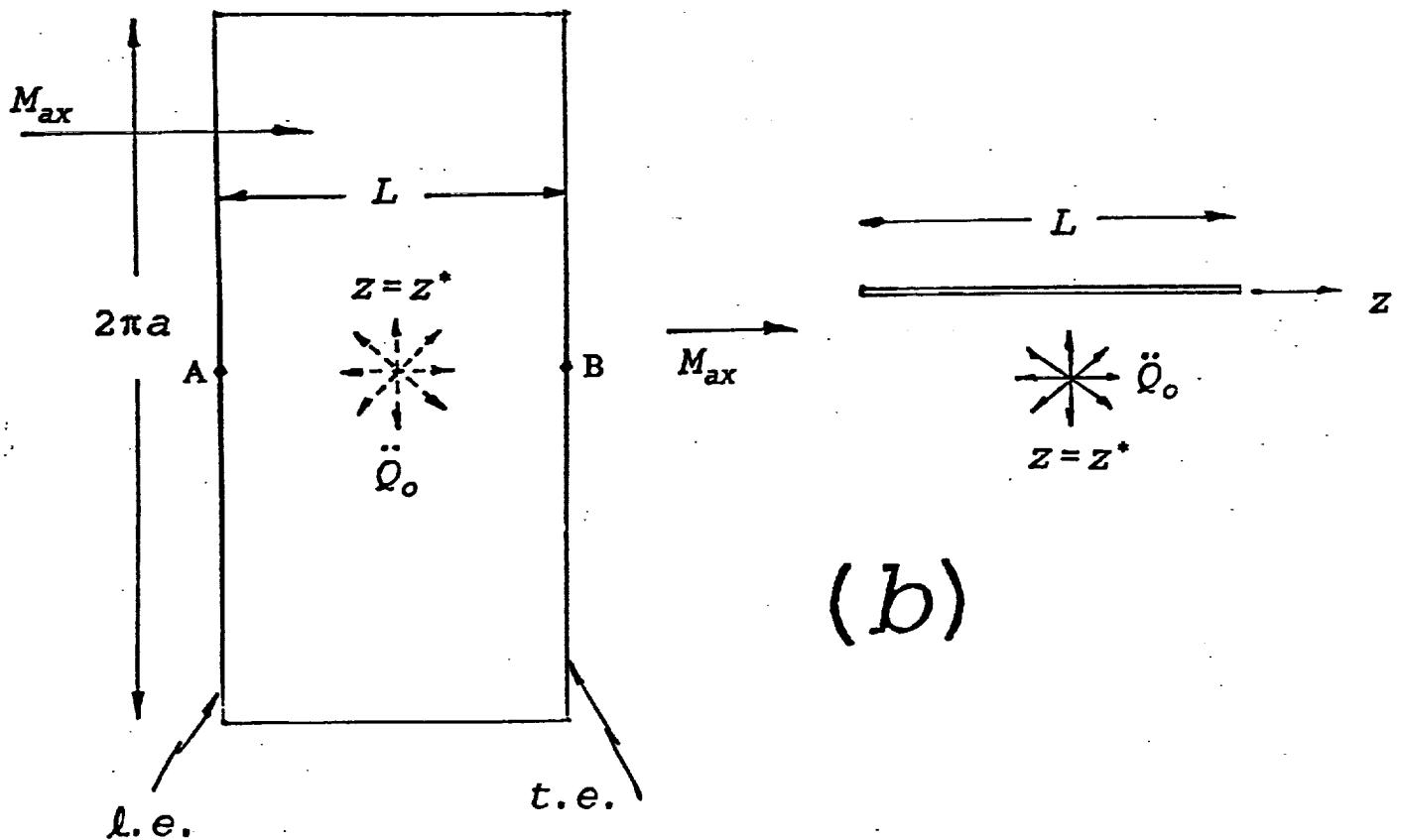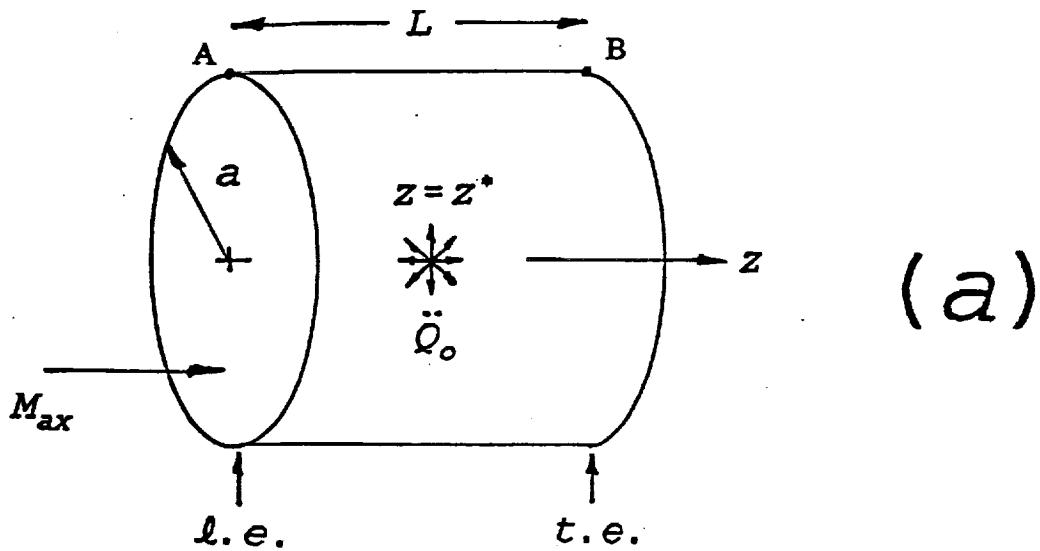
Figs. - 4a,b (a) Original and geometry of ring-wing chord L, insonified by a three dimensional volume velocity source of strength $\ddot{Q}_o$ at $z = z^*$ in Mach number flow M_{ax}. The diffracted field affecting a listener directly overhead of the cowl is determined primarily by the points A and B on the inlet and outlet, respectively.

(b) (left) unwrapped duct to provide the locally flat, two-edge model invoked in later figures, indicating the positions of points A and B. The implied observer is on a plane normal to the flattened "ring wing". The intersection of that plane and the wing is the chord line containing the points A, $z = z^*$, and B; (b)'s right-hand sketch shows the wing's chordwise view.
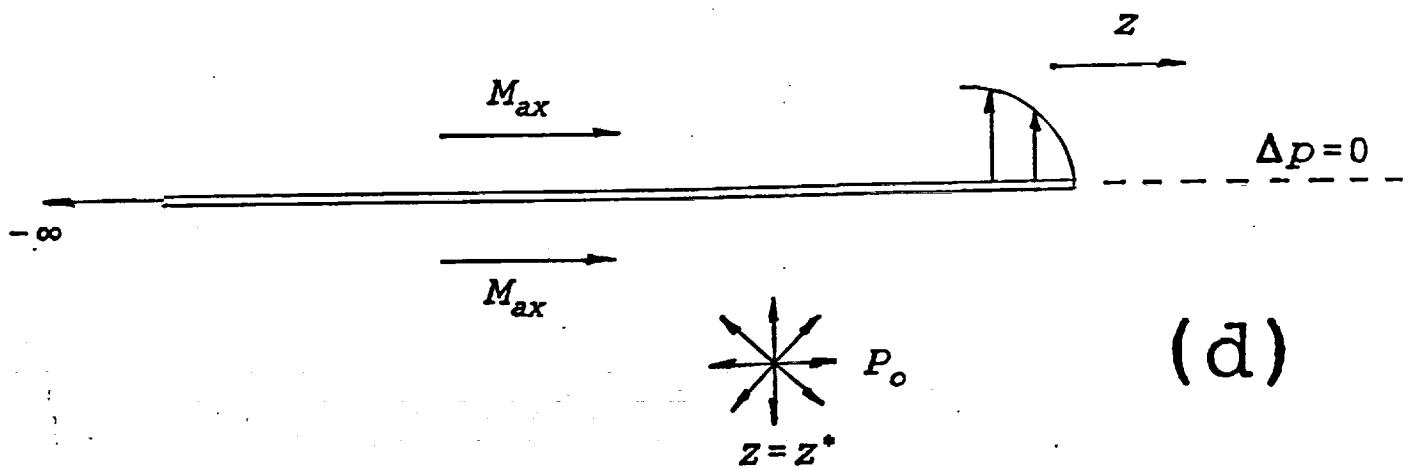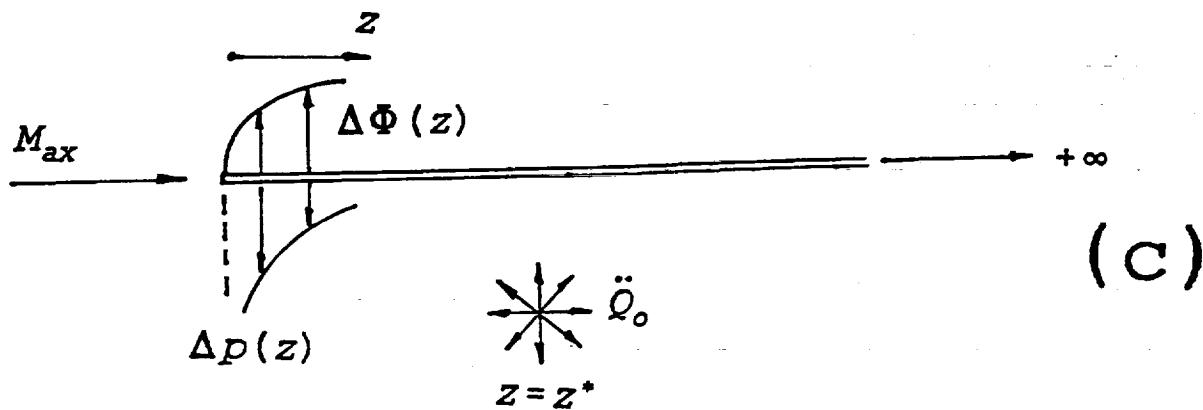
Figs. - 4c,d (c) Behavior of the diffraction load Δp and the jump in potential $\Delta \Phi$ on approach of the leading-edge of a semi-infinite rigid wing. (d) Candel and Amiet's trailing-edge diffraction problem for a pressure source of strength $"P_o"$. Δp vanishes on approach of the trailing edge as the square root of the distance to it, i.e., as the leading-edge behavior of the potential jump $\Delta \Phi$ in the upper figure.

47
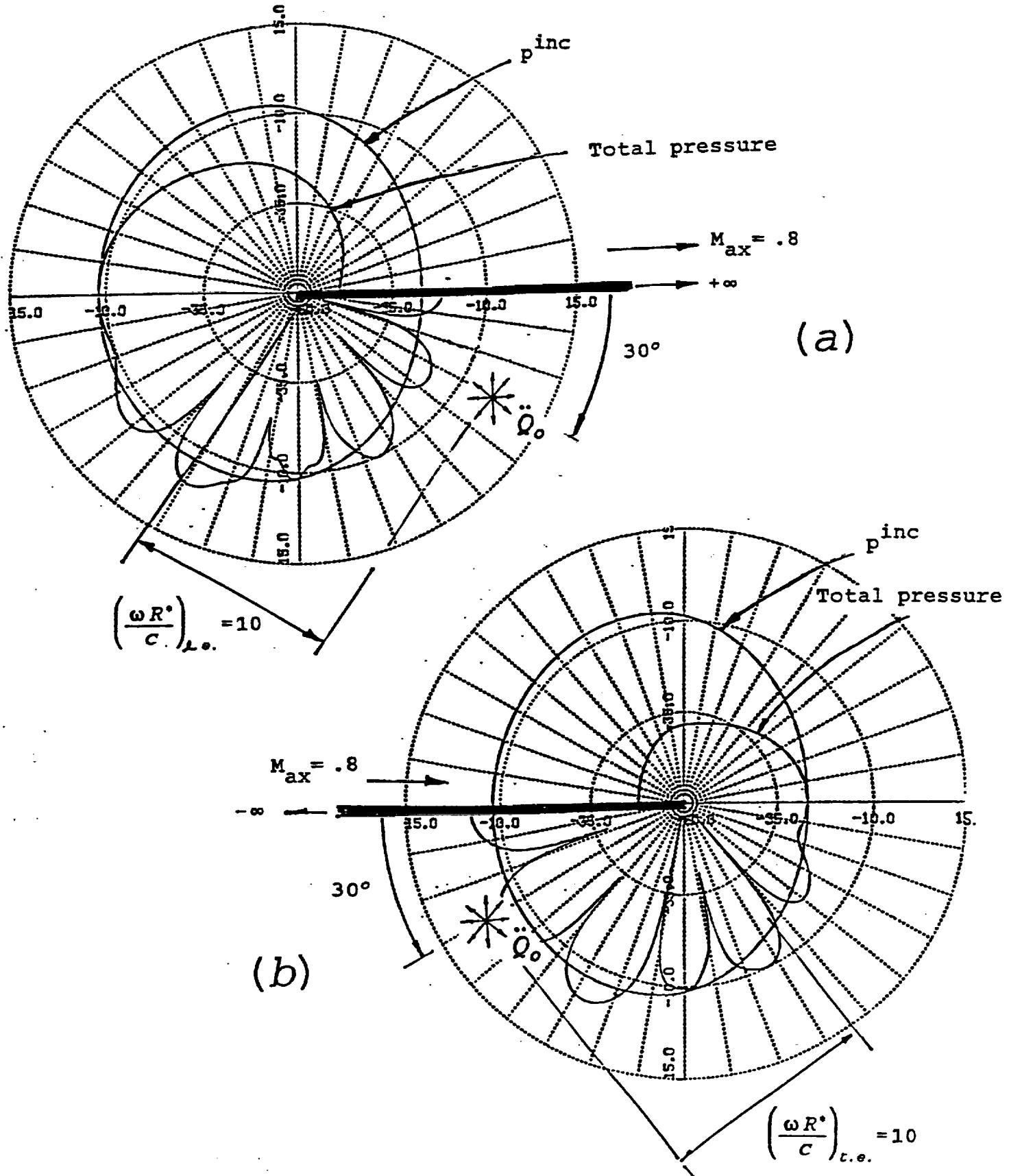
Figs. 5a,b - (a) Diffraction by a leading-edge wing; (b) by a trailing-edge wing.

p^{inc}

total pressure

$M_{ax} = .8$

$l.e.$ $30°$ $t.e.$

$\ddot{Q}_o$

$\left(\dfrac{\omega R^*}{c}\right)_{l.e.} = 10$

$\left(\dfrac{\omega R^*}{c}\right)_{t.e.} = 10$

L

$30°$

$\ddot{Q}_o$

M_{ax}

$l.e.$ $t.e.$
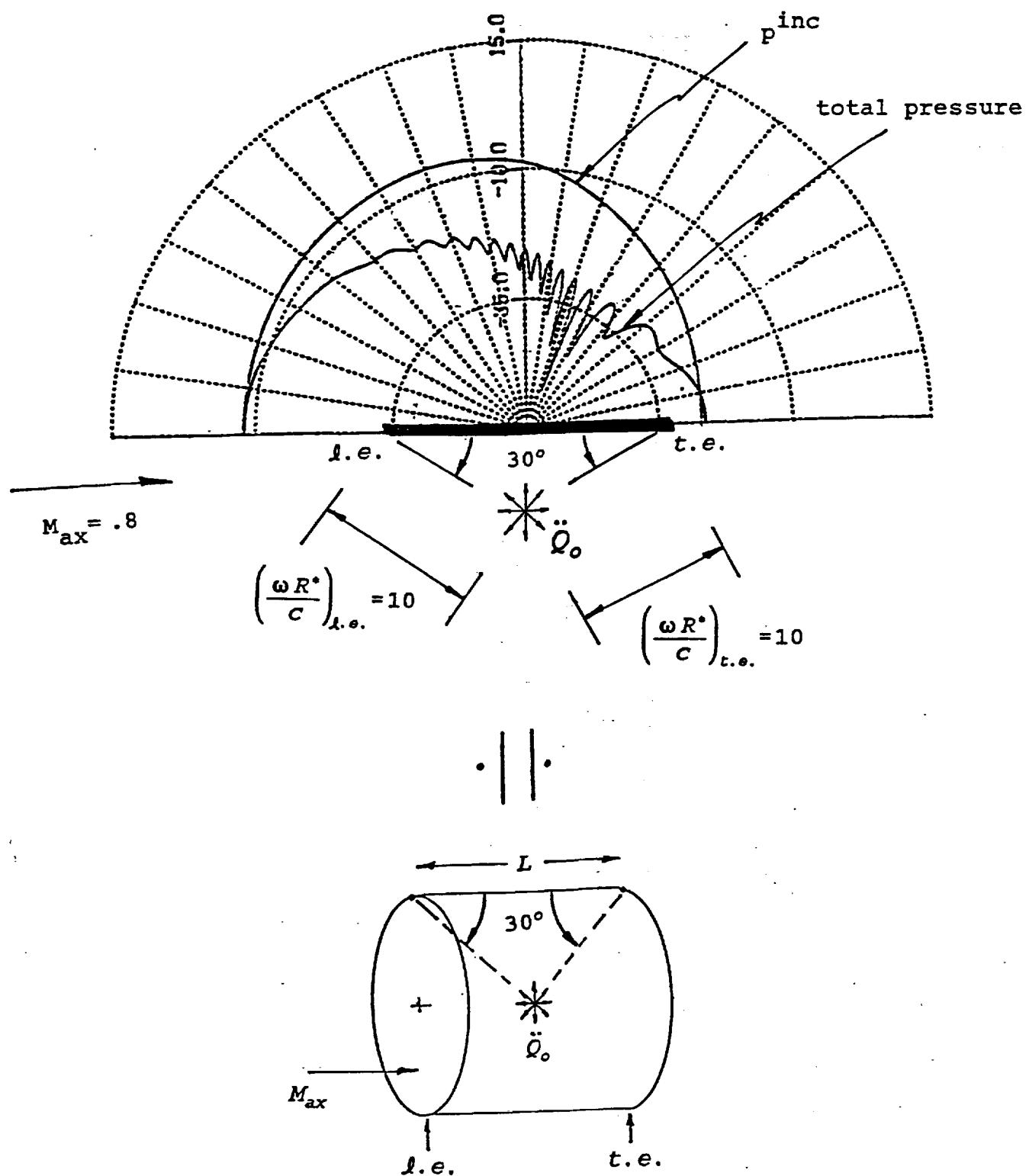
Fig. - 6 Coherent combination of the shadow zone fields of Figs. 5a,b, leading to a new fringe in that shadow region. The bottom sketch re-wraps the cowl to recall the relative position of source and edges in the original geometry.
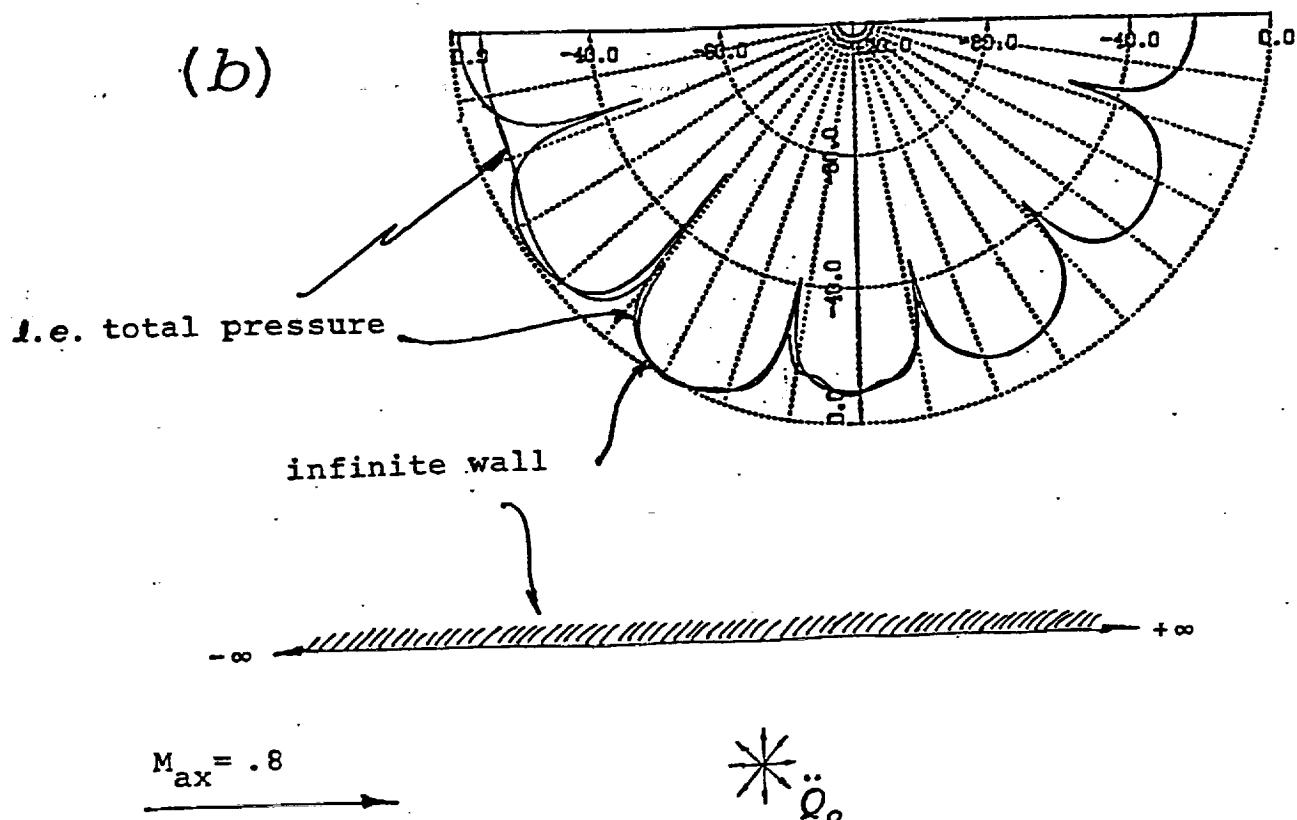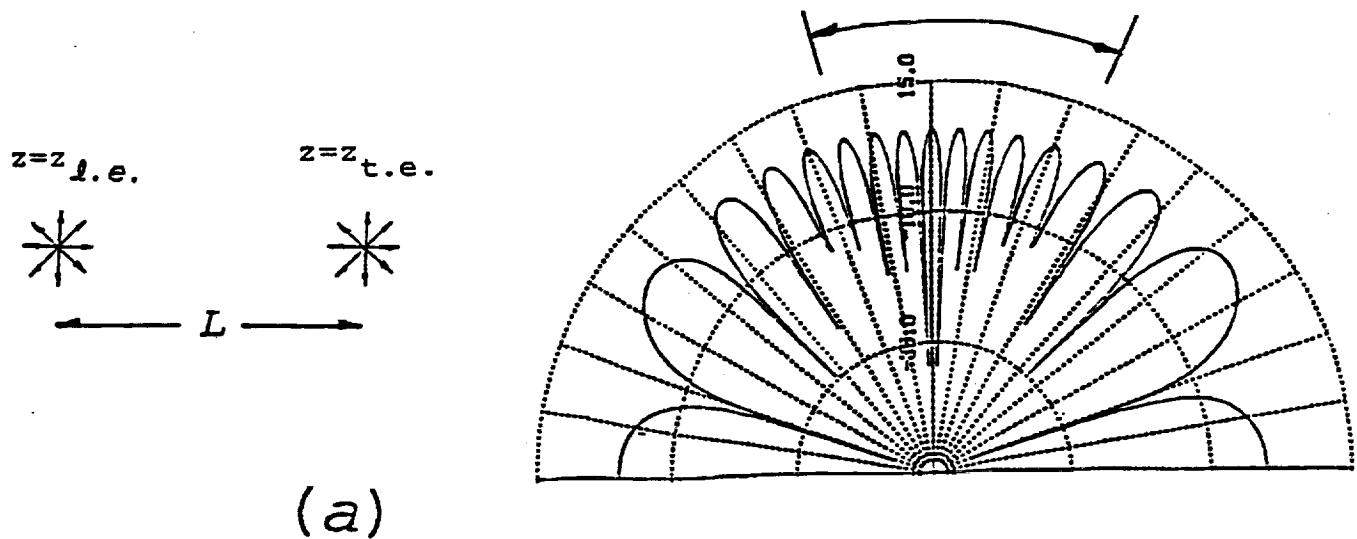
Figs. - 7a,b Sub-canonical calculations to verify Figs. 6's directivity pattern: (a) lobe field in the
rough sector indicated, from the phase factors of two "diffraction" sources a distance
L apart in a freestream M_{∞}; (b) The lobe pattern on the illuminated side of the
leading-edge solution in Fig. 5a, compared to that of a source near an infinite rigid
wall. The two patterns match towards the right side of the picture as they should.

p^{inc}

total pressure

15.0

10.0

-35.0

$+\infty$

30°

$-\infty$

30°

$\ddot{Q}_o$

$M_{ax}= .8$

$\left(\dfrac{\omega R^*}{C}\right)_{\ell.e.}=10$

$\left(\dfrac{\omega R^*}{C}\right)_{t.e.}=3.34$

M_{ax}

30°

30°

$\ddot{Q}_o$
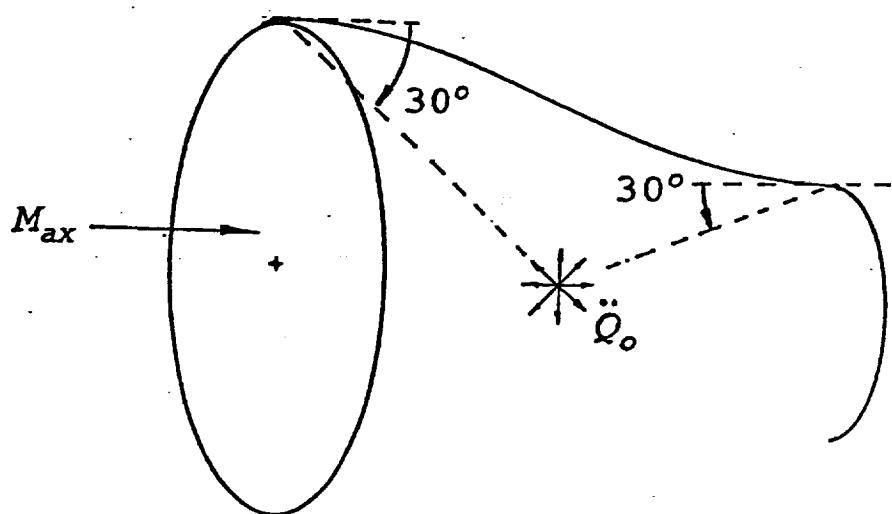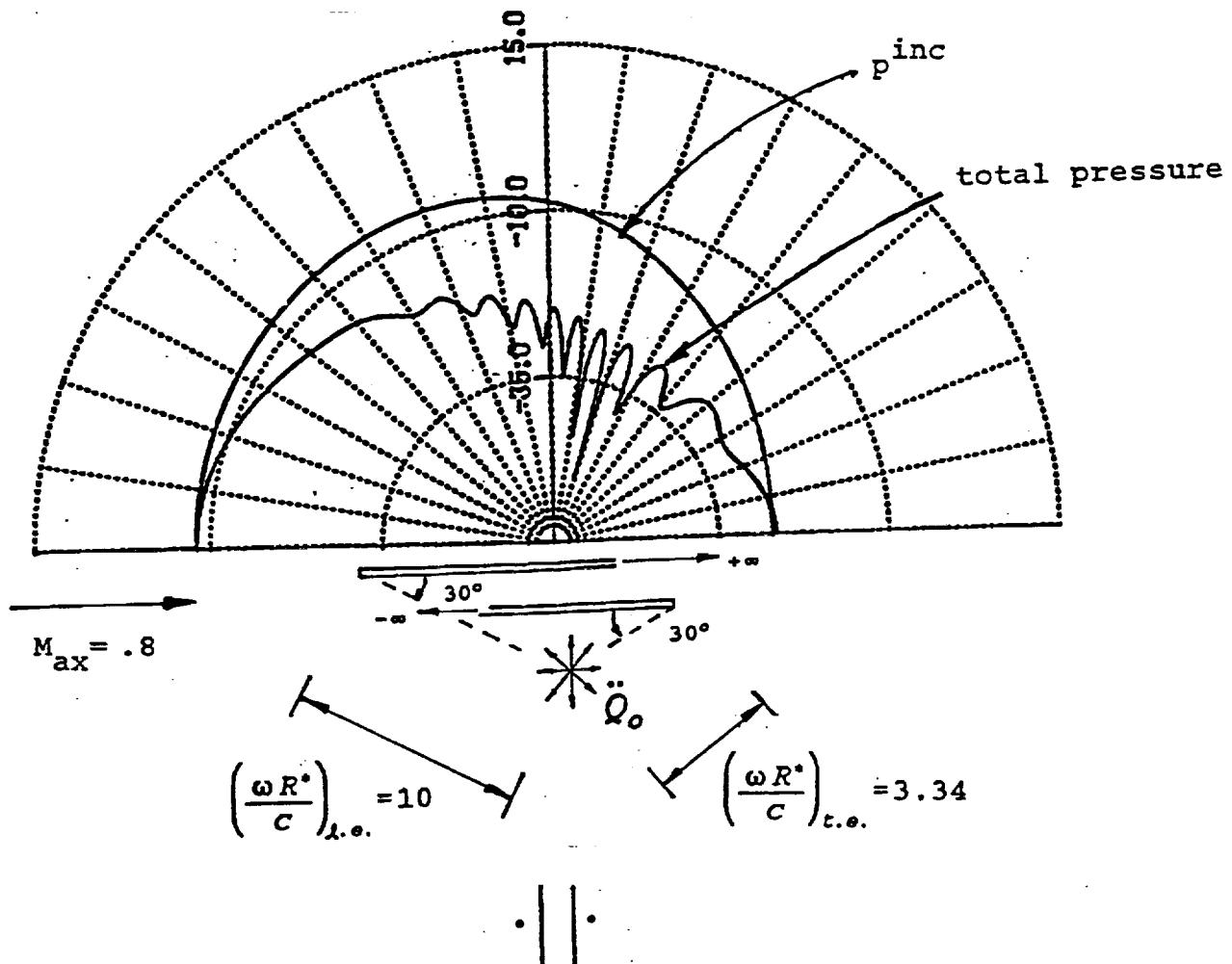
Fig. 8 - Offset leading- and trailing-edge screens as a model of the cowl shape shown in the lower sketch. The cowl's generator has zero slope at both the inlet and outlet.

51
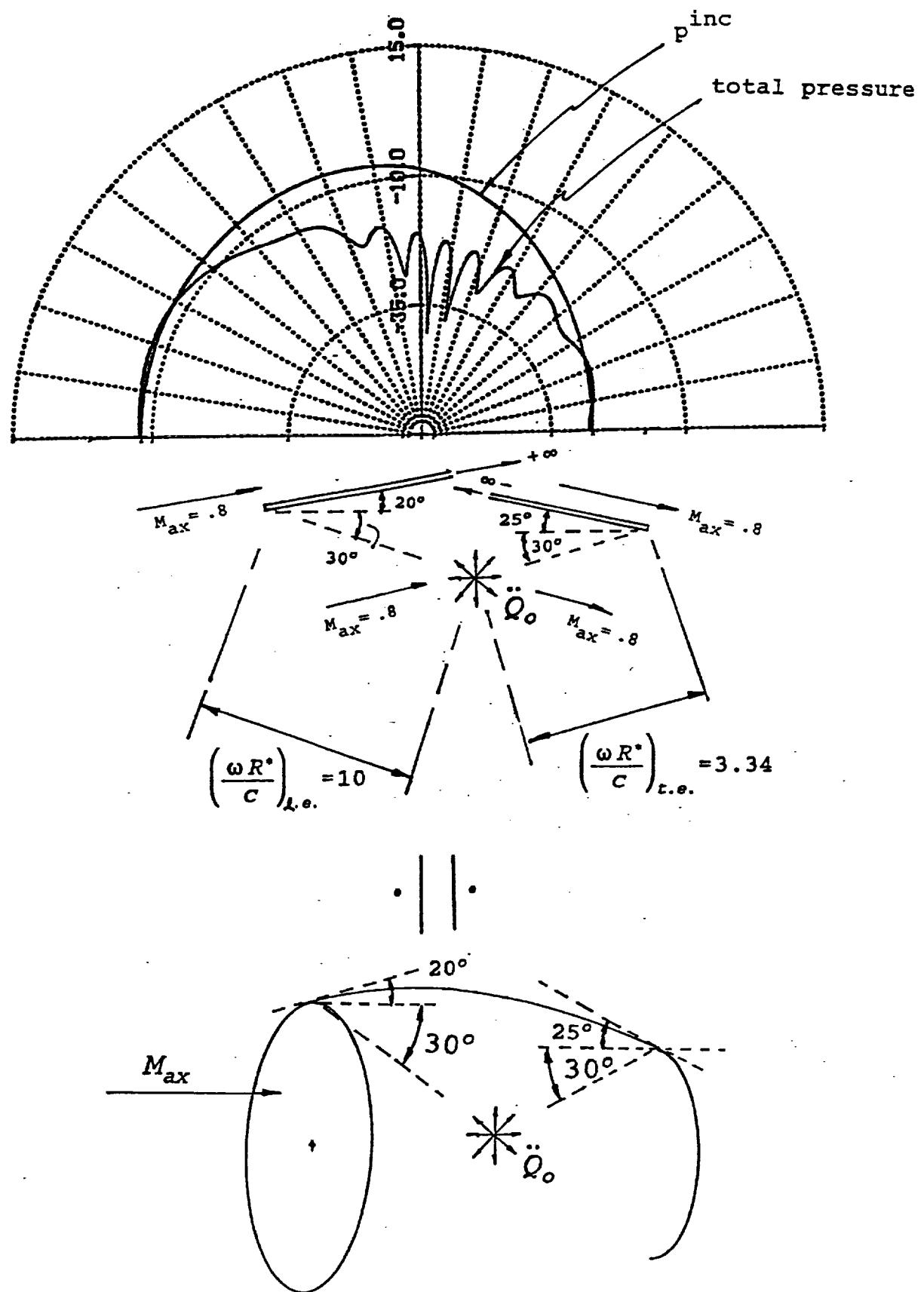
Fig. 9 - Conceptual "stretching" of the model in Fig. 8 to account for nonzero leading- and trailing-edge camber. The two flattened screens are now tilted and so are the freestreams.
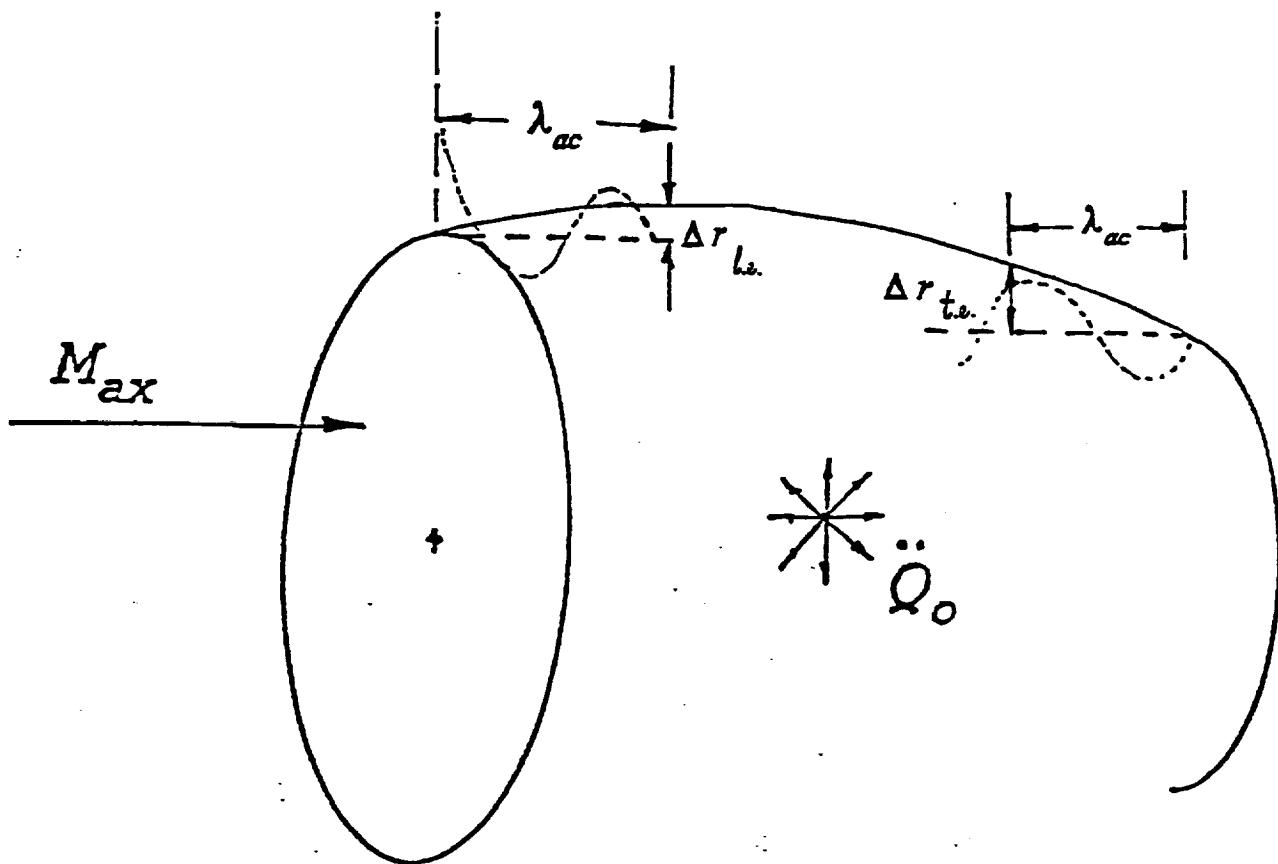
Fig. 10 Leading- and trailing-edge regions of potentially significant "steering" by the cowl's diffraction dipoles, along the on-axis radiation directions. The actual steering for each edge should be minimal when the local value of $k_{ac}\Delta r$ is $\ll 1$. The sketch shows an example where the acoustic wavelength $\lambda_{ac}=2\pi/k_{ac}$ is in fact much greater than Δr for both edges, so that the hoped-for steering becomes negligible (as confirmed by the canonical calculations).
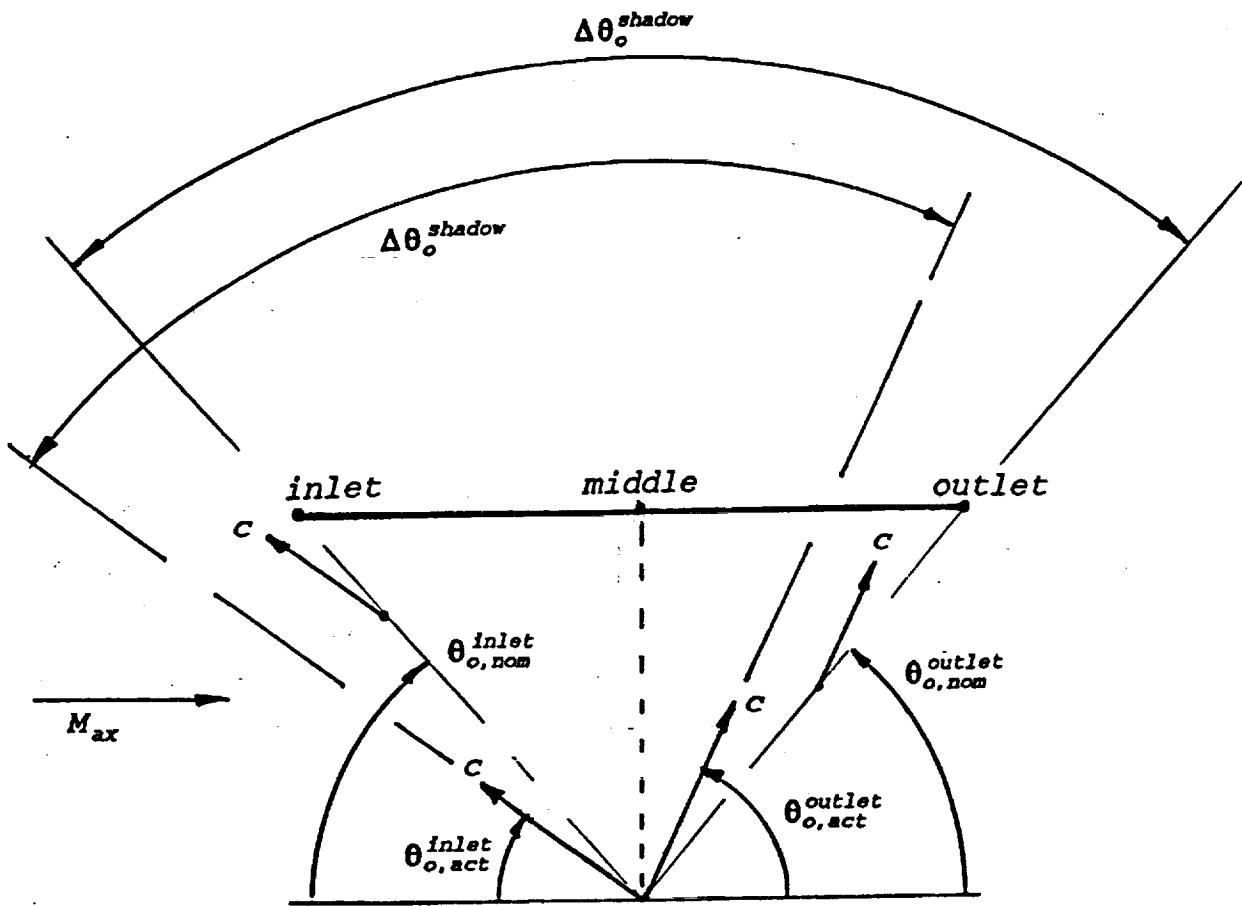
$$\sin\theta_{o,act}^{inlet} = \frac{-M_{ax}\cot\theta_{o,nom}^{inlet} + \sqrt{\beta_{ax}^2 + \cot^2\theta_{o,nom}^{inlet}}}{1 + \cot^2\theta_{o,nom}^{inlet}}$$

$$\sin\theta_{o,act}^{outlet} = \frac{M_{ax}\cot\theta_{o,nom}^{outlet} + \sqrt{\beta_{ax}^2 + \cot^2\theta_{o,nom}^{outlet}}}{1 + \cot^2\theta_{o,nom}^{outlet}}$$

Fig. 11a: Aberration of sound: necessary tilting of ray directions for achieving a spatial objective. The figure shows the cowl's inlet and outlet stations, and a typical point of radiation at the cowl's axial center but removed from it radially by an arbitrary amount. Rays shooting upstream must do so at an "actual" angle $\theta_{o,act}^{inlet}$ or less if they are to clear the cowl (upper equation). Downstream rays that make an angle $\theta_{o,act}^{outlet}$ or greater measured from the downstream axis strike the cowl.

cowl outlet

**directional ray content
of the specular zone**

**point origin
of radiation**
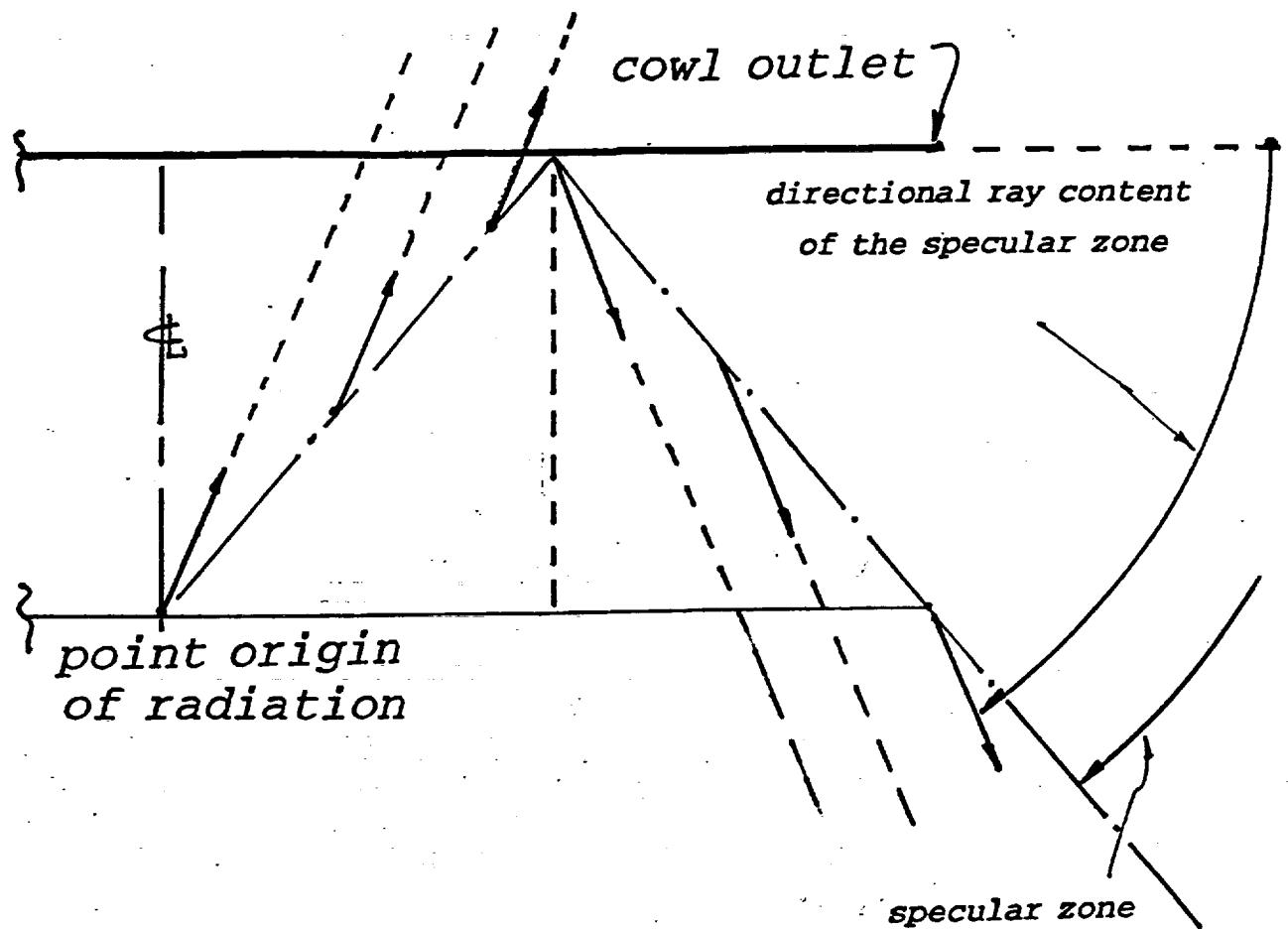
specular zone

Fig. 11b: Effect of ray tilting on the cowl's downstream zone of specular reflections (Snell's law in a flow). The picture shows a typical origin of radiation, and the "last" ray from that point to experience a single bounce against the cowl's inner wall before proceeding to the "lower" medium. The flow endows the downstream zone of specular reflections with a ray-directional content greater than that of a still medium.
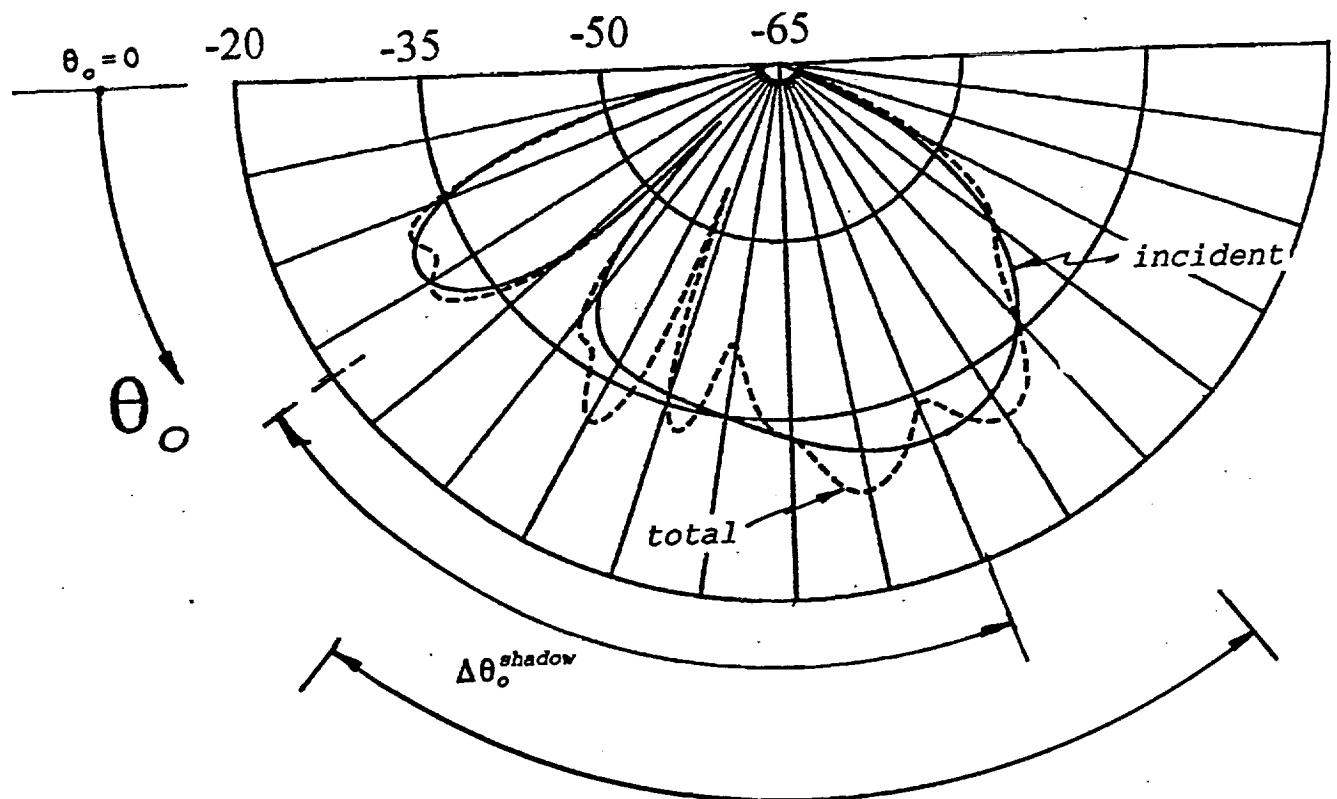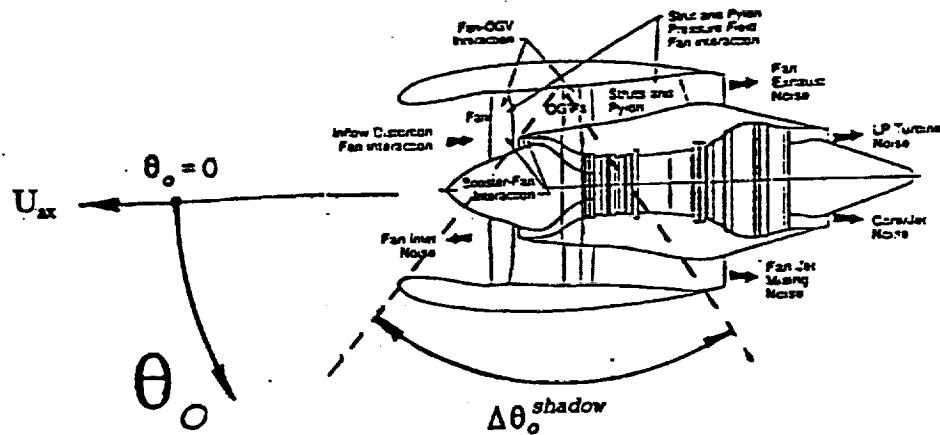
Fig. 12: Predicted directivity patterns on the ground's reference frame, for a stator-first/rotor-second artificial fan stage. The solid curve displays the incident field alone and the broken the total field (incident + cowl-scattered). The engine sketch shows the cowl's ideal shadow sector of geometric acoustics. The main figure shows the same sector shifted according to the ray content formulas on Fig. 11a. The radiating rotor blades are justifiably chordwise compact. The cowl is unlined.
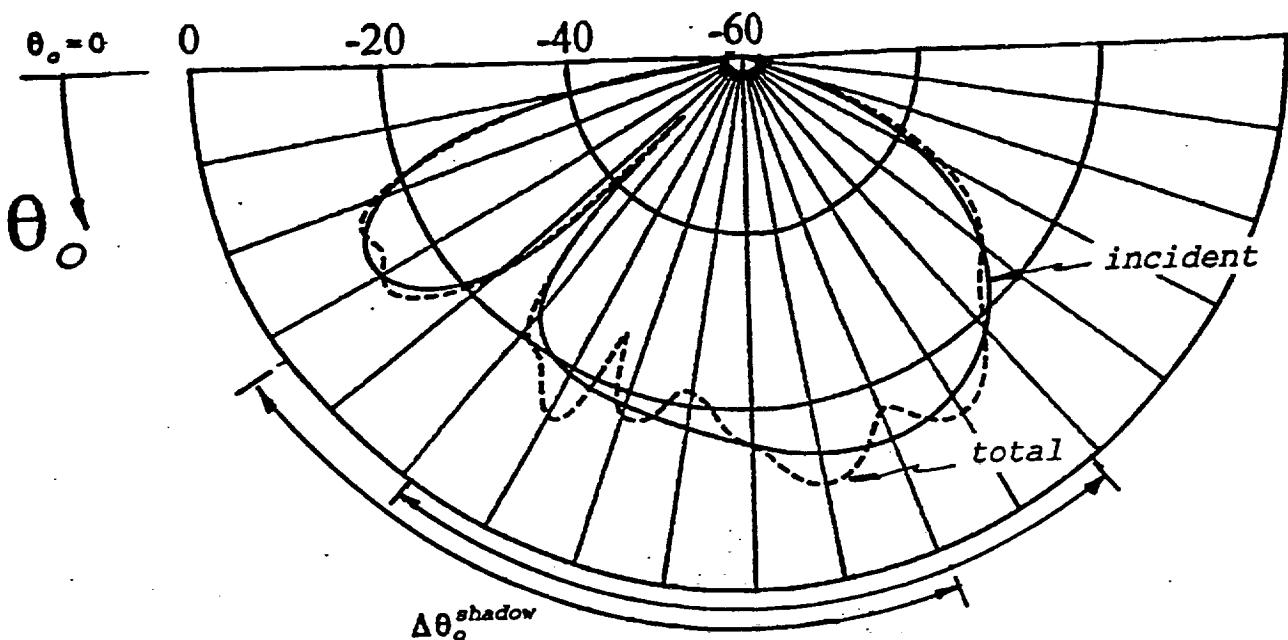
Fig. 13a: Incident and total fields for a practical rotor-first configuration: same as Fig. 12 but with the fan stage reversed. The cowl is unlined.
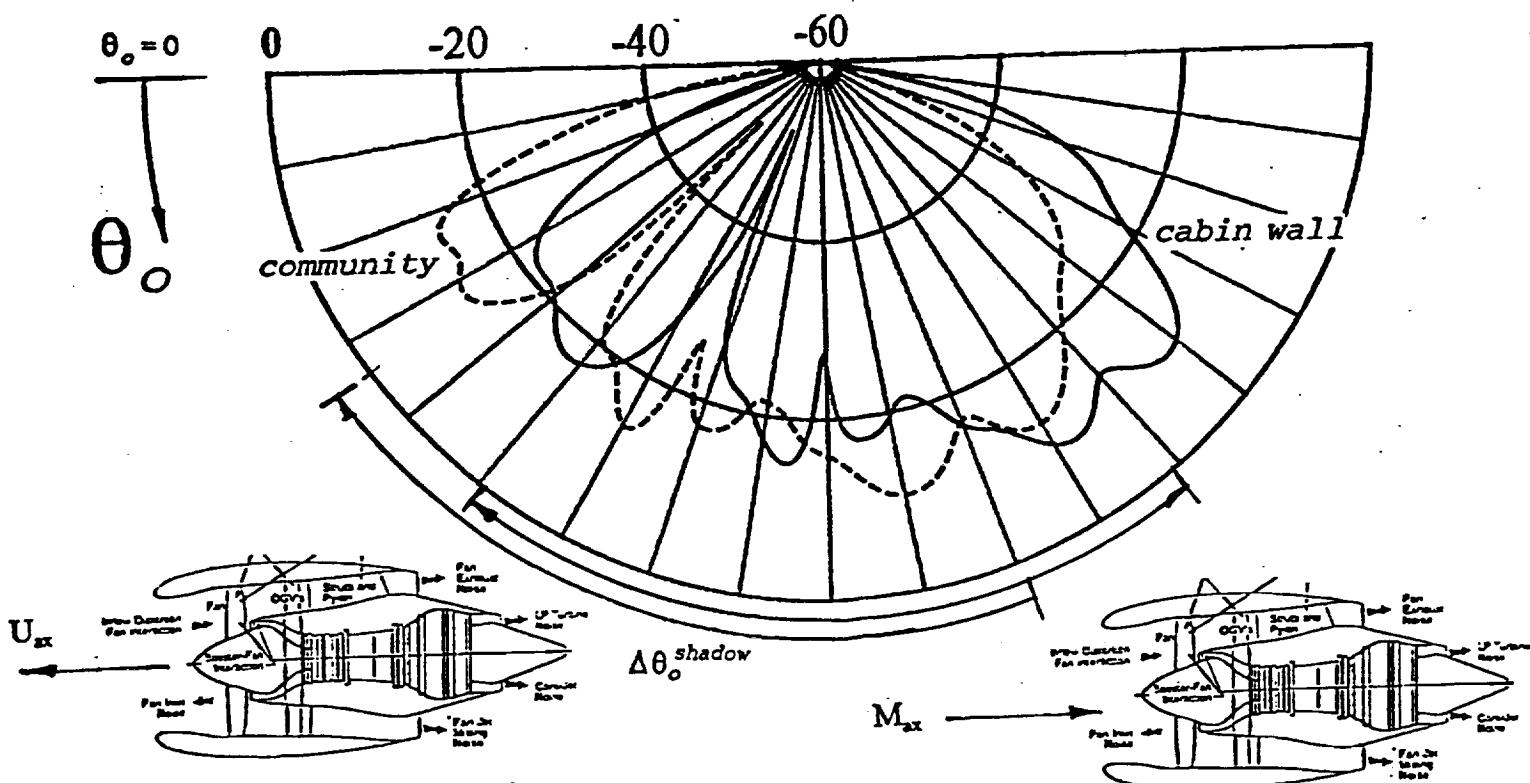
Fig. 13b: Total pressure fields as perceived on the aircraft's reference frame (solid), and on the ground (dashed). The former is washed downstream by the meanflow. The same sound field beams forward when heard at ground level by an observer stationary relative to the air. The flight Mach number is .4. The cowl is unlined.

57
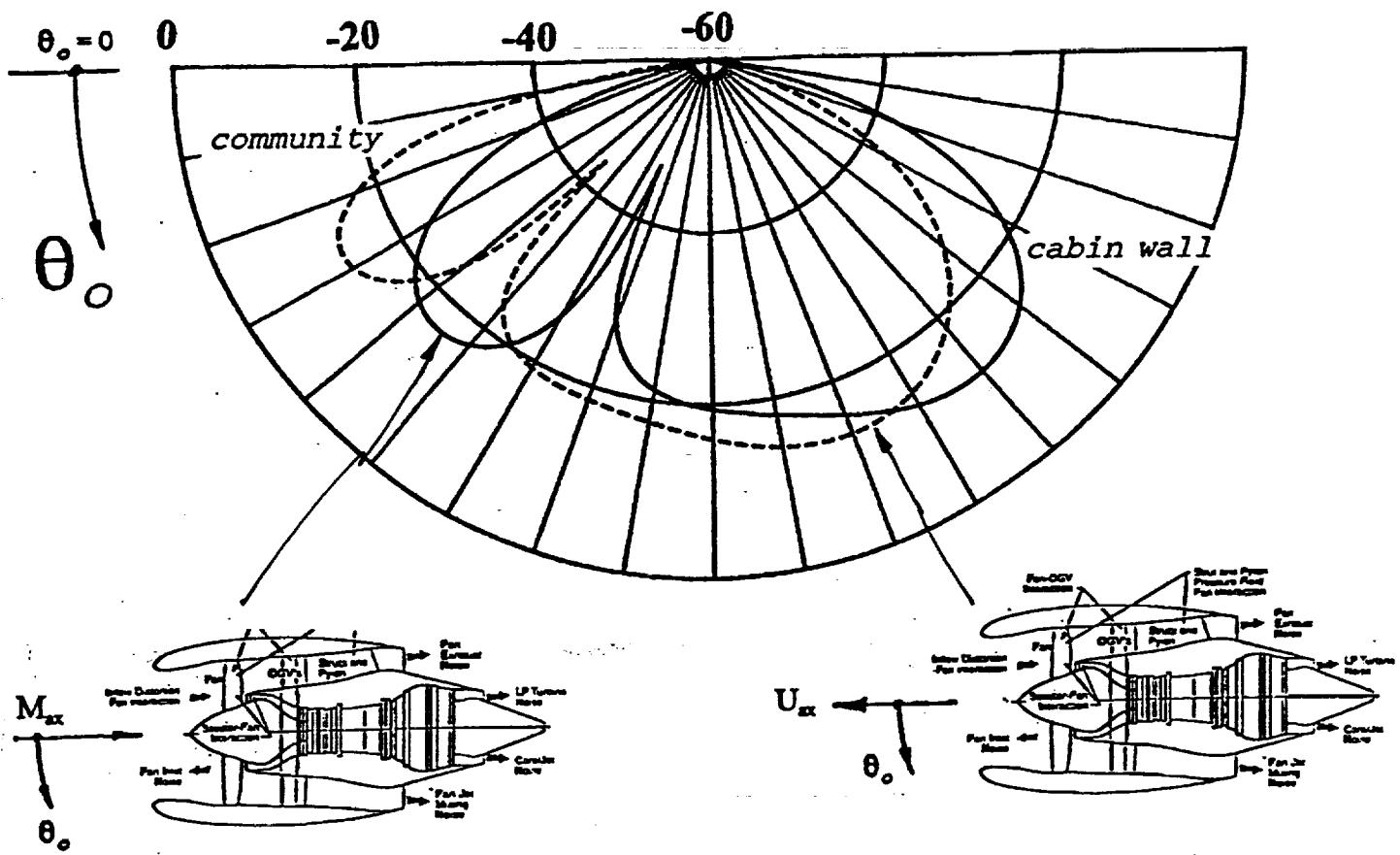
Fig. 13c: Comparison of the stator's incident fields for observers riding with the aircraft (solid), and at ground level (dashed).

θ_o = 0   0   -20   -40   -60

θ_O

specular looking

specular looking

*shadow producing (?)*

$\Delta\theta_o^{shadow}$
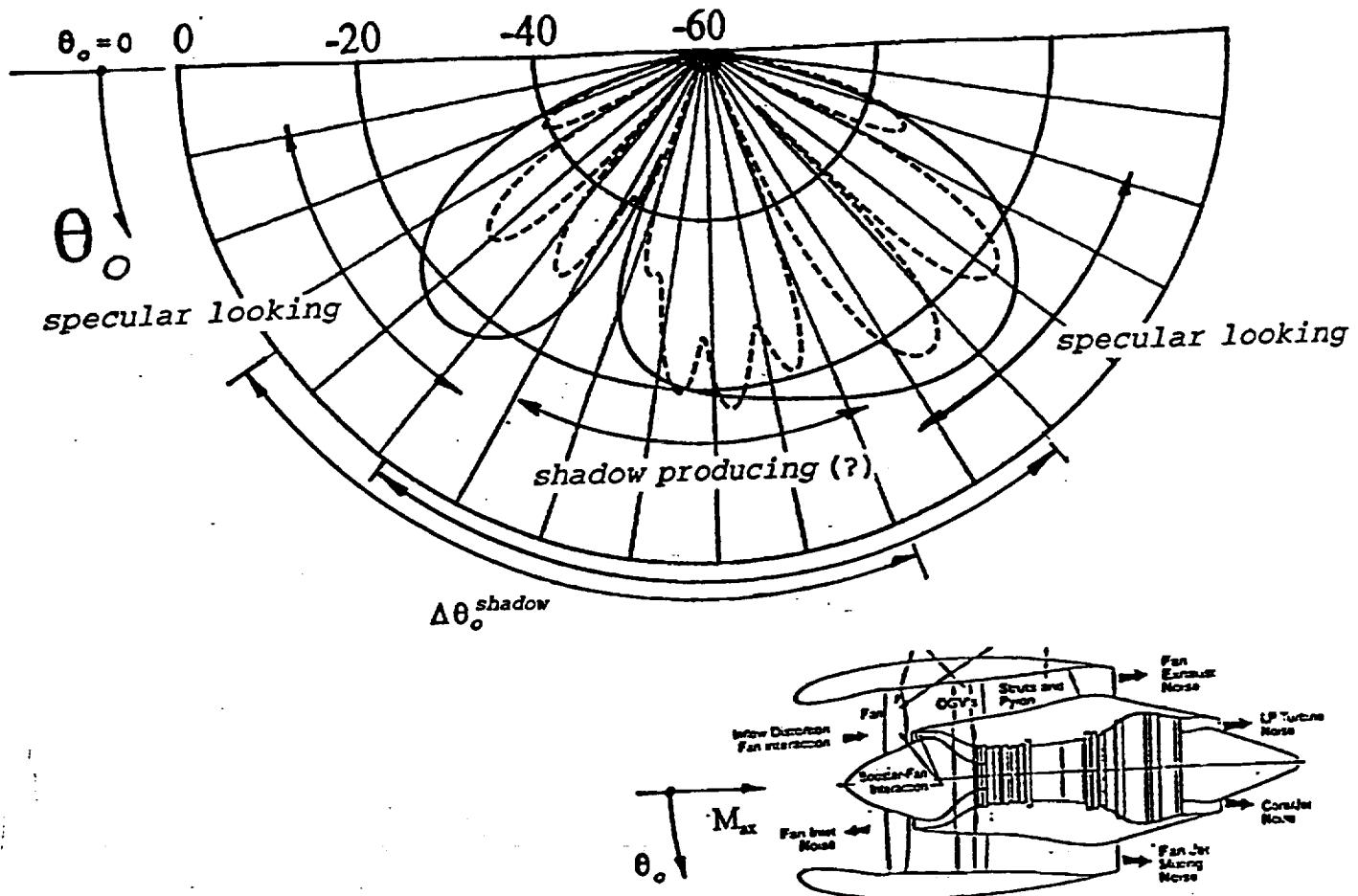
Fig. 13d: Diagnostic comparison of incident and cowl-scattered fields in the aircraft's reference frame. The specular and nonspecular lobes are interpreted as such. The cowl is unlined.

59
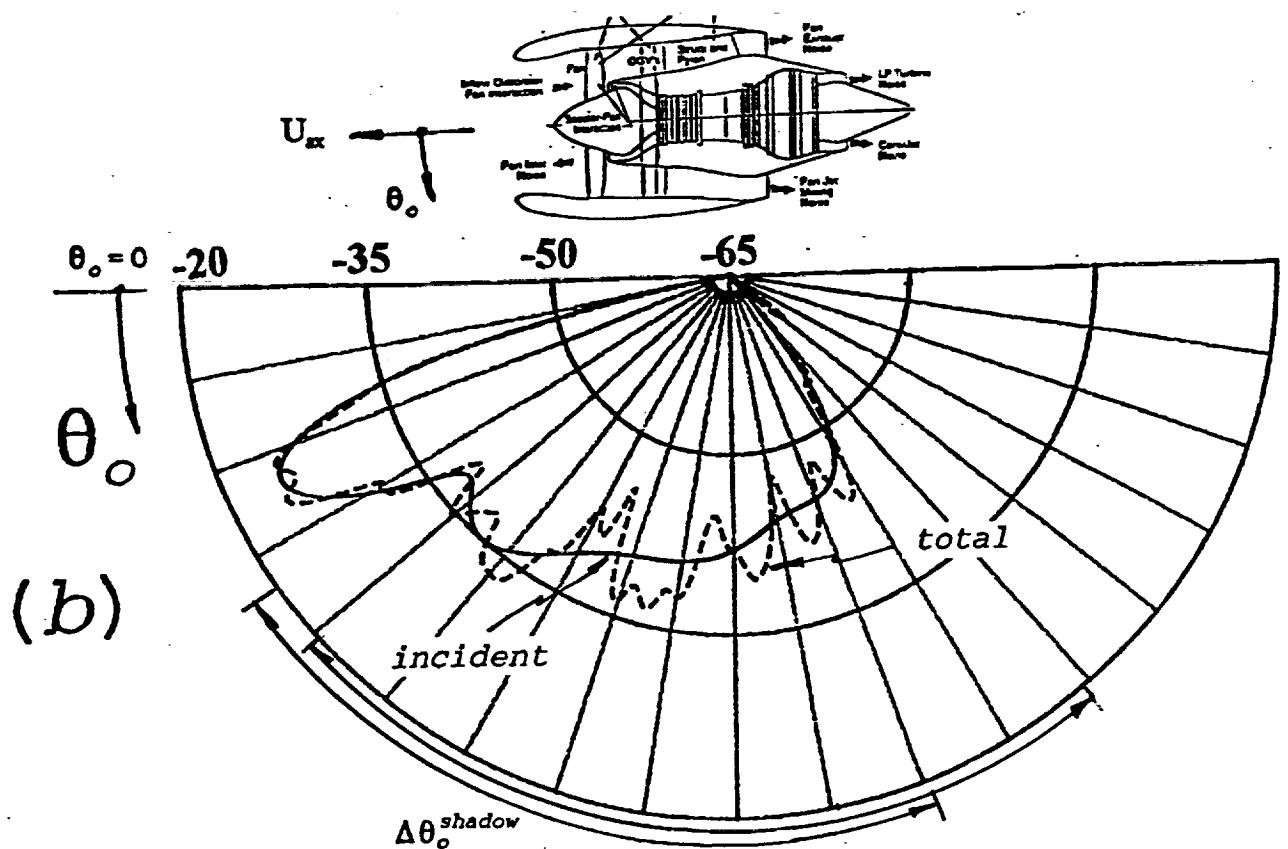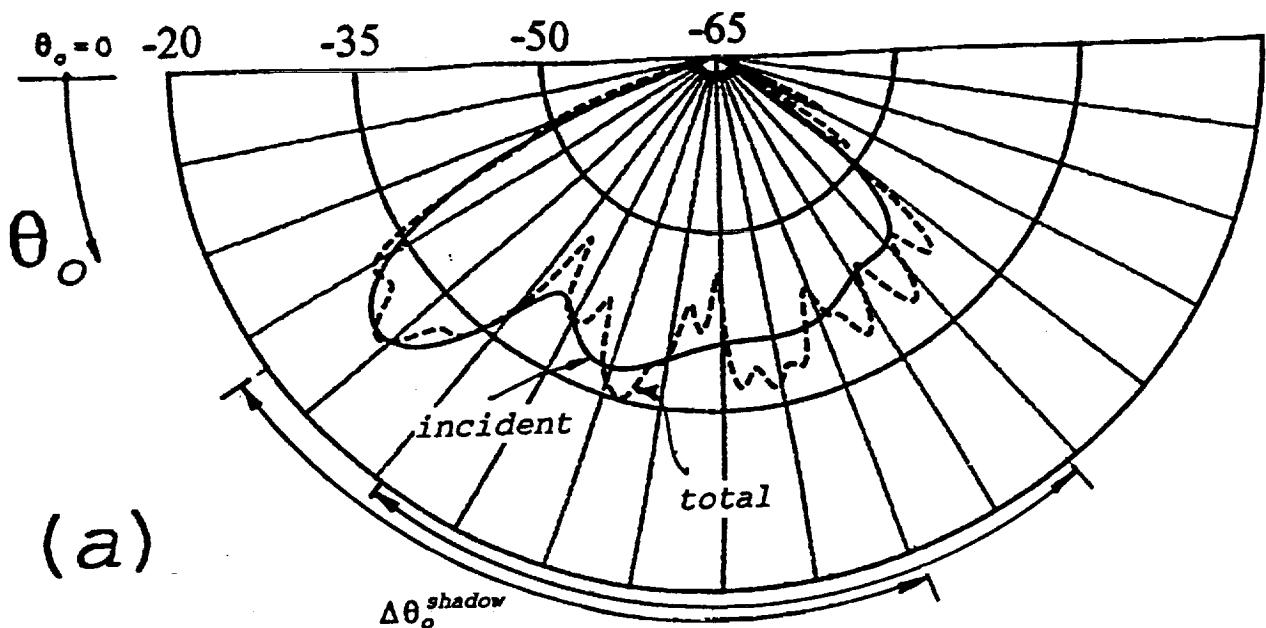
Figs. 14a,b: Predictions for the overtone m=2 of blade-passage. The twisted radiating stator blades are now chordwise noncompact at every radial station from root to tip. (a) shows incident and total fields in the aircraft's frame of reference; and (b) shows them as perceived on the ground. The cowl is unlined.

60
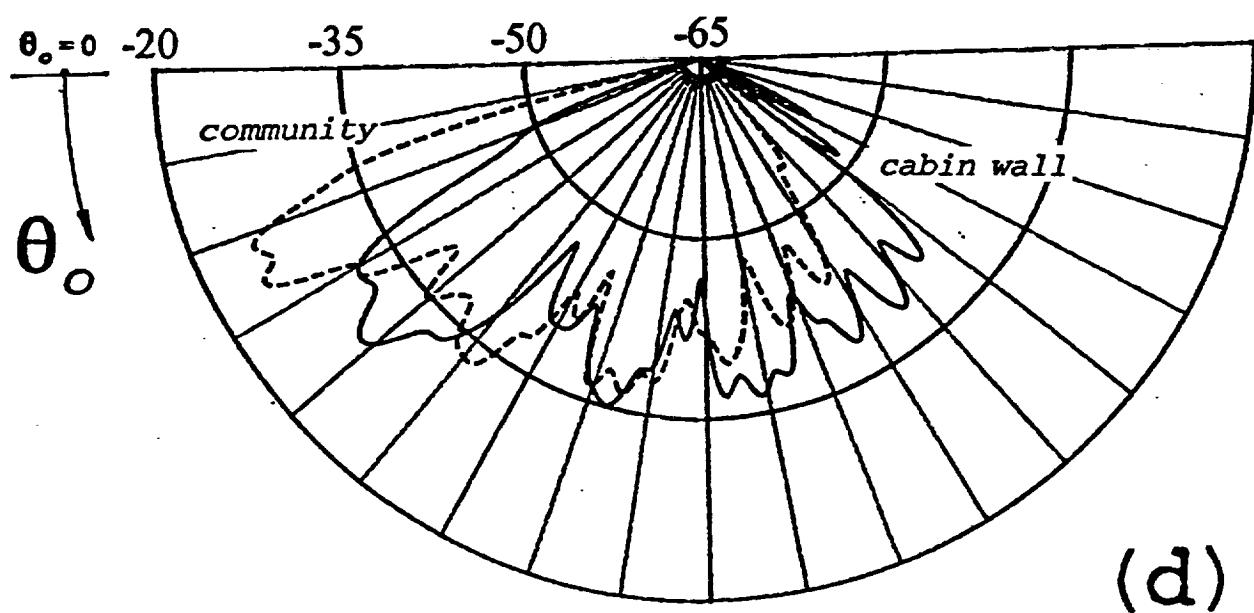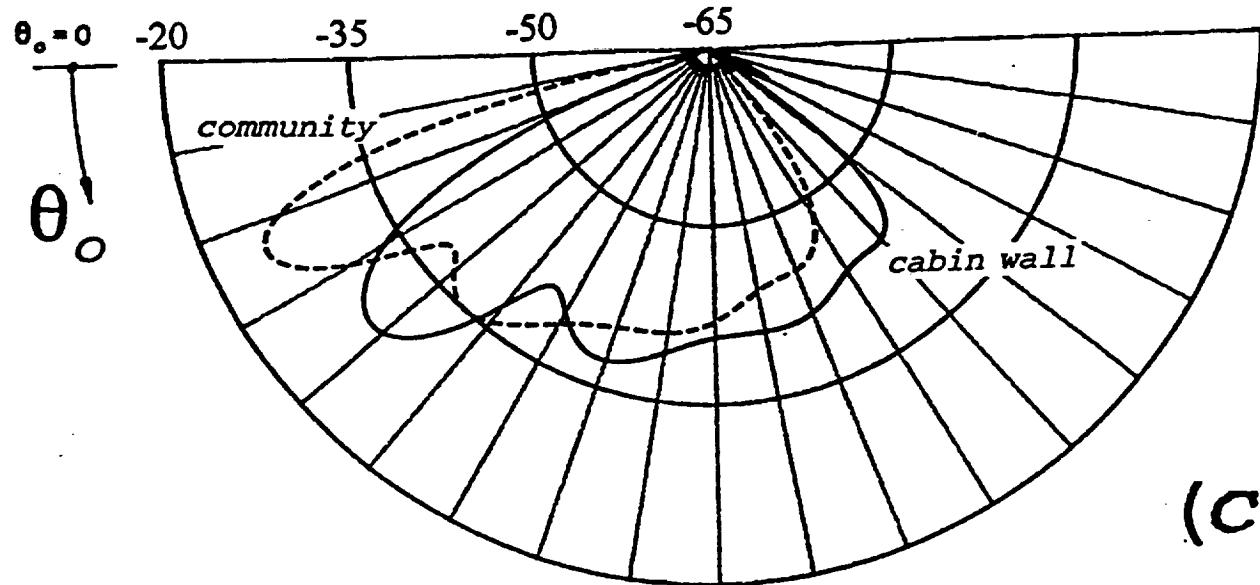
Fig. 14c,d: (c) Comparison of the incident fields heard when flying with the aircraft and at ground level. (d) Similar plot for the total fields.
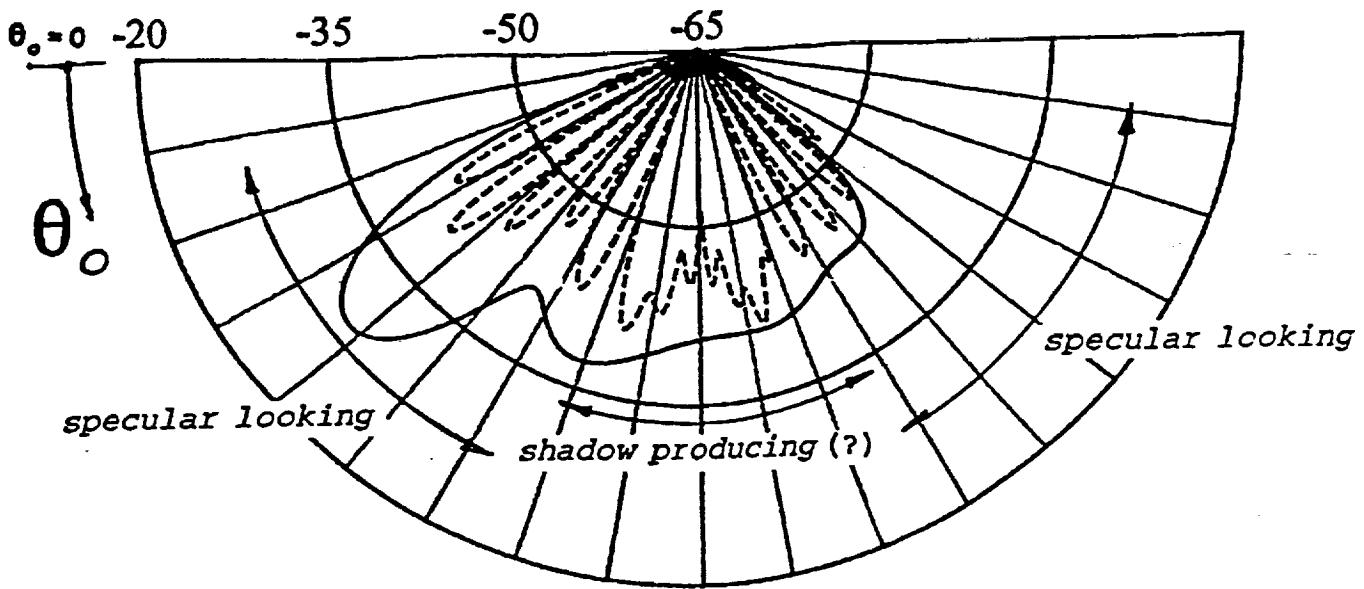
Fig. 14e: Diagnostic comparison of incident and cowl-scattered fields, with the zones of specular reflections identified as such. The cowl is unlined.
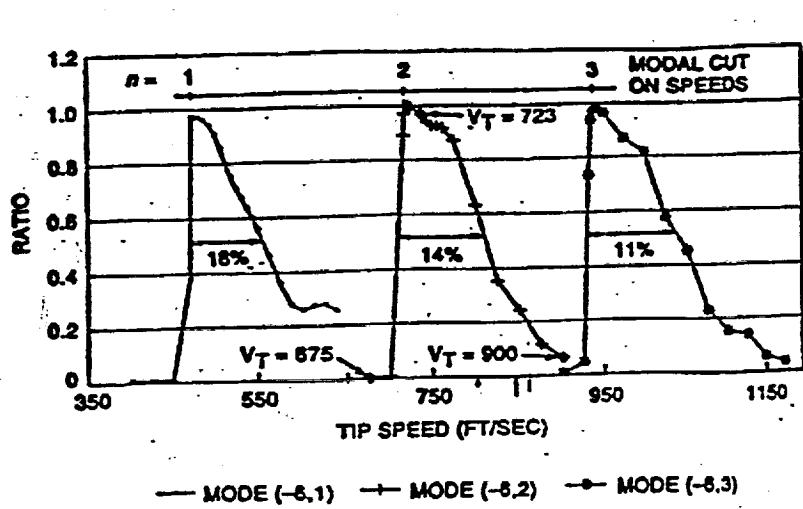

(a)
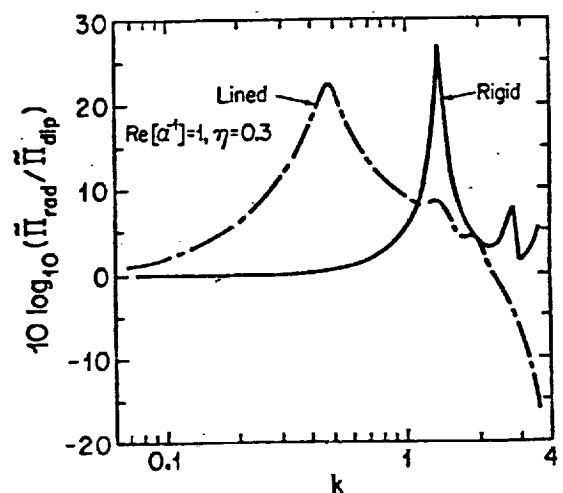
(b)

Figs. 15a,b: (a) From Meyer[7]; computed inlet reflection coefficients for three duct modes. (b) From Martinez[8]; the solid curve shows the radiated power of a single axial dipole within a rigid duct. The ordinate appears normalized by the source's freefield radiated power. The medium is still.

U_x

θ_o

$\theta_o = 0$ -10   -25   -40   -55

θ_o

total

incident

$\Delta\theta_o^{shadow}$

$\theta_o = 0$

θ_o

scattered

incident

$\Delta\theta_o^{shadow}$
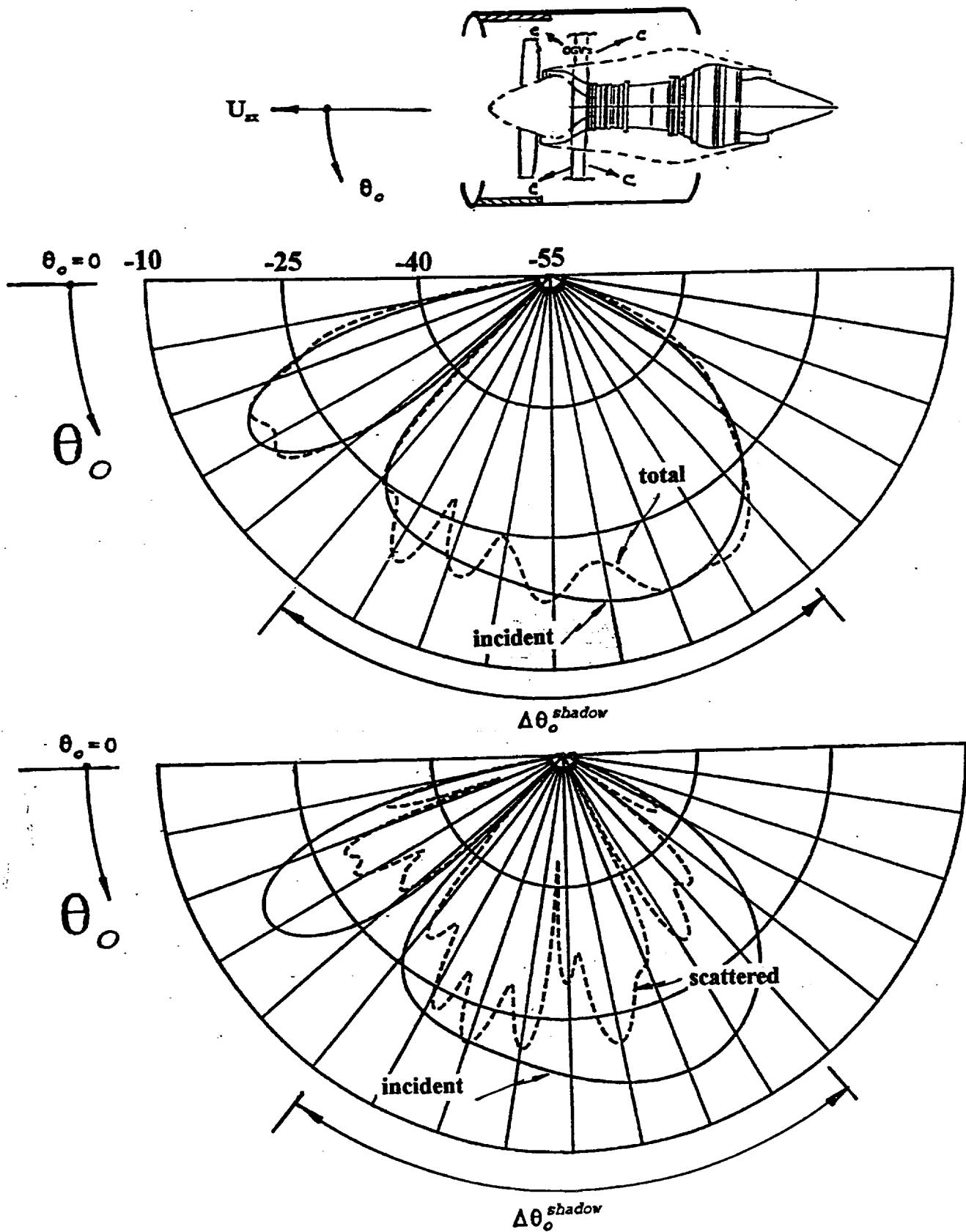
Figs. 16a,b: (a) Predictions of incident (solid) and total (dashed) fields for an inlet liner covering one third of the duct's length. The listener is on the ground. (b) Incident and cowl-scattered fields.

63
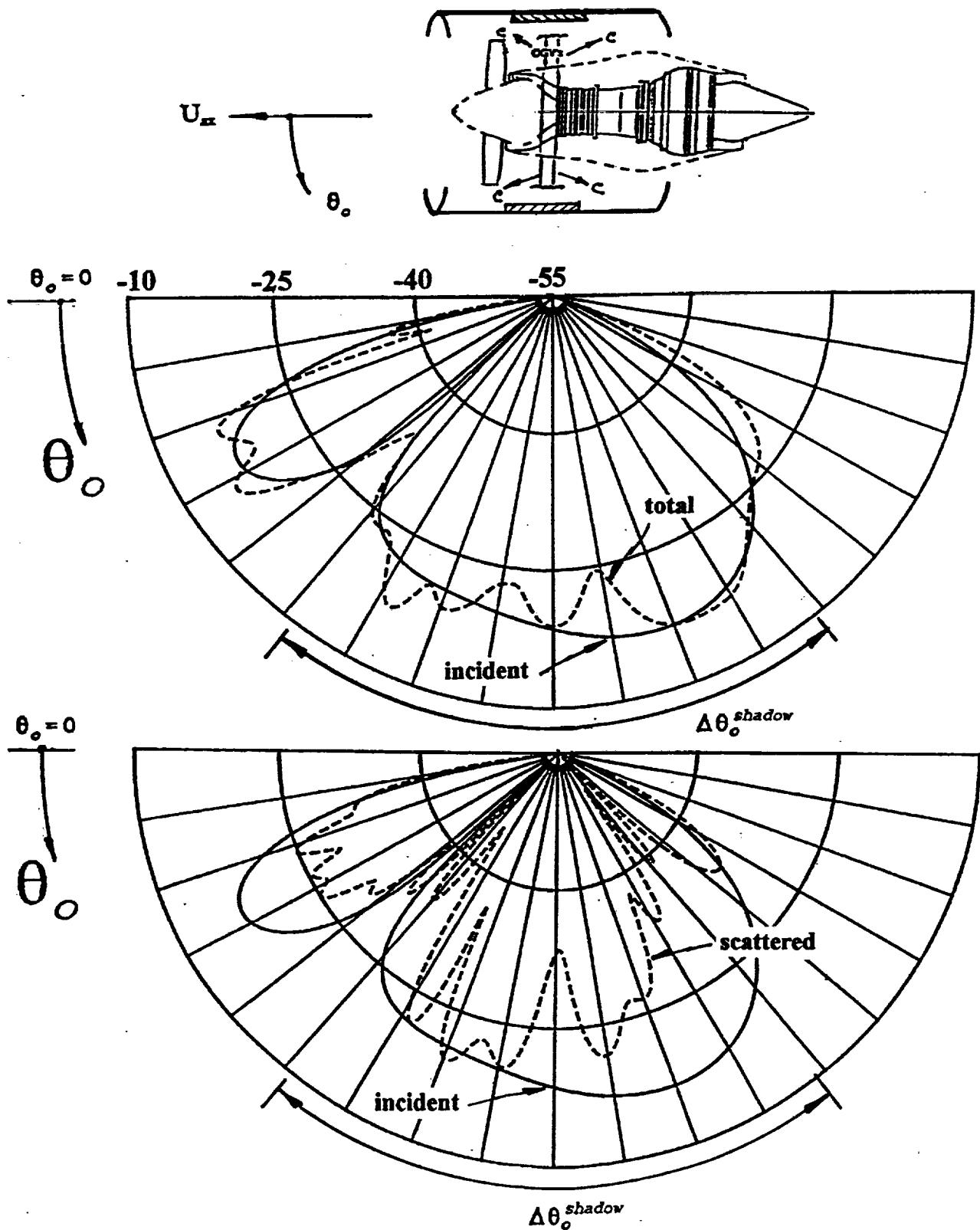
Figs. 17a,b: (a) Predictions of incident (solid) and total (dashed) fields for a central liner covering one third of the duct's length. The listener is on the ground. (b) Incident and cowl-scattered fields.
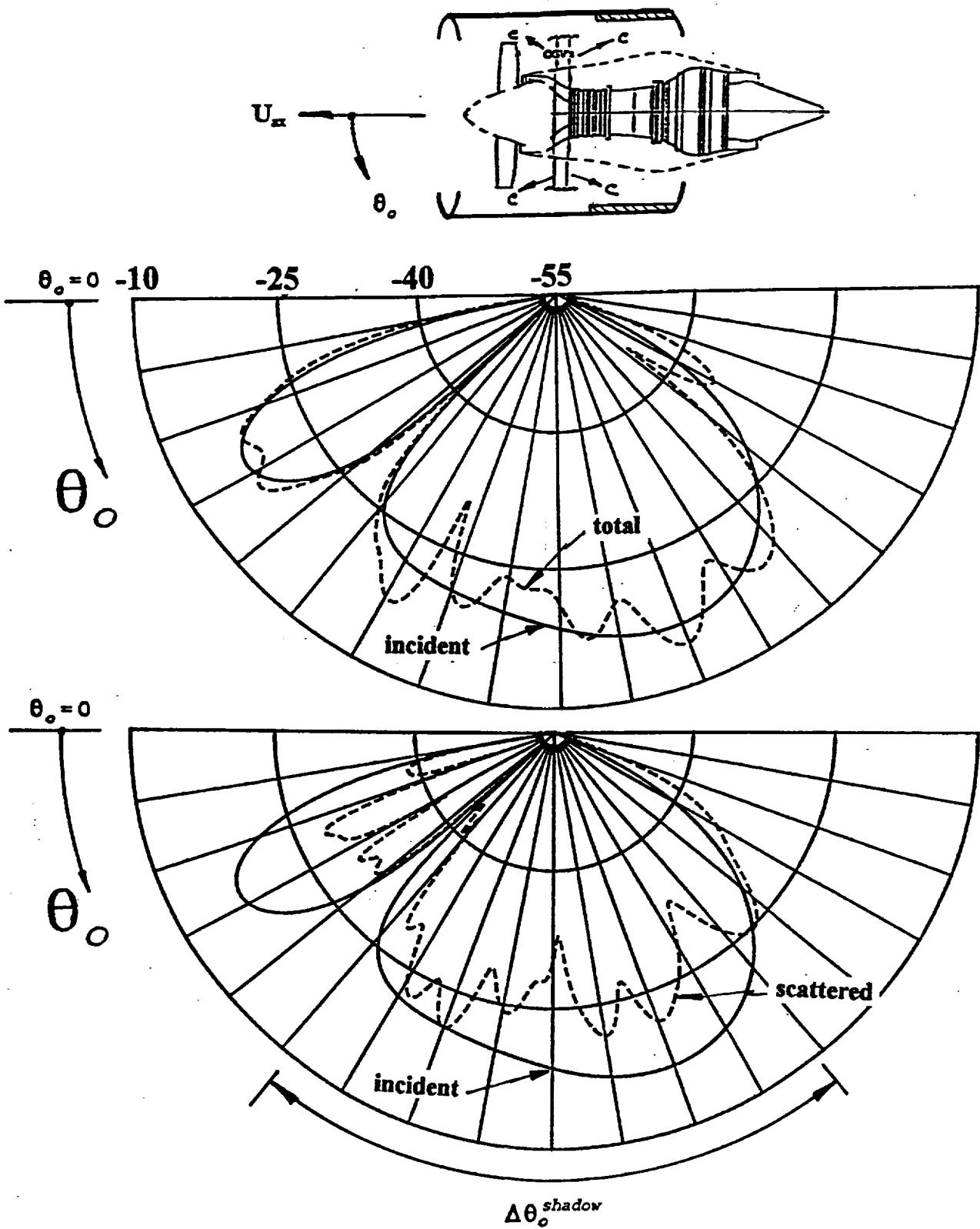
Figs. 18a,b: (a) Predictions of incident (solid) and total (dashed) fields for an outlet liner covering one third of the cowl's length. The listener is on the ground. (b) Incident and cowl-scattered fields.
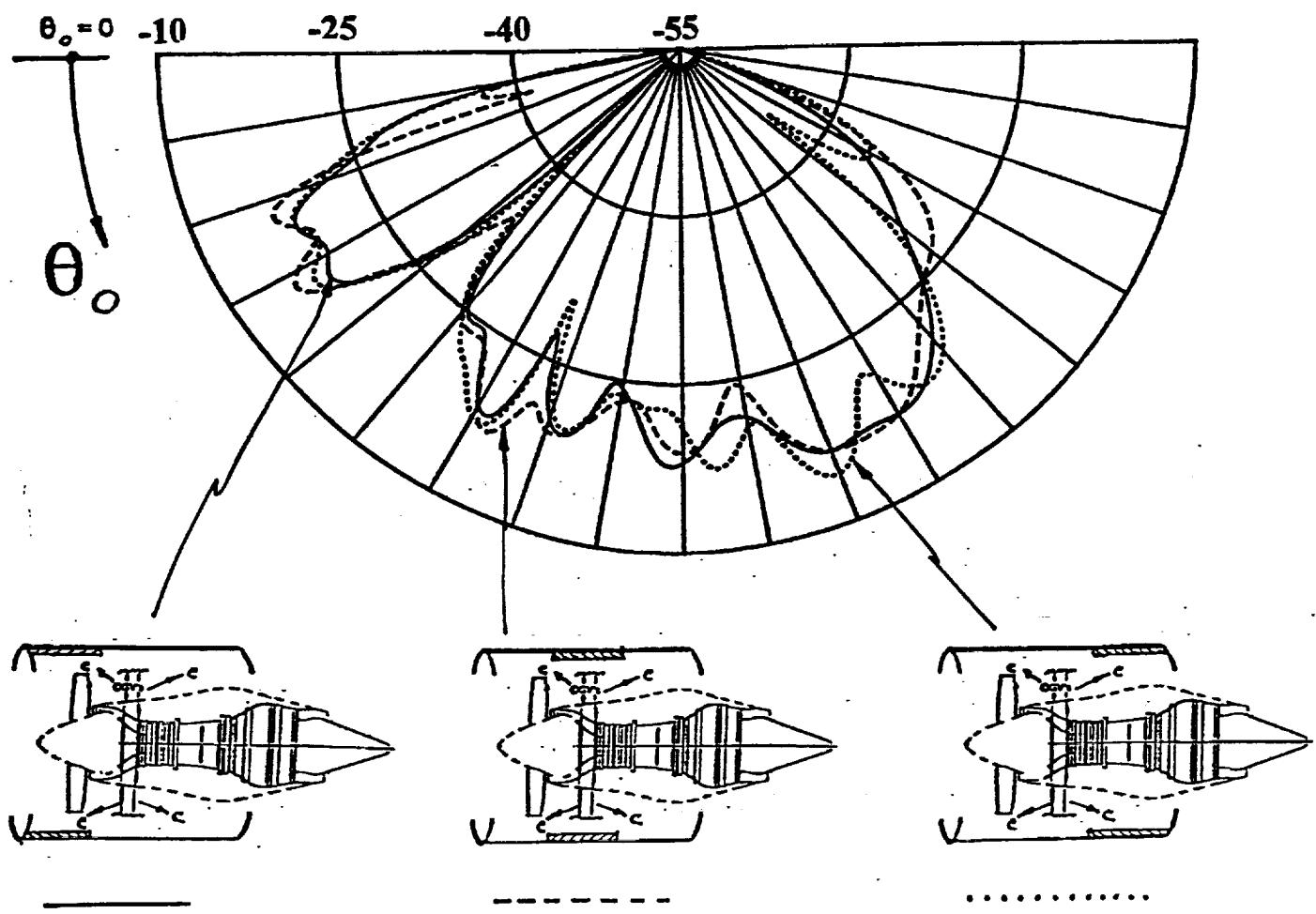
Fig. 19: Comparison of the predicted total fields of the three liner configurations in Figs. 16-18.

APPENDIX A: <u>Coupled Lifting and Nonlifting Surface Theories for the Straight Cowl in its</u>

<u>Role of Aeroacoustic Diffractor and Dissipator of Propulsor Noise</u>

<u>(adapted in part from Ref. 1)</u>

The two fundamental unknowns in the cowl's diffraction problem are the $\Delta \tilde{p}_v(z)$ diffraction load, which will be nonzero whether or not the duct is lined, and $\Delta \tilde{w}_v(z)$, which is nonzero only over the lined segments along the interior side of the cowl's two-sided wall. The first of the two coupled integral equations applies to the $r=a^+$ outer surface. That side is taken here to be rigid, and the boundary condition is therefore one of flow tangency for the incident and the cowl's self-induced field of normal velocities. The negative of the former appears on the left of the first of the two coupled equations. The cancelling field of induced flows generates the right side:

$$I: \quad -\frac{\tilde{w}_v^{inc}(z)}{U_\infty} = \frac{1}{2}\frac{\Delta \tilde{w}_v(z)}{U_\infty} + \int\limits_{-1}^{1} d\bar{z}\, K_v^{U}(z-\bar{z})\,\frac{\Delta \tilde{p}_v(\bar{z})}{\rho\, U_\infty^2}$$

$$+ \int\limits_{-1}^{1} d\bar{z}\, K_v^{L,h}(z-\bar{z})\,\frac{\Delta \tilde{w}_v(\bar{z})}{U_\infty} \quad . \tag{A.1}$$

The second equation comes from the boundary condition along $r=a^-$ surface, part or all of which may be covered with a dissipative liner:

$$II: -M_{\alpha x} \alpha_{liner}(\omega;z) \frac{\tilde{p}_v^{inc}(z)}{\rho U_{\alpha x}^2} =$$

$$\frac{\Delta \tilde{w}_v(z)}{U_{\alpha x}} - \frac{M_{\alpha x}}{2} \alpha_{liner}(\omega;z) \frac{\Delta \tilde{p}_v(z)}{\rho U_{\alpha x}^2}$$

(A.2)

$$- M_{\alpha x} \alpha_{liner}(\omega;z) \int_{-1}^{1} d\bar{z}\, K_v^{l,th}(z-\bar{z}) \frac{\Delta \tilde{p}_v(\bar{z})}{\rho U_{\alpha x}^2}$$

$$+ M_{\alpha x} \alpha_{liner}(\omega;z) \oint_{-1}^{1} d\bar{z}\, K_v^{th,th}(z-\bar{z}) \frac{\Delta \tilde{w}_v(\bar{z})}{U_{\alpha x}} \quad ,$$

where α is the liner's axially variable admittance normalized by the fluid's characteristic admittance $1/\rho c$:

$$\alpha_{liner}(\omega;z) = \frac{\rho c}{Z_{liner}(\omega;z)} \quad .$$

(A.3)

Eq. A.2 collapses to the statement $\Delta \tilde{w}_v(z) = 0$ if there are no lined segments at all along the cowl's interior. Eq. A.1 then turns into a more familiar looking lifting problem, uncomplicated by the one-sided dynamic thickness effects of the compliant dissipative liner:

$$- \frac{\tilde{w}_v^{inc}(z)}{U_{\alpha x}} = \oint_{-1}^{1} d\bar{z}\, K_v^{l,l}(z-\bar{z}) \frac{\Delta \tilde{p}_v(\bar{z})}{\rho U_{\alpha x}^2} \quad .$$

(A.4)

Kernels $K_v^{l,l}$, $K_v^{l,th}$, and $K_v^{th,th}$ in Eqs. A.1,2 are

$$K_v^{u}(z-\bar{z}) = \frac{\beta_{\infty}}{2\pi} \frac{e^{-i\frac{kM_{\infty}^2}{\beta_{\infty}^2}(z-\bar{z})}}{z-\bar{z}} + \frac{e^{-i\frac{kM_{\infty}^2}{\beta_{\infty}^2}(z-\bar{z})}}{4}$$

$$\int_C d\bar{k}\, e^{-i\bar{k}(z-\bar{z})} \left[\frac{\gamma^2 a\, H_v'(\gamma a) J_v'(\gamma a)}{\bar{k} + \frac{k}{\beta_{\infty}^2}} - \frac{i\beta_{\infty}}{\pi} \frac{|\bar{k}|}{\bar{k}} \right] \quad , \qquad (A.5)$$

$$K_v^{u,th}(z-\bar{z}) = - \frac{e^{-i\frac{kM_{\infty}^2}{\beta_{\infty}^2}(z-\bar{z})}}{4} \int_C d\bar{k}\, e^{-\bar{k}(z-\bar{z})} \left[i\gamma a\, H_v'(\gamma a) J_v(\gamma a) + \frac{1}{\pi} \right] \quad , \qquad (A.6)$$

$$K_v^{th,th}(z-\bar{z}) = - \frac{1}{2\pi\beta_{\infty}} \frac{e^{-i\frac{kM_{\infty}^2}{\beta_{\infty}^2}(z-\bar{z})}}{z-\bar{z}} + \frac{e^{-i\frac{kM_{\infty}^2}{\beta_{\infty}^2}(z-\bar{z})}}{4}$$

$$\int_C d\bar{k}\, e^{-i\bar{k}(z-\bar{z})} \left[H_v(\gamma a) J_v(\gamma a) \left(\bar{k}a + \frac{ka}{\beta_{\infty}^2} \right) + \frac{i}{\pi\beta_{\infty}} \frac{|\bar{k}|}{\bar{k}} \right] \quad . $$

$$(A.7)$$

Complex contour C is as drawn on Fig. A.1. Symbol k stands for $\omega L/2U_{\infty}$, the reduced frequency of the cowl based on the cowl's halfchord L/2, and γ is the radial wavenumber earlier defined with an "m" subscript which has been omitted here for the sake of simplicity:

$$\gamma = \sqrt{\left(\frac{kM_{ax}}{\beta_{ax}}\right)^2 - \beta_{ax}^2 \bar{k}^2} \quad .$$ (A.8)

The liner material is locally reacting and its impedance is that of a blocked acoustic layer of thickness h_{liner} and complex compressional wave speed c_{liner} (the blocking is provided by the cowl's "outer" wall, which is of infinite impedance, cf. Fig. A.2). The dissipation mechanism will be a material loss factor η associated with that compressional wave speed. Normalized by the medium's characteristic impedance ρc, Z_{liner} is

$$\frac{Z_{liner}(\omega;z)}{\rho c} = i \cot\left(\frac{\omega\, h_{liner}}{c_{liner}}\right) \quad ; \quad \left| z - z_{MID}\right| < \frac{L_{liner}}{2}$$

$$= i \cot\left(\frac{15}{B_R\sqrt{1-i\eta}} \cdot \frac{\omega}{RPM_{choice}Re\,(1/\sqrt{1-i\eta})}\right) \quad .$$ (A.9)

The second equality has fixed the real part of the liner's compressional wave speed to make impedance Z_{liner} pass through its first null, i.e., through its first thickness resonance, at a value of frequency ω corresponding to a propeller RPM of choice, RPM_{choice}.
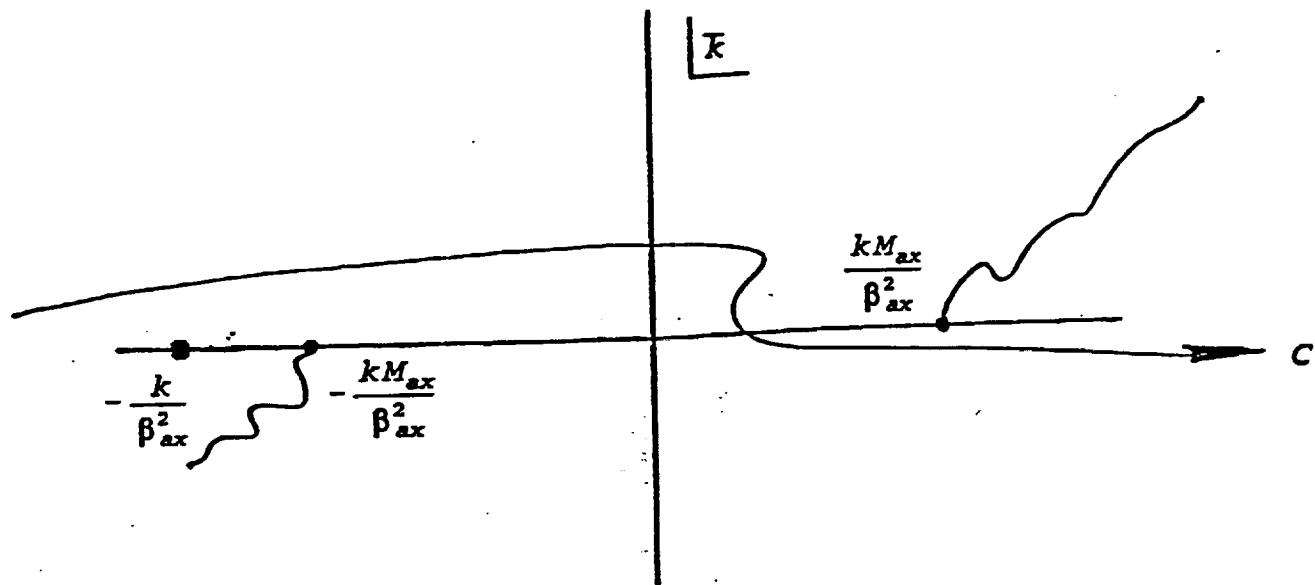
Fig. A.1 Position of the complex contour C relative to the three basic singularities of inviscid aeroacoustics. The branch points generate convected sound signals and the pole produces a shed/trailed wake vortex system springing from the cowl's outlet z=+1. The implied temporal factor is exp(-iωt). The picture is the complex conjugate of that in AIAA J. 18(6), p. 639, Fig. 2.
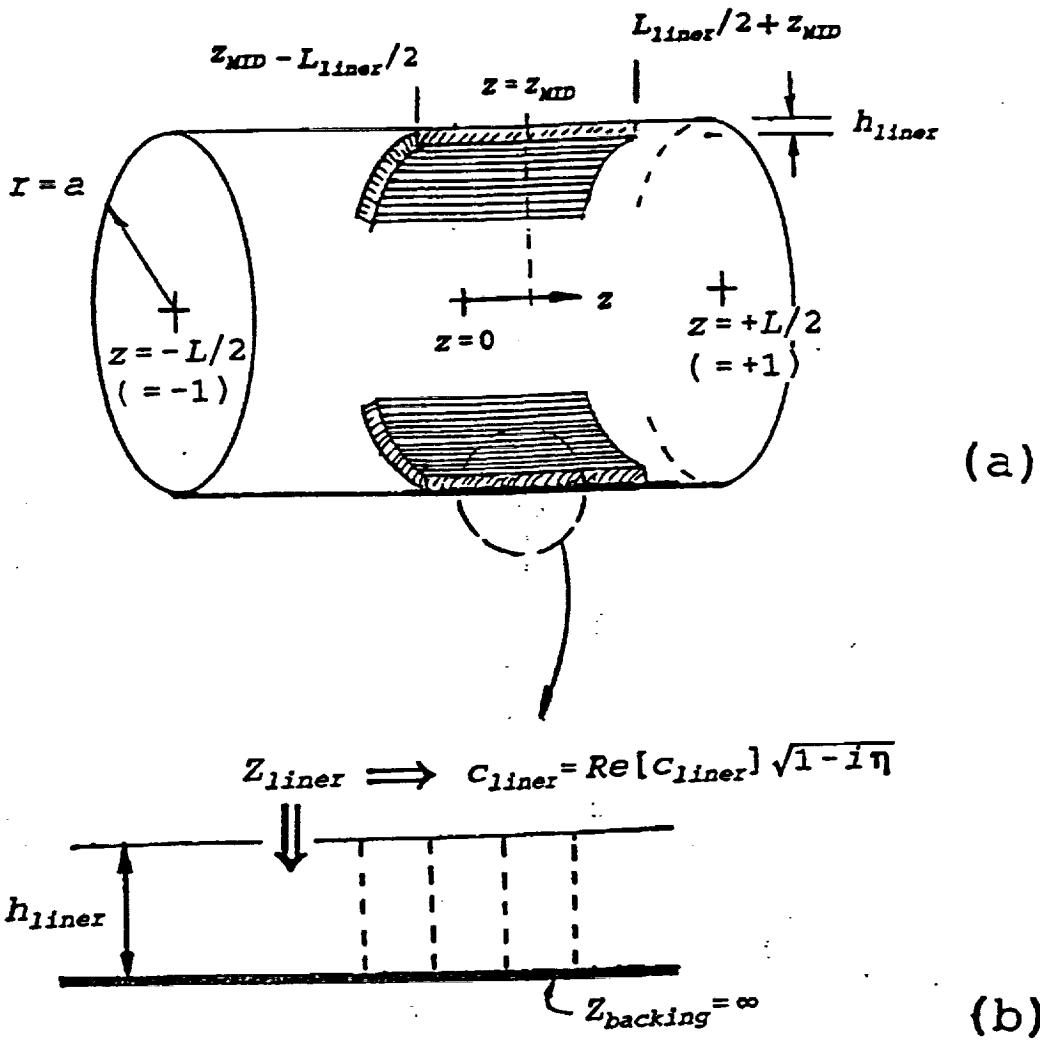
Figs. A.2a,b (a) Geometric parameters for the modeled liner, which is circumferentially uniform but with properties that may vary arbitrarily with the duct's axial variable z. A typical liner segment extends from $z = z_{mid} - L_{liner}/2$ to $z = z_{mid} + L_{liner}/2$.

(b) Blow-up of the cropping circle in (a). The liner is a locally reacting acoustic layer of "depth" h_{liner}. Its loss factor is η and its "reactive" compressional speed is given by the real part of c_{liner}. Eqs. A.1,2 take the surface of the lined segment to be flush with the unlined parts of the cowl's interior, rather than as suggested by the upper sketch.

APPENDIX B: <u>Lifting- and Nonlifting-Surface Theories for a Cowl of Arbitrary Camber and Taper</u>

B.1 <u>General</u>

The next two sections document the generalization of Ref. 1's lift and dynamic thickness analysis for a straight duct, or cowl, to now account for fore/aft camber. The cowl's cross section remains circular at every axial station. Section B.2 addresses the steady incompressible limit of the theory that would be relevant for applications at low takeoff speeds when the cowl is at an angle of attack. The results of that limiting subtheory for a ring wing in steady incompressible flow could be used to generate the duct's field of nonuniform velocities over the stage. Section B.3 extends the new subtheory to cover a more immediate goal: the diffraction kernels for the unsteady subsonic problem of interest here. All spatial variables and wavenumbers will be dimensional, unlike the main text.

B.2 <u>The Incompressible, Steady Form of the Lifting Kernel, for a Cowl of General Fore/Aft Camber and Taper</u>

The incompressible form for general camber of Ref. 1's Eq. 3 is

$$\nabla_{3\text{-}D}^2 \tilde{p}_e^{\ell}(r,\phi,z;a(\bar{s}),\bar{\phi},z(\bar{s})) = \nabla_{2\text{-}D}^2 \tilde{p}_e^{\ell} + \frac{\partial^2 \tilde{p}_e^{\ell}}{\partial z^2} =$$

$$(B.1)$$

$$- [\Delta\tilde{p}(a(\bar{s}),\bar{\phi},z(\bar{s})).d\bar{S}] \ \frac{\partial}{\partial n(\bar{s})} \ \frac{\delta[r-a(\bar{s})]}{a(\bar{s})} \ \delta[z-z(\bar{s})]\delta(\phi-\bar{\phi}) \quad ,$$

where the indicated directional derivative on the right side generalizes the radial derivative on the right side of Ref. 1's Eq. 3. The tilde on p will continue to stand for the frequency-domain version of the original time-domain Δp. The "e" subscript will similarly follow Ref.1 in denoting in the influence of the single lifting element at s=ŝ. The "ℓ" superscript stands again for the lifting component of the complete lifting/nonlifting theory. The (-) sign on the right side of Eq. 1 is the

same (-) sign on the third term on the right side of Eq. 3 of Ref. 1; i.e., $\tilde{p}_e$ in Eq. 1 is $\Delta \bar{p} d\bar{S}$ times "$-\partial G/\partial n(\bar{s})$", as explained after Eq. 2 of Ref. 1. Here $d\bar{S}$ stands for $a(\bar{s})d\phi d\bar{s}$, the element of cowl midsurface area at the source position $\bar{s}$.

With $\Theta(\bar{s})$ now as the angle which the local normal at $\bar{s}$ makes with the horizontal (Fig. B.1), the generalized directional derivative at the source position becomes

$$\frac{\partial}{\partial n(\bar{s})} \; = \; \bar{n}(\bar{s}).\nabla \; = \; \sin\Theta(\bar{s}) \; \frac{\partial}{\partial a(\bar{s})} \; + \; \cos\Theta(\bar{s}) \; \frac{\partial}{\partial z(\bar{s})} \qquad ; \tag{B.2a,b}$$

$$\bar{n}(\bar{s}) \; = \; \sin\Theta(\bar{s})\bar{e}_r \; + \; \cos\Theta(\bar{s})\bar{e}_z \quad . $$

One defines the transform pair

$$P(r,\phi;\bar{k}) \; = \; \int_{-\infty}^{\infty} \frac{dz}{2\pi} \; e^{\bar{i}kz} \, \bar{p}_e^t(r,\phi,z) \; ; \; \bar{p}_e^t(r,\phi,z) \; = \; \int_{-\infty}^{\infty} d\bar{k}e^{-\bar{i}kz} P(r,\phi;\bar{k}) \qquad , \tag{B.3a,b}$$

as on Eqs. 6a,b of Ref. 1, and applies Eq. B.3a to Eq. B.1. Then

$$P \; = \; - \; [\Delta\bar{p}.d\bar{S}] \; \frac{e^{\bar{i}k[z-z(\bar{s})]}}{2\pi} \; \frac{\partial}{\partial n(\bar{s})} \cdot \left(-\frac{i}{4}\right) H_o^{(1)}(i|\bar{k}|\sqrt{\quad}) \tag{B.4}$$

$$= \; \frac{[\Delta\bar{p}.d\bar{S}]}{4\pi^2} \; e^{\bar{i}k[z-z(\bar{s})]} \cdot \frac{\partial}{\partial n(\bar{s})} K_o\left(|\bar{k}| \sqrt{r^2+a^2(\bar{s})-2ra(\bar{s})\cos(\phi-\bar{\phi})}\right) \quad ,$$

where $H_o^{(1)}$ is the zeroth-order Hankel function of the first kind and K_o is its modified form. Expressing Eq. B.4 in terms of circumferential modes ν gives, via Eq. B.3b,

$$\vec{p}_e^t(r=a(s),z,\phi) = \frac{[\Delta\vec{p}.d\vec{S}]}{4\pi^2} \sum_{v=-\infty}^{\infty} e^{-iv(\phi-\bar{\phi})}$$

(B.5)

$$\cdot \int_C d\bar{k} \, e^{-i\bar{k}[z-z(\bar{z})]} \frac{\partial}{\partial n(\bar{s})} \begin{Bmatrix} K_v[|\bar{k}|a(s)]I_v[|\bar{k}|a(\bar{s})] \ , & a(s)>a(\bar{s}) \\ K_v[|\bar{k}|a(\bar{s})]I_v[|\bar{k}|a(s)] \ , & a(s)<a(\bar{s}) \end{Bmatrix} \quad .$$

Contour C is as portrayed in Fig. A.1 with $\beta_{\alpha c}=1$, and upon removal of L/2 used in that figure as a normalizing coating [ignore for the moment also the resulting pole at $\bar{k}=-\omega/U_{\alpha c}$.

The next step toward the new twice nonplanar lifting-surface theory for the diffracting cowl is to relate the pressure $\vec{p}_e^t$ at a field point on the duct's surface to the normal-to-duct fluid velocity at that same point. This process requires the intermediate calculation of a set of pressure gradients taken along a line, semi-infinite in z, whose landing point is the axial coordinate z(s) of that receiver point. Eq. B.5 has anticipated this requirement and has fixed the field's radial variable "a(s)" to correspond to the radial value for the control point, while allowing variable z to roam a semi-infinite range $-\infty<z<z(s)$.

The direction of the required gradient of $\vec{p}_e^t(a(s),\phi,z=free)$, corresponds to the landing point's surface normal $\vec{n}(s)$ [Fig. B.1, bottom left]. This directional derivative is

$$\frac{\partial\vec{p}_e^t(a(s),\phi,z)}{\partial n(s)} = \vec{n}(s).\nabla\vec{p}_e^t = \frac{[\Delta\vec{p}.d\vec{S}]}{4\pi^2} \sum_{v=-\infty}^{\infty} e^{-iv(\phi-\bar{\phi})}$$

$$\cdot \int_C d\bar{k} \, e^{-i\bar{k}[z-z(\bar{s})]} \left\{\sin\Theta(s)\frac{\partial}{\partial a(s)} - i\bar{k}\cos\Theta(s)\right\} \left\{\sin\Theta(\bar{s})\frac{\partial}{\partial a(\bar{s})} + i\bar{k}\cos\Theta(\bar{s})\right\} \quad (B.6)$$

$$\begin{Bmatrix} K_v[|\bar{k}|a(s)]I_v[|\bar{k}|a(\bar{s})] \ , & a(s)>a(\bar{s}) \\ K_v[|\bar{k}|a(\bar{s})]I_v[|\bar{k}|a(s)] \ , & a(s)<a(\bar{s}) \end{Bmatrix} \quad .$$

The second half of the just-cited twofold calculation is the conversion of this pressure gradient into a normal velocity w(s). This final operation uses the linearized inviscid momentum equation for this velocity component $w(a(s),\phi,z)$ of the perturbed flow along direction $\vec{n}(s)$,

$$-\rho\left(-i\omega + U_{\infty}\frac{\partial}{\partial z}\right)\tilde{w}_e^l(a(s),\phi,z) = \frac{\partial\tilde{p}_e^l(a(s),\phi,z)}{\partial n(s)} \quad . \tag{B.7}$$

Eqs. B.6, 7 and 8b now lead to

$$\tilde{w}_e^l(a(s),\phi,z(s)) = -\frac{e^{i\omega z(s)/U_{\infty}}}{\rho U_{\infty}} \cdot \frac{[\Delta\tilde{p}.d\bar{S}]}{4\pi^2} \sum_{\nu=-\infty}^{\infty} e^{-i\nu(\phi-\bar{\phi})}$$

$$\cdot \int_C d\bar{k}\, e^{\bar{k}z(i)}\left\{\cdot\cdot\right\}\left\{\cdot\cdot\right\}\left\{\cdot\cdot\right\}\int_{-\infty}^{z(s)} dz\, e^{-i[\bar{k}+\omega/U_{\infty}]z} \quad , \tag{B.8}$$

where the three factors within curly brackets in the wavenumber transform on the right side stand for the three similarly bracketed terms in the k integrand of Eq. B.6.

The "−∞" bottom limit of the z and final integral in Eq. B.9a causes that integral to exist only for

$$Im[\bar{k}] > Im\left[-\frac{\omega}{U_{\infty}}\right] \quad . \tag{B.9}$$

One finally obtains that

$$\tilde{w}_e^l(a(s), \phi, z(s)) = \frac{-i\,[\Delta\bar{p}\cdot d\bar{S}]}{4\pi^2\rho\,U_{ac}} \cdot \sum_{\nu=-\infty}^{\infty} e^{-i\nu(\phi-\bar{\phi})}$$

(B.10)

$$\cdot \int_C \frac{d\bar{k}\,e^{-\bar{k}\,[z(s)-z(\bar{s})]}}{\bar{k} + \omega/U_{ac}} \{\cdots\}\{\cdots\}\{\cdots\} \cdot$$

Eq. B.10 states the transfer function linking the flow velocity along direction $\bar{t}(s)$ at receiver point $a(s),\phi,z(s)$ to the elemental force that induces it at source position $a(\bar{s}),\phi,z(\bar{s})$. The passage of contour C over the real-axis pole at $\bar{k} = -\omega/U_{ac}$ incorporates Eq. B.9b. This existence condition holds regardless of the sign which real life could impose on the imaginary part of ω; e.g., in an aeroelastic context the sign of $Im(\omega)$ might have to be allowed to "float". Eq. B.9b would put contour C above $-\omega/U_{ac}$ in any case and thereby would generate the shed wake expected of the lifting element (Ref. 1, p. 15).

The last steps in the new development here are: (1) Integrate the right side of Eq. B.10 with respect to its source arclength variable $\bar{s}$ and circumferential running angle ϕ over the spatial domain $-S/2 < \bar{s} < S/2$, $0 < \phi < 2\pi$ that corresponds to the cowl's twice-warped lifting surface; (2) Identify the circumferential modes of the unknown diffraction loading distribution by means of

$$\int_0^{2\pi} d\bar{\phi}\, e^{i\nu\bar{\phi}} \Delta\bar{p}(\bar{s},\bar{\phi}) = 2\pi\,\Delta\bar{p}_\nu(\bar{s}) \quad ; \quad \Delta\bar{p}(\bar{s},\bar{\phi}) = \sum_{\nu=-\infty}^{\infty} e^{-i\nu\bar{\phi}} \Delta\bar{p}_\nu(\bar{s})$$

(B.11a,b)

and finally, (3) Enforce flow tangency over the lifting surface by requiring at every s point that the total normal self-induced flow cancel the normal component of the incident field.

The final lifting-surface equation resulting from those three steps is

$$-\tilde{w}_\nu^{inc}(s) = \int_{-S/2}^{S/2} d\bar{s}\, K_\nu^{l,t}(s,\bar{s})\, \Delta\bar{p}_\nu(\bar{s}) \quad ,$$

(B.12a)

with kernel $K_v^u(s,\bar{s})$ given by

$$K_v^u(s,\bar{s}) = \frac{\sin\Theta(s)}{2\pi\rho U_{\infty}} \cdot \frac{1}{s-\bar{s}} + \frac{a(\bar{s})}{2\pi\rho U_{\infty}} \int_C d\bar{k}\, e^{-i\bar{k}[z(s)-z(\bar{s})]}$$

$$\cdot \left\{ \frac{1}{\bar{k}+\omega/U_{\infty}} \left[-i\bar{k}^2 \sin\Theta(s)\sin\Theta(\bar{s}) K_v'[|\bar{k}|a(s)] I_v'[|\bar{k}|a(\bar{s})] \right. \right.$$

$$+ \bar{k}|\bar{k}| \sin\Theta(s)\cos\Theta(\bar{s}) K_v'[|\bar{k}|a(s)] I_v[|\bar{k}|a(\bar{s})] \qquad \text{(B.12b)}$$

$$- \bar{k}|\bar{k}| \cos\Theta(s)\sin\Theta(\bar{s}) K_v[|\bar{k}|a(s)] I_v'[|\bar{k}|a(\bar{s})]$$

$$\left. - i\bar{k}^2 \cos\Theta(s)\cos\Theta(\bar{s}) K_v[|\bar{k}|a(s)] I_v[|\bar{k}|a(\bar{s})] \right]_{a(s)>a(\bar{s})}$$

$$\left. + \left[\frac{i\cos[2\Theta(s)]\bar{k}/|\bar{k}| + \sin[2\Theta(s)]}{2a(s)} \right] e^{-|\bar{k}||a(s)-a(\bar{s})|} \right\} .$$

Eqs. B.12a,b are the $\Theta(s)\neq\pi/2$ generalizations of those derived and solved numerically for a straight, uncambered cowl in Ref. 1 (Eqs. 19a,b). One notes that $K_v^u(s,\bar{s})$ is not a "displacement kernel" of argument s-$\bar{s}$, as it was in Ref. 1 with s=z and $\bar{s}$=$\bar{z}$. Instead its argument is now the more general "s,$\bar{s}$" pair.

The second through fifth lines of Eq. B.12b appear specialized to segments of the duct's surface where the running values of the duct radius a($\bar{s}$) are smaller than the radius a(s) of the control point s. For the remaining parts of the surface, these four lines would simply exchange themselves for their a(s)<a($\bar{s}$) versions, based on the a(s)<a($\bar{s}$) part of Eq. B.6.

The sixth line in Eq. B.12b, that shows up left-indented relative to the previous four, is the negative of their high-k asymptote. This sixth line applies both to a(s)<a($\bar{s}$) and to a(s)>a($\bar{s}$). This term has been subtracted and added for two reasons, the first mathematical and the second

physical: (1) to improve the convergence of the transform's integrand at the infinite ends of contour C; (2) to display the nature of the kernel's expected singular behavior as the running arclength $\bar{s}$ approaches the control point's arclength position s. The negative of this term has been inverted analytically and appears as the first term on the right side of Eq. B.12b. This high-$\bar{k}$ term collapses, as it should, to the similar spectral subtraction in Ref. 1 for the special case of a straight, untapered and uncambered cowl for $\Theta(s)=\pi/2$ for all s.

B.3   Corresponding Kernels for Unsteady Subsonic Flow

The forms of the kernels needed for the diffraction problem for a cowl with a general fore/aft generator curve follow from analyses similar to that above. The radial wavenumber γ appears again without its m subscript. Again for $a(s) > a(\bar{s})$, the generalization of Appendix A's Eq. A.5 for $\Theta(s) \neq \pi/2$ is

$$
K_v^U(s,\bar{s}) = \frac{a(\bar{s})}{4\rho U_\infty} e^{-i\frac{\omega M_\infty}{c\beta_\infty^2}[z(s)-z(\bar{s})]} \int_C d\bar{k}\, e^{-i\bar{k}[z(s)-z(\bar{s})]}
$$

$$
\cdot \left\{ \frac{1}{\bar{k}+\dfrac{\omega}{U_\infty \beta_\infty^2}} \left[\gamma^2 \sin\Theta(s)\sin\Theta(\bar{s}) H_v'[\gamma a(s)] J_v'[\gamma a(\bar{s})] \right. \right.
$$

$$
+ i\gamma\left(\bar{k}+\frac{\omega M_\infty}{c\beta_\infty^2}\right)\sin\Theta(s)\cos\Theta(\bar{s})\, H_v'[\gamma a(s)] J_v[\gamma a(\bar{s})]
$$

$$
- i\gamma\left(\bar{k}+\frac{\omega M_\infty}{c\beta_\infty^2}\right)\cos\Theta(s)\sin\Theta(\bar{s}) H_v[\gamma a(s)] J_v'[\gamma a(\bar{s})]
$$

$$
\left. \left. - \left(\bar{k}+\frac{\omega M_\infty}{c\beta_\infty^2}\right)^2 \cos\Theta(s)\cos\Theta(\bar{s}) H_v[\gamma a(s)] J_v[\gamma a(\bar{s})] \right] \right\}
$$

(B.13)

The high-$\bar{k}$ asymptote of the transform's integrand generates a Cauchy term similar to that which appears first on the right side of Eq. A.5. The coefficient of that term is now a function of $\Theta(s)$. Returning again to Ref. 1, and defining $\mathcal{H}_\nu^{l,th}(z-\bar{z})$ to be

$$\mathcal{H}_\nu^{l,th}(z-\bar{z}) = \frac{\delta(z-\bar{z})}{2} + K_\nu^{l,th}(z-\bar{z}) \quad , \tag{B.14}$$

one now finds that the generalization of $\mathcal{H}_\nu^{l,th}$ for $\Theta(s) \neq \pi/2$ is

$$\mathcal{H}_\nu^{l,th}(s,\bar{s}) = \frac{i}{4} e^{-i\frac{\omega}{c}\frac{M_{\alpha}}{\beta_{\alpha}^2}[z(s)-z(\bar{s})]} \int_C d\bar{k}\, e^{-i\bar{k}[z(s)-z(\bar{s})]}$$

$$\cdot \left\{ \gamma \sin\Theta(\bar{s}) H_\nu[\gamma a(s)] J_\nu'[\gamma a(\bar{s})] \right.$$

$$\left. + i\left(\bar{k} + \frac{\omega}{c}\frac{M_{\alpha}}{\beta_{\alpha}^2} \right) \cos\Theta(\bar{s}) H_\nu[\gamma a(s)] J_\nu[\gamma a(\bar{s})] \right\} \quad . \tag{B.15}$$

Again $a(s) > a(\bar{s})$ in Eq. B.15. Finally, the generalization of $K_\nu^{th,th}$ in Eq. A.7 to $\Theta \neq \pi/2$ is

$$K_\nu^{th,th}(s,\bar{s}) = \frac{e^{-i\frac{\omega}{c}\frac{M_{\alpha}}{\beta_{\alpha}^2}[z(s)-z(\bar{s})]}}{4} \int_C d\bar{k}\, e^{-i\bar{k}[z(s)-z(\bar{s})]} \tag{B.16}$$

$$H_\nu[\gamma a(s)] J_\nu[\gamma a(\bar{s})] \left(\bar{k} + \frac{\omega}{U_{\alpha}\beta_{\alpha}^2} \right) \quad .$$
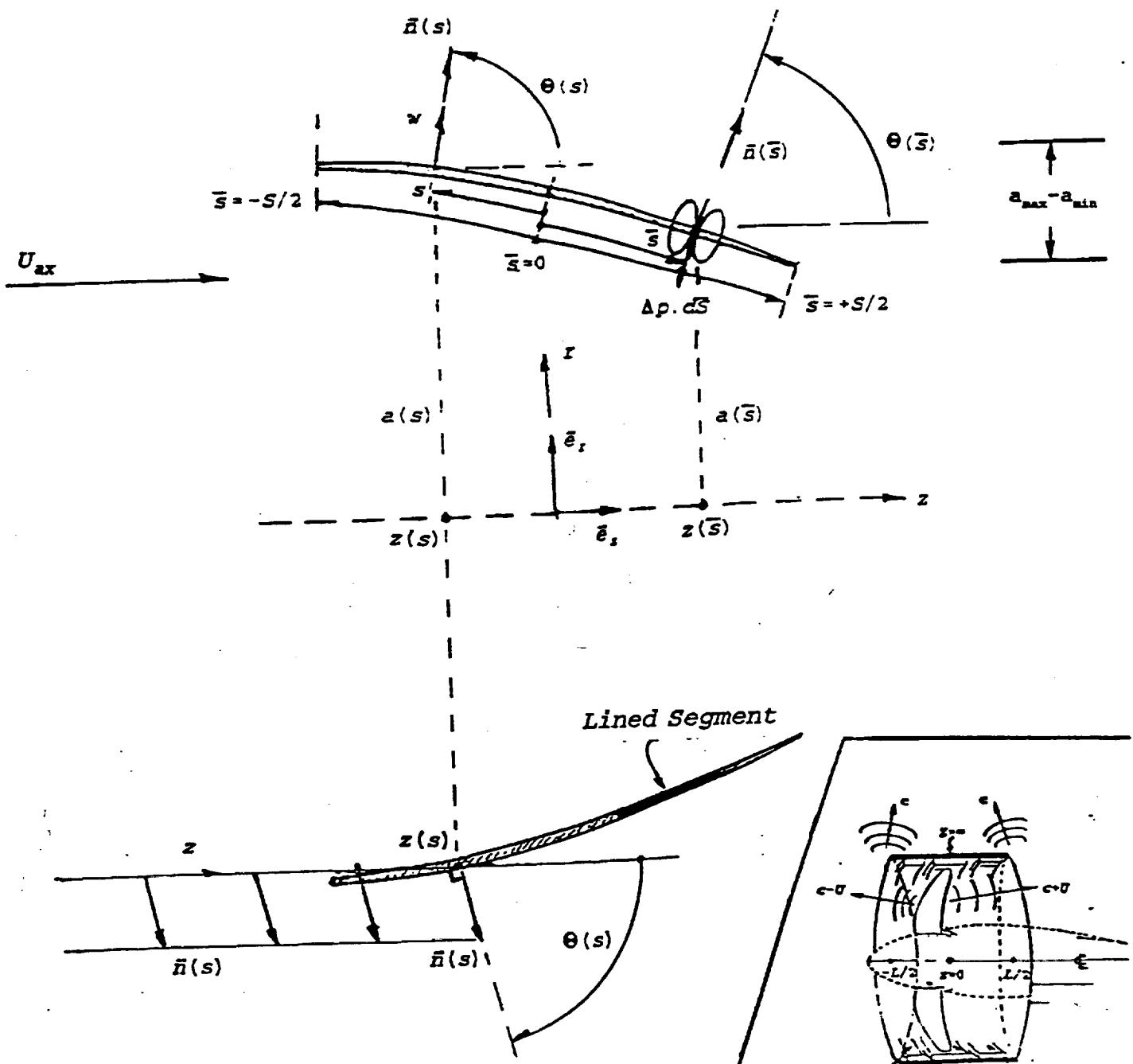
Fig. B.1 Coordinate definitions and geometric parameters for a generally cambered and tapered cowl. The source station is at arclength $\bar{s}$, which shows a typical virtual dipole. "s" marks the receiver, or control ring station, which feels an upwash "w" along the local normal. Angle $\Theta(s)$ is measured away from the downstream horizontal plane. The lower left of the main sketch shows the $-\infty < z < z(s)$ trajectory of running points "z" along which Eq. B.8 calculates the pressure gradient in the direction $\bar{n}(s)$. The insert is from Ref. 1, where the cowl had neither camber nor taper.

REPORT DOCUMENTATION PAGE

Public reporting burden for this collection of information is estimated to average 1 hour per response, including the time for reviewing instructions, searching existing data sources, gathering and maintaining the data needed, and completing and reviewing the collection of information. Send comments regarding this burden estimate or any other aspect of this collection of information, including suggestions for reducing this burden, to Washington Headquarters Services, Directorate for Information Operations and Reports, 1215 Jefferson Davis Highway, Suite 1204, Arlington, VA 22202-4302, and to the Office of Management and Budget, Paperwork Reduction Project (0704-0188), Washington, DC 20503.

1. AGENCY USE ONLY (Leave blank)	2. REPORT DATE February 1995	3. REPORT TYPE AND DATES COVERED Final Contractor Report

4. TITLE AND SUBTITLE

The Use of Cowl Camber and Taper to Reduce Rotor/Stator Interaction Noise

6. AUTHOR(S)

R. Martinez

5. FUNDING NUMBERS

WU–535–03–10
C–NAS3–27229

7. PERFORMING ORGANIZATION NAME(S) AND ADDRESS(ES)

Cambridge Acoustical Associates, Inc.
200 Boston Ave., Suite 2500
Medford, Massachusetts 02155-4243

8. PERFORMING ORGANIZATION REPORT NUMBER

E–9364

9. SPONSORING/MONITORING AGENCY NAME(S) AND ADDRESS(ES)

National Aeronautics and Space Administration
Lewis Research Center
Cleveland, Ohio 44135-3191

10. SPONSORING/MONITORING AGENCY REPORT NUMBER

NASA CR–195421

11. SUPPLEMENTARY NOTES

Work funded by NASA Small Business Innovation Research contract NAS3–27229. Project Manager, James H. Dittmar, Propulsion Systems Division, NASA Lewis Research Center, organization code 2770, (216) 433–3921.

12a. DISTRIBUTION/AVAILABILITY STATEMENT

Unclassified - Unlimited
Subject Category 71

This publication is available from the NASA Center for Aerospace Information, (301) 621–0390.

12b. DISTRIBUTION CODE

13. ABSTRACT (Maximum 200 words)

The project had two specific technical objectives: (1) To develop a realistic three-dimensional model of tonal noise due to rotor/stator interaction, as the input field for predictions of diffraction and dissipation by a lined cowl; and (2) To determine whether the generator curve of that cowl, or duct, could be "steered" to yield substantially lower values of propulsor noise along the engine's fore and aft open sectors. The more general and important aim of the research is to provide the commercial aircraft industry with a useful predictive tool to help it meet its noise-reduction goals. The work has produced a tractable and yet realistic model of rotor/stator interaction noise. The blades in the fan stage are radially divergent, twisted, and of realistically wide chords to match the high frequencies and speeds of the sound-production process. The resulting three-dimensional acoustic nearfield insonifies the interior wall of the diffracting cowl, whose shape, incidentally, does not affect fore or aft noise significantly (but other factors do).

14. SUBJECT TERMS

Rotor/stator noise; Cowl diffraction; Lined ducts

15. NUMBER OF PAGES 89

16. PRICE CODE A05

17. SECURITY CLASSIFICATION OF REPORT	18. SECURITY CLASSIFICATION OF THIS PAGE	19. SECURITY CLASSIFICATION OF ABSTRACT	20. LIMITATION OF ABSTRACT
Unclassified	Unclassified	Unclassified	

NSN 7540-01-280-5500

Standard Form 298 (Rev. 2-89)
Prescribed by ANSI Std. Z39-18
298-102

National Aeronautics and
Space Administration

Lewis Research Center
21000 Brookpark Rd.
Cleveland, OH 44135-3191

POSTMASTER: If Undeliverable — Do Not Return